OBSERVATION OF THE FUNDAMENTAL EXCITON IN LOW-TEMPERATURE GROWN GaAs USING FOUR-WAVE MIXING SPECTROSCOPY

by

Daniel Webber

Submitted in partial fulfillment of the
requirements for the degree of
Master of Science

at

Dalhousie University
Halifax, Nova Scotia
October 2013

© Copyright by Daniel Webber, 2013

Table of Contents

List of Figures . . . . **vi**

Abstract . . . . **xi**

List of Abbreviations and Symbols Used . . . . **xii**

Acknowledgements . . . . **xv**

Chapter 1 Introduction **1**

1.1 Overview 1

1.2 Influence of Disorder on the Optical Properties of LT-GaAs 4

1.3 Four Wave-Mixing Techniques (FWM) 6

1.4 Four-wave mixing signal contributions arising from many-body effects 12

1.5 FWM Studies of the Exciton in Traditional Semiconductors: Previous Work 13

1.5.1 Measurements of the Exciton FWM Response 14

1.5.2 FWM Experiments For Simultaneous Excitation of Excitons and Unbound Electron-Hole Pairs 17

1.6 Outline of the thesis 19

Chapter 2 Background Information **21**

2.1 Chapter Overview 21

2.2 Linear Optical Properties of Semiconductors 21

2.3 Optical Properties of Low-Temperature-Grown GaAs 25

2.4 Overview of Relaxation Processes Following Optical Excitation by a Pulsed Laser 27

2.5 Four-Wave Mixing for a Two-Level System without Interactions . . . 29

2.6 Influence of Excitation-Induced Dephasing on Two-Level System Dynamics 33

2.7 Four-Wave Mixing under Conditions of Simultaneous Excitation of Excitons and Continuum Transitions 35

Chapter 3 Apparatus and Experimental Techniques 39

3.1 Overview 39

3.2 Samples 41

3.3 Pulse Measurement and Optimization 43
3.3.1 Zero-Background Autocorrelation Techniques 43
3.3.2 Optimization of Pulse Duration using a Pulse Compressor . . 47

3.4 Two-Pulse Four-Wave Mixing 48

Chapter 4 Results and Discussion 55

4.1 Overview 55

4.2 Experimental Results 55
4.2.1 Spectrally-Resolved Four-Wave Mixing 56
4.2.2 Dependence of FWM results on Interpulse Delay 58
4.2.3 Comparison of Signal Characteristics for Colinear and Cross-Linear Polarization Geometries 59
4.2.4 Influence of an Optical Prepulse on the Four-Wave Mixing Response 63
4.2.5 Variation of Exciton and Continuum Response with Prepulse Excitation Conditions 67

4.3 Discussion 73
4.3.1 Observation of the Exciton in LT-GaAs 73
4.3.2 Excitation-Induced Dephasing Dominates Exciton Signal in LT-GaAs 74
4.3.3 Dephasing Dynamics in LT-GaAs 75
4.3.4 Prepulse Power Dependence 78
4.3.5 Prepulse Delay Dependence 80

Chapter 5 Conclusion 82

5.1 Overview 82

5.2 Summary: Conclusions of this Thesis Work 82

5.3 Future Work 84

Bibliography 85

Appendix A Copyright Permissions 91

List of Figures

Figure 1.1 (a) Full band structure of GaAs calculated using a pseudopotential technique 5

Figure 1.2 A schematic representation of a typical two-pulse four-wave mixing experiment is shown. Due to an interference of the two electric fields along directions $\vec{k}_1$ and $\vec{k}_2$, a third electric field along $\vec{k}_2$ is self-diffracted off of this interference, and projected along the $2\vec{k}_2 - \vec{k}_1$ direction. 7

Figure 1.3 (a) Table showing the matrix elements of the electric dipole operator between heavy-hole and conduction band states. $\hat{\mu}_{\pm} = \frac{1}{\sqrt{2}}\left(\hat{\mathrm{X}} \pm i\hat{\mathrm{Y}}\right)$ where $\hat{\mathrm{Z}}$ is the growth direction of the heterostructure. (b) Optical selection rules resulting from (a) $\sigma+$ ($\sigma-$) indicating transitions induced by right (left) circularly-polarized light. (c),(d) An illustration of the spatial distribution of the excited population across a thin slice of the sample in the $\hat{\mathrm{X}}$ direction. $n_{\sigma+}$ and $n_{\sigma-}$ correspond to the excited populations of the $\sigma+$ and $\sigma-$ exciton transitions given in (b). For co-polarized beams (c), a constructive superposition of the two density gratings occurs. However, in (d) a uniform total (spin-averaged) carrier density is created (dashed line). 10

Figure 1.4 (a): A two-level system depicting a collection of discrete resonances with the same transition energy referred to as a homogeneously-broadened transition. (b): A two-level system exhibiting inhomogeneous broadening, corresponding to a distribution of closely-spaced transition energies. (c): Four-wave mixing signal versus time for a homogeneously broadened system. (d): Four-wave mixing signal versus time for an inhomogenously broadened system. 12

Figure 1.5 Shown are the combined results of a SR-FWM experiment in bulk Ge. 18

Figure 2.1 In an absorption process, a photon with energy $\hbar\omega$ can excite an electron from the valence (V) to the conduction band (C). The energy of the photon dictates which momentum states can be involved in electronic transitions. 23

Figure 2.2 The absorption spectrum for interband transitions in GaAs from Eqn. 2.5 (dashed curve) is compared with an experimentally measured absorption spectrum (solid curve). The Coulomb interaction between the electron and hole leads to the formation of excitons and a corresponding sharp absorption peak below the band gap. In addition, the electron-hole interaction leads to Sommerfeld enhancement of the continuum absorption near the band edge, reflected in the experimental data. 24

Figure 2.3 (a) A plot of the linear absorption for as-grown LT-GaAs (solid line) and GaAs (dashed line). The smooth linear absorption profile of LT-GaAs is characteristic of the high density of defects present that cause smearing of the band edge. (b) A simple band structure diagram of LT-GaAs is shown, illustrating the possible transitions that contribute at energies near the band gap. 26

Figure 3.1 A schematic diagram of the four-wave mixing apparatus used in this thesis work. The labels refer to: BBO: Beta-barium borate crystal, BS: Beam splitter, C: cryostat, F: Neutral density filter, HWP: Half-wave plate, PC: Pulse compressor, PMT: Photomultiplier tube, S: Polarized beam splitting cube, SF: Spatial filter, TS: Linear translation stage, WS: Woofer speaker. The three beams incident on the sample are: Thick solid line: $\vec{E}_2$, Thin solid line: $\vec{E}_1$, Dashed thick line: Prepulse. The thick blue line exiting the sample corresponds to the four-wave mixing signal in the $2\vec{k}_2 - \vec{k}_1$ direction. The pulse duration is measured (and spatial overlap is optimized) by inserting mirror M to redirect the excitation beams to an equivalent focus containing a BBO crystal. 40

Figure 3.2 The sample at various stages of preparation. The as-grown sample is mounted sample-side down to the sapphire window using optical adhesive, as shown in (a). Mechanical polishing is used to remove approximately 300 μm of the GaAs substrate, as illustrated in (b). In (c), chemical etching removes the remainder of the substrate leaving only the sample and a thin stop etch layer. 42

Figure 3.3 Linear absorption spectrum of GaAs (black circles) and LT-GaAs (blue triangles) taken at 10K. 43

Figure 3.4 (a) A schematic diagram of the portion of the four-wave mixing apparatus used for measurement of the pulse autocorrelation. Parallel alignment of the two excitation beams was performed by placing an alignment tool at three different locations in the optical setup, as indicated by the numbered blue squares. (b) The tool used in the alignment procedure. 47

Figure 3.5 A schematic diagram of a pulse compressor containing prisms P_1 and P_2 in a folded geometry. The compressor is used to compensate positive GVD by introducing a uniform wavelength dependent time-delay to each component. Prism P_2 can be moved into the beam path using a micrometre-controlled translation stage, as indicated by the double-ended arrow. 49

Figure 3.6 (a) Measured pulse autocorrelation. A Gaussian fit to the autocorrelation trace yielded a FWHM of 41 fs, corresponding to a pulse duration of 29 fs; (b) The laser pulse spectrum collected just outside the laser source. For the experiments conducted in this thesis, the laser was centred at 1.553 eV, with a bandwidth of 74.0 meV. The low-energy tail of the pulse does not go to zero due to the laser source. 50

Figure 3.7 A circuit diagram of the compensation circuit used to correct for the response of the PMT. 51

Figure 3.8 A schematic illustration of a two-pulse four-wave-mixing geometry with a prepulse. The two investigatory pulses $\vec{E_1}$ and $\vec{E_2}$ are are separated by an interpulse delay τ. At a time τ_{PP} before (or after) arrival of $\vec{E_1}$ and $\vec{E_2}$, a spectrally-identical prepulse $\vec{E_{PP}}$ injects a population of free-carriers into the system. The prepulse does not affect the phase-matching condition for two-pulse FWM, and so the diffracted macroscopic polarization still lies in the $2\vec{k}_2 - \vec{k}_1$ direction. 53

Figure 4.1 Linear absorption spectrum of GaAs and LT-GaAs at 10 K. . 57

Figure 4.2 (a) The FWM spectrum at zero pulse delay for GaAs (circles) and LT-GaAs (triangles) shown together with the excitation pulse spectrum (red curve). (b) Spectrally-resolved four-wave mixing measurement on GaAs and (c) LT-GaAs. 58

Figure 4.3 SR-FWM results for GaAs for the two polarization geometries investigated in this thesis. For (a) co-polarized pulses and (b) cross-polarized pulses. (c) An energy slice at $\tau = 20$ fs reveals the strong enhancement at the exciton resonance for the co-polarized configuration in comparison to cross-polarized case. The results of the cross-polarized case have been magnified 5.08 times for clarity. 61

Figure 4.4 SR-FWM results for LT-GaAs for the two polarization geometries investigated in this thesis. For (a) co-polarized pulses and (b) cross-polarized pulses. (c) An energy slice at $\tau = -10$ fs . The results of the cross-polarized case have been magnified 3.57 times for clarity. 62

Figure 4.5 SR-FWM results for GaAs for two prepulse conditions investigated in this thesis. For a (a) prepulse delayed 600 fs and (b) at zero delay with respect to mutual zero delay. (c) An energy slice at $\tau = 20$fs is shown to highlight the change in TI-FWM signal at the excitonic resonance. 65

Figure 4.6 SR-FWM results for LT-GaAs for two prepulse conditions investigated in this thesis. For a (a) prepulse delayed 600 fs and (b) at zero delay with respect to mutual zero delay. (c) An energy slice at $\tau = -10$fs highlights the dramatic change in the TI-FWM line shape with the addition of the prepulse. 66

Figure 4.7 Results for GaAs for varying prepulse power. For a range of prepulse powers, the FWM emission as a function of pulse delay was collected at two energies probed in this thesis work. The TI-FWM contour as a function of prepulse power is depicted in (a) for the exciton, and (b) for the continuum. The peak value versus pulse delay corresponds to the data in (a) and (b) and is plotted in (c) and (d) respectively. 68

Figure 4.8 Results for LT-GaAs for varying prepulse power. For a range of prepulse powers, FWM emission as a function of pulse delay was collected at two energies probed in this thesis work. The TI-FWM contour as a function of prepulse power is depicted in (a) for the exciton, and (b) for the continuum. The peak value as a function of prepulse power for both of these contours are plotted in c) and d) respectively. 69

Figure 4.9 Results for GaAs for varying prepulse delay with respect to mutual zero delay. For a range of prepulse delays, FWM emission as a function of pulse delay was collected at the two energies probed in this thesis work. The TI-FWM contour as a function of prepulse delay is plotted in (a) for the exciton, and (b) for the continuum. The peak value as a function of prepulse delay for both of these contours are plotted in (c) and (d) respectively. The solid black line is the autocorrelation of $\vec{E}_1$ and $\vec{E}_2$, and the gray shaded area is the region of pulse overlap. The solid red and dashed blue lines represent fits to two models of the FWM response considered in this thesis work. 71

Figure 4.10 Results for LT-GaAs for varying prepulse delay with respect to mutual zero delay. For a range of prepulse delays, FWM emission as a function of pulse delay was collected at the two energies probed in this thesis work. The TI-FWM contour as a function of prepulse delay is plotted in (a) for the exciton, and (b) for the continuum. The peak value as a function of prepulse delay for both of these contours are plotted in (c) and (d) respectively. The solid black line is the autocorrelation of $\vec{E}_1$ and $\vec{E}_2$, and the gray shaded area is the region of pulse overlap. 72

Figure 4.11 (a) TI-FWM signal slice at zero delay for GaAs. (b) TI-FWM signal slice at zero delay for LT-GaAs. The red line is a fit using a Gaussian and a squared Lorentzian. 77

Abstract

The nonlinear optical response of low-temperature (LT) grown GaAs were studied using four-wave mixing techniques. Through measurements of the four-wave mixing response as a function of pulse delay and photon energy, a strong optical response was identified associated with the fundamental band gap exciton. These experiments therefore demonstrated the importance of the exciton in understanding the ultrafast nonlinear optical response of LT-GaAs despite the absence of any evidence of the exciton in past linear absorption studies in this material. Measurement of the four-wave mixing response as a function of pulse delay and the polarization states of the two excitation pulses shows that the dominant contribution to the exciton signal is tied to excitation-induced dephasing. Four-wave mixing experiments in which the sample is exposed to an additional laser pulse indicate that the exciton signal may be strongly diminished due to a combination of screening and a reduction in the total dephasing time. The short temporal duration of the above effect provides evidence of an ultrashort ($<$ 100 fs) electron trapping time in this system tied to arsenic related defects introduced during low-temperature growth. These findings are of importance to the understanding of the optical properties of LT-GaAs and will aid in the development of optoelectronic devices using this material system.

List of Abbreviations and Symbols Used

$\alpha(\omega)$	Absorption coefficient at frequency ω
Al_2O_3	Sapphire
AlGaAs	Aluminum gallium arsenide
As_{Ga}	Arsenic antisite
As^0_{Ga}	Neutral arsenic antisite state
As^+_{Ga}	Ionized arsenic antisite state
As_i	Arsenic Interstitial
BBO	Beta-Barium Borate
BS	Beamsplitter
C	Cryostat
CB	Conduction band
CC	Continuum contribution
E_g	Band gap energy
E_1	Electric field of pulse 1
E_2	Electric field of pulse 2
E_{PP}	Electric field of prepulse
EID	Excitation-induced dephasing
eV	Electron Volts (units of energy)
F	Neutral density filter
FWM	Four-wave mixing
γ_0	Intrinsic dephasing rate
γ	Dephasing rate
Γ	EID coefficient
GaAs	Gallium arsenide
GaMnAs	Gallium manganese arsenide
GaNAsSb	Gallium Nitride Arsenide Antimonide
GVD	Group velocity dispersion

$\hbar$	Planck's constant
$H(\tau)$	Heaviside step function function
HH	Heavy hole
HWP	Half-wave plate
InGaAs	Indium Gallium Arsenide
InP	Indium phosphide
$\vec{k}_1$	Pulse E_1 wavevector
$\vec{k}_2$	Pulse E_2 wavevector
LF	Local field
LH	Light hole
LT-GaAs	Low-temperature grown gallium arsenide
OBE	Optical Bloch equations
MBE	Molecular beam epitaxy
N	Excited carrier density
μ	Transition dipole moment
n	Excited state occupation
p	Coherence state occupation
P_1	Prism one
P_2	Prism two
P_x	Macroscopic exciton polarization
PC	Pulse compressor
$\Psi_{\nu,\vec{k}}(\vec{r})$	Bloch function
PMT	Photomultiplier tube
SF	Spatial filter
SO	Spin-orbit split-off
SR	Spectrally-resolved
S_{SR}	Spectrally-resolved four-wave mixing signal
S_{TR}	Time-resolved four-wave mixing signal
S_{TI}	Time-integrated four-wave mixing signal

τ	Interpulse delay
Ti:Sapphire	Titanium sapphire
TI	Time-integrated
TR	Time-resolved
TS	Translation stage
γ_1	Population decay time
T_2	Coherence decay time
$T_{2,PP}$	Reduced dephasing time due to prepulse
TS	Linear translation stage
VB	Valence band
$u_{\nu,\vec{r}}$	Cell function
WS	Woofer speaker
X	Fundamental exciton

Acknowledgements

First and foremost, I would like to thank my supervisor Kimberley C. Hall for her guidance over the duration of my graduate studies. I wish to thank Jacek Furdyna and his group for growing the samples investigated in this thesis work, and Murat Yildirim for constructing the optical setup used in conducting these experiments.

I would like to acknowledge my fellow group members Angela, Reuble, Tristan, Mat, Eric, and Luke for their assistance in the lab. In particular, I would like to acknowledge Luke who assisted me in collecting the data presented in this thesis work.

Finally, I would like to thank my family for their past, present, and continuing support throughout my studies.

Chapter 1

Introduction

1.1 Overview

The relaxation processes of charge carriers (electrons and holes) in semiconductors play a central role in electronic and optoelectronic devices made from these materials. The photoconductivity of a material is an important parameter in the development of photodetectors, and describes the change in conductivity of a material when exposed to optical radiation. The conductivity of a material can also be controlled with the application of an electric field, which is the basic concept of the field-effect transistor. These devices are made from a sandwich of different semiconductor layers, which are arranged in such a fashion that precise application of an electric potential can lead to rapid changes in the conductivity, making these devices appealing for applications in fast electrical switching and signal amplification. The transport properties of a material (*e.g.* conductivity) which dictate device performance, are ultimately governed by the various scattering processes present, such as interactions between carriers, between carriers and crystal vibrations (phonons), and between carriers and defects. The timescales these processes occur on are very short, and are only accessible using ultrafast optical techniques. The generation of very short light pulses on the order of femtoseconds has permitted the detailed investigation of these rapid processes, and has uncovered the underlying mechanisms responsible for transport and relaxation of charge carriers.

One of the most well-characterized semiconductor materials for the above applications is GaAs, which can be grown in atomically flat layers using a technique called molecular beam epitaxy. During the early 1990's, it was shown that if GaAs is grown at a lower temperature than usual (about 200°C in comparison to 600°C), the material properties are modified considerably [1, 2, 3]. These modified properties make this so-called low-temperature grown GaAs (LT-GaAs) attractive for applications such as ultrafast photodetectors because LT-GaAs-based devices exhibit larger bandwidths

(derived from shorter response times), and smaller dark currents (derived from lower mobility) than conventional semiconductor platforms. In addition to photodetection, ultrafast (sub-ps) electrical pulses can be generated using LT-GaAs based photoconductors, making this material appealing for application to THz photonics applications [4].

During growth, the lower substrate temperature reduces the surface mobility of the Ga and As atoms such that when another layer of atoms is deposited on the crystal, As can be trapped in nonstoichiometric bonding configurations, such as replacing a Ga atom in the lattice or occupying a vacant crystal location. Large densities of unintended As incorporation (*i.e.*, defects) are present in LT-GaAs because, in conjunction with nonstoichiometric bonding, large arsenic overpressures (As:Ga > 1) are required to generate high quality crystalline GaAs. In as-grown LT-GaAs, the majority of these defects are introduced as point defects and clusters. These defects introduce trapping centres than can rapidly capture an optically-injected electron (on a time scale of a picosecond or less, much faster than the electron-hole recombination time in clean GaAs, which is appoximately 1 ns). The associated fast response time is attractive for all-optical switching [5], fast photodetectors [6, 7, 8], and THz sources and detectors [4]. These defects also increase the resistivity of LT-GaAs compared to GaAs. This is attractive for photodetector applications, because the high resistivity leads to smaller dark currents, resulting in smaller noise currents and a corresponding higher signal-to-noise. The possibility of such applications has led to a comprehensive research effort aimed at understanding the fundamental properties of LT-GaAs [5, 7, 9, 10, 11, 1, 12, 13, 14, 15, 16, 17]. The nature of the primary defect (EL_2) has been studied using IR absorption [11, 13], Hall-effect techniques [11], and photocapacitance measurements [10], and the influence of local potential fluctuations in this material tied to these defects has been studied both experimentally [10, 15] and theoretically [9]. Among these studies, linear and ultrafast nonlinear optical techniques have played a central role [5, 10, 11, 1, 12, 13, 14, 18, 19, 20]. The influence of defects on the trapping and recombination times has been investigated using incoherent ultrafast pump probe techniques [5, 14]. It has also recently been shown that growth at low temperature permits the incorporation of magnetic dopants such as Mn [21], leading to magnetic properties of interest for new magneto sensitive electronic and

optoelectronic devices (so-called spintronic devices) [22]. This discovery has motivated more recent studies into the influence and nature of defects on the electronic and optoelectronic properties of low-temperature grown semiconductors [23, 24, 25].

Despite the above studies, little is known about the coherent response of LT-GaAs. Four-wave mixing techniques allow one to measure the timescale for decay of coherence of optically-injected electron-hole pairs. Since the dephasing process is mediated by the strongest (i.e. fastest) scattering events, these techniques provide the most direct approach to measuring the time scale of these scattering processes. The first four-wave mixing experiment on LT-GaAs was recently reported [16]. Although the focus of this work was the influence of Mn on the electronic structure and dephasing time in LT-GaMnAs, reference measurements on a sample without Mn revealed a discrete state at the energy of the exciton in GaAs. An exciton is a bound state of an electron-hole pair that has an energy a few meV below the band gap due to the Coulombic binding energy. No such excitonic feature is observed in linear absorption experiments on LT-GaAs [19], so this observation of such a feature using the *nonlinear* technique of four-wave mixing is intriguing. Since the nonlinear band edge response of LT-GaAs is the basis for applications to THz sources and all optical switching, and since the excitonic response is of fundamental importance to the overall optical properties of this material, experiments that elucidate the nature of the excitonic response in LT-GaAs are required.

In this thesis work, the coherent dynamics of the fundamental exciton in a low temperature grown III-V semiconductor (GaAs) has been experimentally investigated. Four-wave mixing experiments performed over a wide range of excitation conditions have revealed the effects of many-body interactions on the fundamental exciton in LT-GaAs. Several tailored experiments have been performed that directly target key features tied to many-body effects. A series of prepulse and polarization studies have directly uncovered the importance of excitation-induced dephasing, which is shown to lead to the dominant contribution to the four-wave mixing signal at the exciton. The insight provided by the results presented in this thesis will aid in the understanding of the coherent response of fundamental excitons in LT-GaAs and other low-temperature grown semiconductors (*e.g.* GaNAsSb [6], InGaAs [26], and InP [27]).

1.2 Influence of Disorder on the Optical Properties of LT-GaAs

The optical properties of a semiconductor are determined by the electronic band structure. Prior to discussing the optical properties of LT-GaAs, it is instructive to consider the band structure of high-temperature grown GaAs. The full band structure of GaAs is shown in Fig. 1.1(a). The highest energy point in the valence band and the lowest energy point in the conduction band occur at the same point in the Brillouin zone, referred to as the Γ point (Fig. 1.1(b)). These are separated by the band gap energy, corresponding to an energy range in which no electronic states exist. For optoelectronic device applications, the focus is on energetic transitions near the band gap. A simplified band edge diagram for GaAs is shown in Fig. 1.1(c), indicating three doubly-spin degenerate valence bands (heavy-hole (HH), light-hole (LH), and spin-orbit split-off (SO)) and a single doubly-spin degenerate conduction band (C). At 10 K, the energy gap in GaAs is 1.519 eV [28]. GaAs is classified as a direct band gap semiconductor because the critical points of all four bands are vertically aligned at the Γ point in the band structure. The HH and LH bands are energetically indistinguishable at the Γ point but the SO band is 0.34 eV lower due to spin-orbit coupling.

Studying optical transitions in semiconductors can reveal information about the electronic structure as well as the dynamic evolution of electronic excitations following optical excitation. Optically-induced transitions can occur if an incident photon has sufficient energy to promote an electron from the valence to conduction band. When such a optical transition occurs, an electron vacancy (hole) is created in the valence band that is coupled to the excited electron in the conduction band via the attractive Coulomb potential between the electron and hole. This attractive potential leads to the formation of a charge-neutral quasiparticle called an *exciton* that behaves similarly to a hydrogen atom, with corresponding discrete bound states with energies smaller than the band gap due to the Coulomb binding energy. Because an exciton corresponds to a Coulomb-coupled electron-hole pair, each valence band has its own exciton associated with it. The heavy hole and light hole excitons are approximately degenerate in bulk GaAs and are collectively referred to as the fundamental gap exciton. It is represented by the level indicated by an X in Fig. 1.1(c) and 1.1(d). In bulk GaAs, the fundamental exciton has a binding energy of 4 meV.

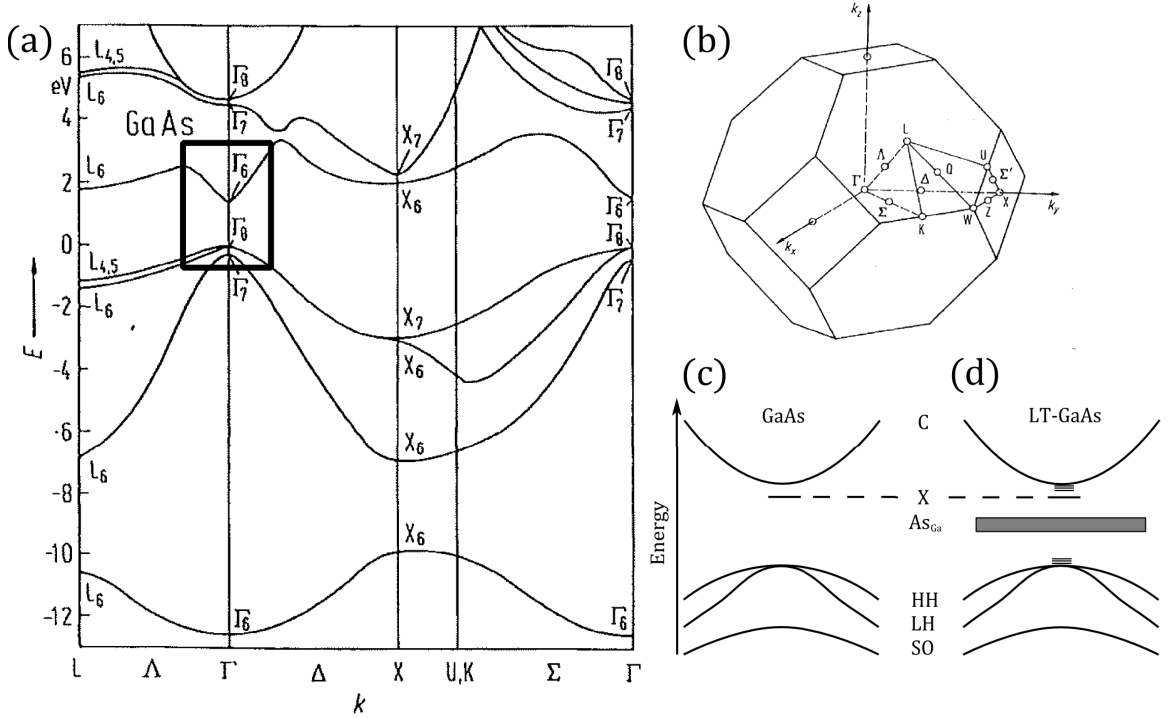

Figure 1.1: (a) Full band structure of GaAs calculated using a pseudopotential technique (adapted from [29]). (b) The corresponding $\vec{k}$ points in the band structure shown in the Brillouin zone (adapted from [29]). (c) A simplified diagram of the band structure that is highlighted by the black box in (a). (d) The band structure near the band edge in LT-GaAs. Low-temperature growth leads to the addition of the defect states As_{Ga} and band-tailing states. The former corresponds to a deep donor band, represented by the shaded rectangle. The latter is represented pictorially as flat lines near the conduction and valence bands. The bands are labeled as follows: As_{Ga} - Arsenic defect band, C-Conduction band, HH - Heavy-hole valence band, LH - Light-hole valence band, SO - Spin-Orbit Split-Off, X - fundamental exciton.

The band structure of LT-GaAs is considerably more complicated than that of GaAs due to the presence of defects introduced during low-temperature growth. Low-temperature grown GaAs epilayers are typically grown using molecular-beam epitaxy (MBE) with the substrate held at 200−300°C. In contrast, high quality GaAs epilayers are typically grown at 600°C. The band structure near the edge of the conduction and valence band in LT-GaAs is shown in Fig. 1.1(d). During low-temperature growth, point defects are introduced into the GaAs host crystal that greatly influence the conduction properties of electrons. Excess arsenic can be incorporated by replacing a Ga atom with an As atom, leading to the creation of As_{Ga} antisites. Because As

is a type V atom, which has five bonding electrons, when it replaces the type III atom Ga, two electrons are left over from bonding and can contribute to conduction leading to additional energy states that are located close to the middle of the GaAs band gap. Because the As_{Ga} can contribute, or *donate* two electrons to conduction, the As_{Ga} defect is called a double-donor. For low defect concentrations, the As_{Ga} has two nondegenerate energy levels at 0.52 eV and 0.75 eV above the valence band that correspond to the neutral and positive ionization states of the As atom. At very high concentrations typical in LT-GaAs ($\geq 10^{19}$ cm^{-3}) [30], the associated localized wavefunctions of these mid-gap donor states can overlap spatially, leading to the formation of bands that are energetically centred approximately at 0.5 eV above the valence band edge. The associated bands are represented by the grey bar in Fig. 1.1(d). Additionally, arsenic can be introduced as interstitials; an As atom can occupy a site where there was originally no atom. A cluster of As atoms can also form, corresponding to a group of tightly spaced point defects. In LT-GaAs these defects are spread throughout the crystal and cause local potential fluctuations that lead to smearing of the valence and conduction bands via the creation of localized states near the edges of the conduction and valence bands inside the band gap [14, 31]. These localized states, or band tails, are represented by a series of lines near the edges of the conduction and valence band in Fig. 1.1(d). Defects are problematic in optical studies because they can lead to additional transitions that can obscure the absorption spectrum tied to band to band transitions, including transitions between the As_{Ga} impurity band and the conduction band and between band tail states in the valence and conduction bands. As discussed in detail in Chapter 2, in stark contrast to GaAs, linear optical experiments on LT-GaAs [14, 16, 19] do not display an excitonic signature, and there are strong contributions to absorption below the band gap, obscuring the band edge.

1.3 Four Wave-Mixing Techniques (FWM)

The optical technique used in this thesis is degenerate two-pulse FWM. A schematic representation of the geometry of a FWM experiment is shown in Fig. 1.2. In such an experiment, two excitation pulses with the same center frequency (derived from a single laser source) characterized by wavevectors $\vec{k}_1$ and $\vec{k}_2$ and electric fields $\vec{E}_1$

and $\vec{E}_2$, are used to excite electron-hole pairs in a semiconductor sample. In the simplest case, the electric fields of the two pulses are linearly-polarized in the same direction, *e.g.* in the $\hat{\mathrm{Y}}$ direction, as indicated in Fig. 1.2. Interference between the two electric fields at the sample creates a spatial modulation of the total intensity in the $\hat{\mathrm{X}}$ direction, resulting in a corresponding modulation in the density of electron-hole pairs excited by the pair of pulses. The index of refraction for light resonant with these excited transitions is modified by the presence of these excited carriers, and so the two pulses together create what can be physically viewed as an optical grating, also referred to as a carrier density grating or population grating. A portion of $\vec{E}_2$ can be diffracted by this grating, resulting in emission in the direction $2\vec{k}_2 - \vec{k}_1$ that can be directly measured using a highly-sensitive photodetector. This process is referred to as self-diffraction since $\vec{E}_2$ participates in both writing the grating and diffracting from it. The detected signal results from a third-order nonlinear interaction in the semiconductor (*i.e.* a $\chi^{(3)}$ process, as described in Chapter 2). In particular, one photon from each pulse participates in writing the grating, and diffraction of a third photon from the second pulse then leads to a polarization density in the sample that emits an output wave along $2\vec{k}_2 - \vec{k}_1$. This output wave constitutes the *fourth* field involved in the process, leading to the name *four-wave mixing*.

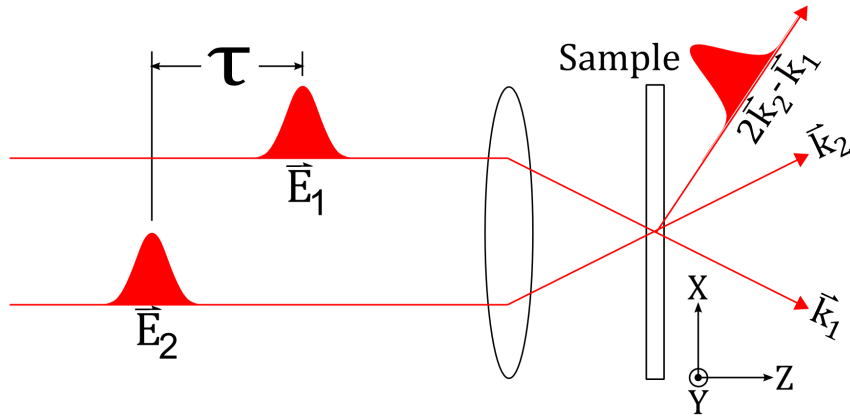

Figure 1.2: A schematic representation of a typical two-pulse four-wave mixing experiment is shown. Due to an interference of the two electric fields along directions $\vec{k}_1$ and $\vec{k}_2$, a third electric field along $\vec{k}_2$ is self-diffracted off of this interference, and projected along the $2\vec{k}_2 - \vec{k}_1$ direction.

It is possible to induce a FWM signal when the pulses $\vec{E}_1$ and $\vec{E}_2$ are not overlapped in time. If $\vec{E}_2$ arrives at a time delay τ relative to $\vec{E}_1$, then $\vec{E}_2$ can still interfere with the remaining polarization induced by $\vec{E}_1$ and diffract from the resulting optical grating, creating the four-wave mixing signal. This process, however, only occurs to the extent that the polarization from pulse $\vec{E}_1$ remains coherent (*i.e.* that the excited electron-hole pairs still oscillate in phase with the original excitation pulse). As a result, measurement of the FWM signal as a function of the time delay between the two pulses can provide a measurement of the dephasing time (or T_2 time, as distinct from the population relaxation time T_1) for the optical transitions resonant with the laser pulse. These coherent carrier dynamics are isolated from the incoherent (population-related) dynamics by spatial selection along $2\vec{k}_2 - \vec{k}_1$, unlike in an incoherent pump-probe experiment such as differential transmission.

The creation of a carrier-density grating for the case in which both $\vec{E}_1$ and $\vec{E}_2$ are polarized in the $\hat{\mathrm{Y}}$ direction results from the direct interference of the two electric fields (or for nonzero time delay interference of the pulse $\vec{E}_2$ with the polarization induced by $\vec{E}_1$) since all of $\vec{E}_1$, $\vec{E}_2$ and the induced polarization are polarized in the $\hat{\mathrm{Y}}$ direction. The nature of the carrier density grating differs when $\vec{E}_1$ and $\vec{E}_2$ are orthogonally polarized (*e.g.* $\vec{E}_1 = E_1\hat{\mathrm{Y}}$ and $\vec{E}_2 = E_2\hat{\mathrm{X}}$). To understand the result of such an excitation process, one must consider the optical selection rules of the semiconductor. Since the heavy-hole to conduction band transitions are three times stronger than light-hole to conduction band transitions [32], attention will be focused on transitions involving the heavy hole band. The selection rules in this case are depicted in Fig. 1.3(a) and Fig. 1.3(b). Here $|\pm 1/2\rangle$ and $|\pm 3/2\rangle$ indicate the projection of the total angular momentum on the growth direction of the semiconductor structure, and

$$\hat{\mu}_{\pm} = \frac{1}{\sqrt{2}}(\hat{\mathrm{X}} \pm i\hat{\mathrm{Y}}) \tag{1.1}$$

indicates the vector orientation of the matrix element of the dipole operator. The inner product of the dipole moment vectors in Eq. 1.1 with the light polarization vector determines the transition rate for the associated two-level system. In particular, the selection rules for HH-C transitions in Fig. 1.3(b) indicate that right (left) circularly-polarized light excites electrons and holes that are spin-down (spin-up). Since linearly-polarized light is composed of an equal superposition of left and right

circularly-polarized components, linearly-polarized light excites both spin transitions equally. Each spin population has associated with it a particular spatial dependence (across the sample, in the $\hat{\mathrm{X}}$ direction). In a four-wave mixing experiment, excitation using collinearly-polarized pulses (*i.e.* $\vec{E_1} = E_1\hat{\mathrm{Y}}$ and $\vec{E_2} = E_2\hat{\mathrm{Y}}$) leads to spin population gratings that are *in phase* along the X direction, as depicted in Fig. 1.3 (c), leading to a grating in the total (spin averaged) carrier density; however, for the case $\vec{E_1} = E_1\hat{\mathrm{Y}}$ and $\vec{E_2} = E_2\hat{\mathrm{X}}$, the two spin population gratings are out of phase along X, leading to the situation depicted in Fig. 1.3(d). In this case, the total (spin-averaged) population is independent of X (*i.e.* there is no grating in the total spin-averaged carrier density) despite the existence of a spatial variation in the net spin polarization of the optically-excited carriers (*i.e.*, a spin grating). In either excitation polarization geometry ($\hat{\mathrm{Y}}\hat{\mathrm{Y}}$ and $\hat{\mathrm{Y}}\hat{\mathrm{X}}$ for the polarizations of $\vec{E_1}$ and $\vec{E_2}$), the four-wave mixing signal is composed of equal contributions to the total four-wave mixing signal from each spin transition (*i.e.* self-diffraction of the associated circularly-polarized component of pulse $\vec{E_2}$ from the spin population grating it participated in writing). As a result for a simple electric-field diffraction signal, as described above, the magnitude of the total signal is the same for the $\hat{\mathrm{Y}}\hat{\mathrm{Y}}$ and $\hat{\mathrm{Y}}\hat{\mathrm{X}}$ configurations. As discussed below, for many-body related signals, this is not always the case.

There are three measurement configurations in a FWM experiment: (i) time-integrated four-wave mixing (TI-FWM); (ii) spectrally-resolved four-wave mixing (SR-FWM); and time-resolved four-wave mixing (TR-FWM). In a TI-FWM experiment, the FWM emission is detected directly using a photodetector (typically a high-speed photomultiplier tube (PMT)). The PMT is far too slow to resolve the decay of the FWM emission in time, and as a result, it is used to make a measurement of the average signal at each value of the interpulse delay, reflecting the integral of

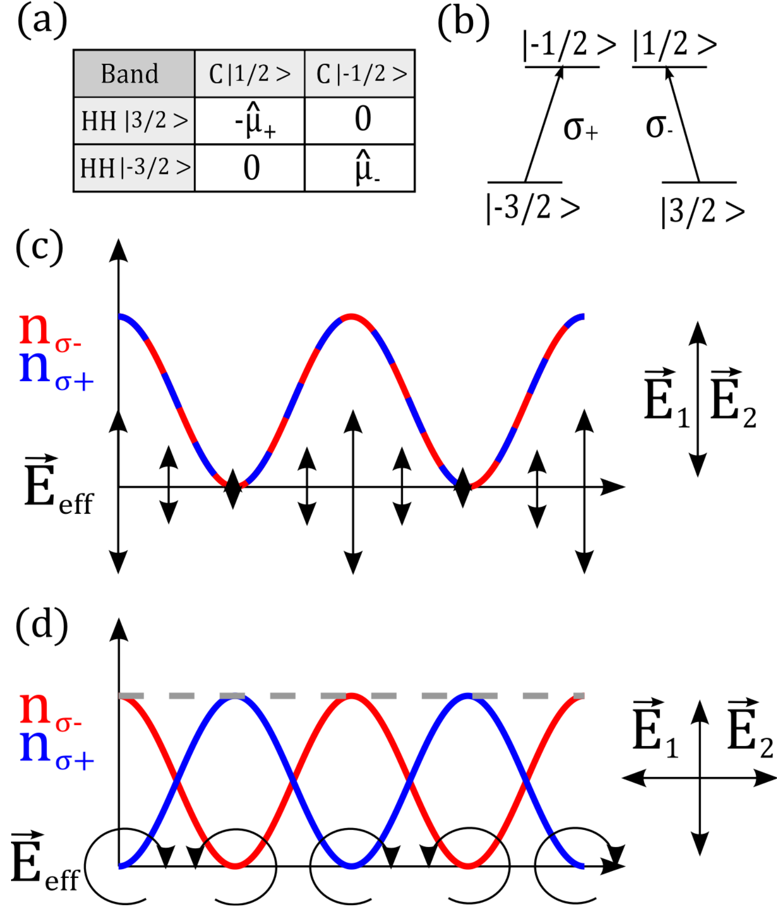

Figure 1.3: (a) Table showing the matrix elements of the electric dipole operator between heavy-hole and conduction band states. $\hat{\mu}_{\pm} = \frac{1}{\sqrt{2}}\left(\hat{\mathrm{X}} \pm i\hat{\mathrm{Y}}\right)$ where $\hat{\mathrm{Z}}$ is the growth direction of the heterostructure. (b) Optical selection rules resulting from (a) $\sigma+$ ($\sigma-$) indicating transitions induced by right (left) circularly-polarized light. (c),(d) An illustration of the spatial distribution of the excited population across a thin slice of the sample in the $\hat{\mathrm{X}}$ direction. $n_{\sigma+}$ and $n_{\sigma-}$ correspond to the excited populations of the $\sigma+$ and $\sigma-$ exciton transitions given in (b). For co-polarized beams (c), a constructive superposition of the two density gratings occurs. However, in (d) a uniform total (spin-averaged) carrier density is created (dashed line).

the FWM over many pulses from the laser source (*i.e.* an integral over time). (A high-speed PMT is useful for experimental schemes in which the interpulse delay is scanned rapidly: The detector must be fast enough to follow the variation of the time-averaged FWM signal with pulse delay in this case.) In a SR-FWM experiment, the FWM emission is passed through a monochromator before being detected by the PMT detector. This results in a measurement of the amplitude of the component of the FWM signal at each photon energy. In a TR-FWM experiment, the FWM emission is measured as a function of time t directly (rather than pulse delay) using a second copy of the laser pulse (acting as a gate pulse) through sum frequency generation between the gate pulse and the FWM emission. These different configurations provide distinct yet complementary information. For example, SR-FWM is especially useful when exciting a region in the electronic band structure with a structured optical joint density of states, as is the case, for example, in the vicinity of an exciton transition. The nonlinearity of the four-wave mixing signal amplifies this structure in the density of states because the signal is proportional to the dipole moment to the eighth power. TR-FWM provides a means to distinguish between a homogeneously- and inhomogeneously-broadened optical transition, which are shown in Fig. 1.4(a) and (b). The former case corresponds to a spectrally-isolated two-level system (*e.g.* an exciton), while the latter case corresponds to a collection of closely-spaced transitions forming a quasi-continuum (*e.g.* the interband transitions in a semiconductor). The TR-FWM signal differs significantly in the two cases, as shown in Fig. 1.4. If the transition is homogeneously broadened, the resulting signal will promptly decay after arrival of E_2, a process referred to as *free polarization decay*. For an inhomogeneously-broadened transition, the FWM signal will occur at a time after $\vec{E}_2$ corresponding to the relative delay between $\vec{E}_1$ and $\vec{E}_2$. This is frequently referred to as a *photon-echo*, and is caused by interference of the free-polarization decay contributions from transitions at different energies. A theoretical treatment of the four-wave mixing response for both a homogeneously-broadened and inhomogeneously-broadened two-level system was provided by Yajima and Taira [33] based on a density matrix formalism involving the optical Bloch equations (OBE) (described in more detail in Sec. 2.5).

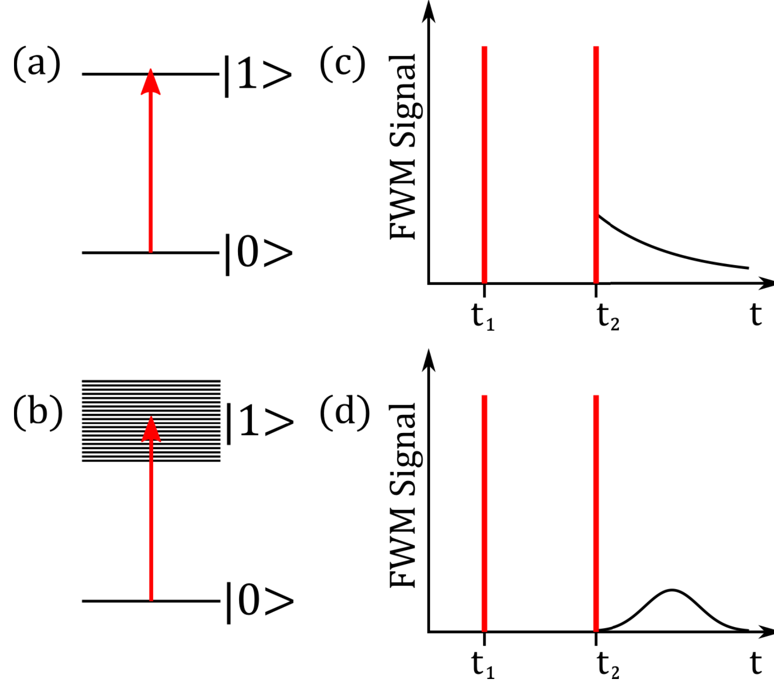

Figure 1.4: (a): A two-level system depicting a collection of discrete resonances with the same transition energy referred to as a homogeneously-broadened transition. (b): A two-level system exhibiting inhomogeneous broadening, corresponding to a distribution of closely-spaced transition energies. (c): Four-wave mixing signal versus time for a homogeneously broadened system. (d): Four-wave mixing signal versus time for an inhomogenously broadened system. The two optical pulses $\vec{E}_1$ and $\vec{E}_2$ are represented as vertical red lines at times t_1 and t_2. The curves in (c) and (d) correspond to the analytical model in [33].

1.4 Four-wave mixing signal contributions arising from many-body effects

Additional light may be detected in the $2\vec{k}_2 - \vec{k}_1$ direction that does not correspond to the simple optical diffraction process described above, but instead is caused by Coulomb-mediated many-body effects. In particular, for the free polarization decay and photon-echo FWM signals described above for non-interacting two-level systems, the electric field of the second pulse is diffracted by the carrier density grating; however, it is also possible for the *polarization* induced by the second pulse to diffract from the grating provided that there are interactions within the system of electrons and holes. This can occur via what is called the Lorentz local field (LF), by which a given optical transition experiences both the applied field due to the optical pulse

and an additional polarization field due to the combined effect of all other excited electron-hole pairs in the system. In addition, the polarization induced by pulse E_2 can couple to the carrier density grating via a scattering interaction referred to as excitation-induced dephasing (EID). This latter contribution is tied to the dependence of the total dephasing rate on the carrier density.

Contributions to the FWM signal that originate from many-body effects are referred to as *interaction-induced nonlinearities.* Because interactions within the semiconductor environment are so strong, these many-body FWM signals are often much stronger than the corresponding non-interacting signals. Their measured dependence on the optical polarization of the exciting laser pulses, photon energy, and interpulse delay can differ significantly from the non-interacting signals described in the preceding section, and as such these interaction-induced nonlinearities can be identified by performing experiments under a range of excitation conditions. It is also possible to exploit screening as a means to selectively turn-off these interactions, further clarifying the origin of the nonlinear signal. Due to the sensitivity of the four-wave mixing signal to many-body effects, a considerable amount of information can be obtained about interactions within the semiconductor through a successful analysis of the self-diffracted FWM signal. Since such interactions have a critical influence on the carrier transport and optical properties in semiconductor devices, FWM techniques have been used extensively to study traditional semiconductors, such as GaAs, InP and Ge [34, 35, 36].

As background for this thesis work, in which FWM techniques are applied to low-temperature grown GaAs, the body of literature concerning the application of FWM experiments in traditional GaAs is described in the next section.

1.5 FWM Studies of the Exciton in Traditional Semiconductors: Previous Work

A wealth of information concerning the optical response of the fundamental exciton in traditional semiconductors (*i.e.*, those grown at high temperatures, resulting in a low density of defects) has been gained through the application of FWM techniques to these materials. As discussed in the preceding section, due to the strong interactions between excited electron-hole pairs within the semiconductor, the FWM signals

observed have been found to be strongly dominated by interaction-induced nonlinearities, providing a platform for gaining insight into these effects. This body of literature falls into two categories depending on which optical transitions are resonant with the exciting laser pulses: (i) experiments carried out under conditions in which primarily excitons are excited; and (ii) experiments in which excitons are excited together with a broad bandwidth of unbound electron-hole pairs above the band gap. In the former case, the center frequency of the laser pulses is tuned below the band gap so that only the tail of the pulse spectrum is used to excite the exciton transition. In the latter case, the center frequency of the laser pulse is tuned above the band gap, overlapping the continuum of unbound electron-hole pair transitions in addition to the exciton resonance. The body of literature concerning the simpler case of (primarily) exciton excitation is summarized in Sec. 1.5.1. When the interband continuum is excited together with the exciton, there exists a complex interplay between contributions to the FWM signal arising from many-body effects and interference resulting from the range of transition energies involved. The associated experiments are highlighted in Sec. 1.5.2. This thesis work concerns studies of the band edge optical response in LT-GaAs under conditions of both exciton and continuum excitation. It is shown that many-body effects greatly influence the dynamics of the exciton, so it is prudent to understand these effects in traditional semiconductors prior to interpreting results in LT-GaAs.

1.5.1 Measurements of the Exciton FWM Response

For a system of excitons, which corresponds to a homogeneously-broadened transition in the semiconductor, the fact that interaction-induced nonlinearities (*i.e.* four-wave mixing signals originating from many-body effects) strongly dominate the four-wave mixing response was clear from many early experiments [37, 38, 39, 40, 41, 42, 43]. Notable observations that deviate from the simple non-interacting four-wave mixing signals described in Sec. 1.3 include: (i) the measurement of a TI-FWM signal at negative time delay [37, 38]; (ii) the observation in TR-FWM of a slow rise of the signal after the arrival of the second pulse [39, 44]; and (iii) a stronger signal amplitude for parallel polarizations in the two excitation pulses ($\hat{\mathrm{Y}}\hat{\mathrm{Y}}$) than for the perpendicular polarization geometry ($\hat{\mathrm{Y}}\hat{\mathrm{X}}$) [40, 41, 42, 43, 44]. For a non-interacting

two-level system, no signal exists in TI-FWM experiments for negative delay since the signal along $2\vec{k}_2 - \vec{k}_1$ corresponds to diffraction of the electric field of the second pulse from the population grating caused by both $\vec{E}_1$ and $\vec{E}_2$ and the first pulse must arrive *first* to generate such a signal. Furthermore, a TR-FWM signal associated with a non-interacting homogeneously-broadened transition is *prompt*, *i.e.* it peaks at the time of the arrival of pulse $\vec{E}_2$ (Fig. 1.4(c)). The TI-FWM signal in the noninteracting case also has the same signal strength for parallel and perpendicular polarizations in the excitation pulses since the two spin transitions contribute equally to the four-wave mixing signal.

All of the above observations that deviate from the simple case of a collection of non-interacting two-level systems were ultimately explained by taking into account excitation-induced dephasing (EID) [45], corresponding to a dependence of the exciton dephasing rate on the total density of optically-excited excitons. The simplest model of this dependence is linear, resulting in a dephasing rate given by

$$\frac{1}{T_2} = \gamma_0 + \Gamma N \tag{1.2}$$

where γ_0 is the dephasing rate tied to coupling of the exciton to phonons and defects, N is the total exciton population density. A population density dependence of T_2 arises from the Coulomb interaction between excitons, which results in exciton-exciton collisions that correspond to phase-breaking scattering events. A density dependence of T_2 was observed for low excitation densities by Schultheis *et al.* [46] and later by Honold *et al.*, [47]. As described in detail in Sec. 2.6, EID leads to an additional contribution to the four-wave mixing signal because the polarization induced by pulse $\vec{E}_2$ can couple to an exciton population density grating via the coefficient Γ in Eq. 1.2 (called the EID coefficient), and thereby diffract from such a grating. The resulting signal contributes together with the free-polarization decay response to the FWM signal. An EID signal is nonzero in TI-FWM experiments for negative pulse delay provided that the polarization from pulse $\vec{E}_2$ persists when pulse $\vec{E}_1$ arrives, since it is the polarization induced by $\vec{E}_2$ that diffracts rather than $\vec{E}_2$ itself, in agreement with the observations of Wegener *et al.* [37] and Leo *et al.* [38]. An EID signal is also characterized by a slow rise of the signal in real time, with a peak that occurs close to the dephasing time T_2, in agreement with the observations of Kim *et al.* [39] and Cundiff *et al.* [44]. The most distinctive feature of an EID signal contribution

(in contrast to a free-polarization decay response) is that the signal is only present for excitation pulses with parallel polarizations ($\vec{\mathrm{Y}}\vec{\mathrm{Y}}$). This is because the exciton-exciton scattering process is independent of the spin orientations of the electrons and holes within the exciton. The lack of a dependence of the scattering rate on spin is reflected by the fact that N in Eq. 1.2 is the *total* exciton density including both spin polarizations; *i.e.* that Γ has the same value for both polarizations. Since no grating in the total carrier density exists in the $\vec{\mathrm{Y}}\vec{\mathrm{X}}$ configuration (as discussed in Sec. 1.3), no EID signal is generated, leaving only the free-polarization decay contribution. A much stronger signal for parallel pulse polarizations in comparison to that for perpendicular pulse polarizations has been observed by several groups [40, 44, 45], indicating that an EID signal dominates the FWM signal for parallel pulse polarizations. In the polarization-dependent experiments by Cundiff *et al.* [44], the TR-FWM signal was also measured for both parallel and perpendicular pulse polarizations. The much smaller signal observed for perpendicular pulse polarizations was found to be prompt, in agreement with a simple free-polarization decay response. This conclusively showed that a different type of many-body related signal tied to local field effects, which like the free-polarization decay signal is expected to have a similar strength for parallel and perpendicular pulse polarizations, does not contribute significantly, in contrast to EID.

Since an EID signal in a four-wave mixing experiment is caused by Coulomb-mediated exciton-exciton scattering, the size of such a signal will be affected by screening. In particular, for a large enough carrier density N, the linear relationship in Eq. 1.2 breaks down because the probability of scattering between excitons is reduced by screening when a sufficiently large density of excitons is present. In Eq. 1.2, this can be taken into account by allowing Γ to decrease with increasing exciton density. This effect was observed by Wang *et al.* [41], who showed that the FWM signal strengths for $\vec{\mathrm{Y}}\vec{\mathrm{Y}}$ and $\vec{\mathrm{Y}}\vec{\mathrm{X}}$ become closer to each other for a sufficiently large excitation density. It is possible to explore the effects of screening by exposing the sample to an extra excitation pulse *before* the primary pulses $\vec{E}_1$ and $\vec{E}_2$. This extra pulse is called a prepulse, and creates a pre-existing population of excitons prior to the excitons excited by $\vec{E}_1$ and $\vec{E}_2$. These extra excitons do not contribute to the population grating generated by $\vec{E}_1$ and $\vec{E}_2$ and, as a result, the only influence of these

preinjected excitons on the magnitude of the FWM signal is through: (i) screening of the EID coefficient Γ in Eq.1.2; (ii) screening of the dipole moment of the exciton; and (iii) an increase in the total dephasing rate. Prepulse experiments were carried out by Schulthesis *et al.* [46] and Honold *et al.* [47], who showed that the dephasing rate was proportional to exciton density in the low excitation regime but that the EID coefficient Γ is reduced by screening by pre-injected excitons when a sufficiently high density of these excitons is introduced by the prepulse.

1.5.2 FWM Experiments For Simultaneous Excitation of Excitons and Unbound Electron-Hole Pairs

It was apparent from more recent experiments [16, 17, 48, 34, 49, 35, 50, 51, 52, 53, 54, 55, 36] that the nature of the FWM response at the exciton changes considerably when a broadband optical pulse is used to excite the exciton together with unbound electron-hole pairs (*i.e.* interband transitions above the band gap). Under these conditions, the unbound electron-hole pairs (also referred to as continuum excitations) contribute to the overall FWM response. Since these continuum transitions form an inhomogeneously broadened two-level system, the four-wave mixing response constitutes a photon echo. In addition to this continuum photon-echo response, the dominant four-wave mixing signal at the exciton tied to excitation-induced dephasing is strongly modified when free carriers are excited together with the exciton. This change in the characteristics of the exciton EID FWM response arises because: (i) the rate of scattering between the excitons and free carriers is larger than the rate of scattering between excitons [46, 47]; and (ii) the exciton-carrier scattering interaction is insensitive to the energy of the free carriers involved [52]. As a result, the EID response at the exciton is considerably larger when continuum transitions are excited. Because scattering between the exciton and the continuum dominates the FWM response of the exciton under these conditions, the associated signal at the exciton is often referred to as the *continuum contribution* (CC). Such an exciton EID response has been observed in four-wave mixing experiments under broadband excitation in GaAs [16, 17, 48, 34, 49, 51, 53, 54, 55], Ge [35, 50], and InP [36]. The most notable difference between a CC response and the EID signal observed when only excitons are excited is that the CC signal is only nonzero for a narrow range of pulse delays

around zero delay. This feature results from destructive interference of EID signal contributions from continuum transitions at different energies [54]. When the bandwidth of the continuum transitions excited by the laser pulse is comparable to the pulse bandwidth, the exciton CC signal becomes as narrow (versus pulse delay) as the pulse autocorrelation; *i.e.* the excitonic feature is pulse-width limited versus delay. These features only became clear when initial TI-FWM four-wave mixing experiments [46, 47] were extended to TR-FWM [39, 56] and SR-FWM [49, 35, 50, 52, 53] configurations, so that the characteristics of the FWM response of the continuum and exciton could be separately measured. A comprehensive theoretical description of the CC was provided by El Sayed *et al.* [54].

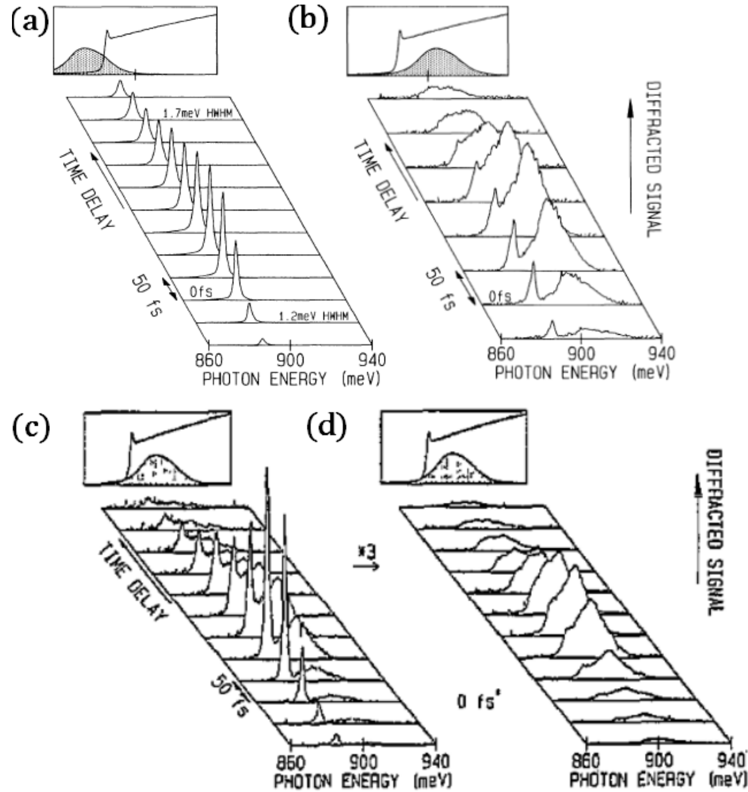

Figure 1.5: Shown are the combined results of a SR-FWM experiment in bulk Ge by Rappen *et al.*[35, 50]. The pulse conditions used for each case are shown above the SR-FWM results. SR-FWM data presented for sub-gap and above gap excitation are shown in (a) and (b). The dependence of the SR-FWM signal on polarization is shown for linearly co-polarized beams in (c) and cross-polarized beams in (d). (a),(b) adapted with permission from [35]. (c), (d) adapted with permission from [50].

The four-wave mixing experiments by Rappen *et al.* [35, 50] illustrate the dominant features of the FWM response when excitons are excited together with a broad bandwidth of unbound electron hole pairs. The results of these experiments are shown in Fig. 1.5. For excitation below the direct band gap, a sharp peak at the excitonic resonance reflects the strong nonlinear response of the exciton, as shown in Fig. 1.5(a). Excitation well above the bandgap (Fig. 1.5(b)) leads to two peaks in the nonlinear spectra that correspond to diffracted signals from excited exciton and continuum states. Strikingly, in Fig. 1.5(b) an exciton signal is present even though there is minimal overlap of the exciton resonance with the pulse bandwidth. Furthermore, in contrast to the non-interacting two-level model, the TI-FWM exciton signal decays much more rapidly in Fig. 1.5(b) than the continuum response. These features are consistent with the expected properties of an EID signal caused by exciton scattering with carriers excited in the interband continuum (*i.e.*, the CC response described above). In a successive publication by Rappen *et al. et al.* [50], the polarization-dependence of the EID FWM response was investigated. In Fig. 1.5(c) and Fig. 1.5(d) are the results of these experiments for linearly co- and cross-polarized configurations. The results for co-polarized pulses display the unique signatures of EID, and are similar to Fig. 1.5(b). In stark contrast to the results in Fig. 1.5(b) and Fig. 1.5(c), the TI-FWM signal at the exciton resonance is absent for cross-polarized beams (shown in Fig. 1.5(d)). This observation revealed the strong EID-related contributions to the exciton FWM response (*i.e.*, that the CC signal dominates for the exciton), and highlighted the importance of many-body effects in determining the coherent dynamics of the exciton.

1.6 Outline of the thesis

In Chapter 2, the linear and nonlinear optical properties of a semiconductor in the context of a two-level system model are discussed. Chapter 3 contains an overview of the experimental apparatus and techniques used to obtain the data contained within this thesis, as well as the methods used for preparation of the GaAs and LT-GaAs samples for optical experimentation. The experimental results are presented and discussed in Chapter 4. Polarization-dependent measurements are presented for a FWM experiment carried out with co- and cross-polarized configurations. The

presented results also include a series of experiments incorporating an optical prepulse with varying prepulse delay and power. Finally, in Chapter 5 a summary of the major conclusions reached in this thesis work is provided, along with recommendations for future investigation in these materials.

Chapter 2

Background Information

2.1 Chapter Overview

This chapter contains a summary of each of the key background concepts required to interpret the experimental results in this thesis work. The first part of the chapter contains a discussion of the electronic and linear optical properties of semiconductors, considering first an idealized semiconductor in Sec. 2.2 appropriate for GaAs grown at elevated temperatures. The influence of defects tied to excess As in low-temperature-grown GaAs modifies the absorption spectrum. These modifications are described in Sec. 2.3. Although the linear optical response (*i.e.*, the absorption spectrum) provides valuable information, the use of short pulses provides access to the dynamic response of a semiconductor. A general discussion of the dynamics following optical excitation is provided in Sec. 2.4. Sec. 2.5 contains the salient parts of a derivation of a four-wave mixing signal for a non-interacting model, following Yajima *et al.* [33]. A phenomenological treatment of excitation-induced dephasing is described in section 2.6, illustrating the mechanism by which excitation-induced dephasing leads to a signal in addition to the noninteracting free-polarization decay response. The development in Sec. 2.6 is based on the findings in El Sayed *et al.* [54] and Wang *et al.* [41]. Finally, an approximate model of the four-wave mixing signal for the experimental conditions considered in this thesis work (simultaneous excitation of the exciton and continuum) is presented in Sec. 2.7, following the development in Allan *et al.* [57]. The predicted characteristics of the four-wave mixing signal in Sec. 2.7 are used to interpret the results of this thesis work in Chapter 4.

2.2 Linear Optical Properties of Semiconductors

The motion of an electron in a semiconductor is described by to the solutions to the Schrödinger equation with a periodic potential corresponding to the repeated

arrangement of screened ion cores. The resulting wavefunctions are called Bloch functions and are given by:

$$\Psi_{\nu,\vec{k}}(\vec{r}) = \frac{1}{\sqrt{V}} u_{\nu,\vec{k}}(\vec{r})\, e^{i\vec{k}\cdot\vec{r}} \quad k_i = 0, \pm\frac{2\pi}{L}, \pm\frac{4\pi}{L} \quad i = x, y, z \tag{2.1}$$

which is a product of a plane wave envelope function that describes the wavefunction of free-electrons, and a cell function $u_{\nu,\vec{k}}(\vec{r})$ that describes the atomic orbitals of atoms in the semiconductor, where ν indicates the band ($\nu = hh, lh, so, c$) and L is the dimension of the semiconductor. The cell functions for a given band have a character (s, p, etc.) that reflects the corresponding bonding or antibonding orbital of the GaAs molecule at each lattice site of the crystal. In particular, the cell functions near zone centre (*i.e.*, near $\vec{k} = \vec{0}$, at the Γ point in Fig. 1.1(a) and (b)) resemble s and p hydrogenic orbitals for the conduction and three highest energy valence bands, respectively.

To obtain a general understanding of optical transitions in a semiconductor, it is instructive to simplify the electronic band structure by considering a two-level model consisting of only the heavy-hole valence band and the conduction band. Carriers in the conduction band will be referred to as electrons, and in the valence band as electron-vacancies, or *holes*. Furthermore, the dispersion relationship for these bands is assumed to be parabolic, a description that is accurate for states near zone centre. In this case, the energy of a carrier in either the conduction ($\epsilon_{c,\vec{k}}$) or the valence band ($\epsilon_{v,\vec{k}}$) is given by:

$$\epsilon_{c,\vec{k}} = \frac{\hbar^2 k^2}{2m_e^*} + E_g \quad \epsilon_{v,\vec{k}} = -\frac{\hbar^2 k^2}{2m_h^*} \tag{2.2}$$

Where m_e^* (m_h^*) represents the effective mass of an electron (hole) in the conduction (valence) band, and E_g is the energy gap at $\vec{k} = \vec{0}$. The effective mass of the carriers differs from the electron mass in vacuum due to coupling of the electron with the lattice of ion cores in the crystal.

Optical interband transitions in semiconductors can occur if the photon energy $\hbar\omega$, where $\hbar$ is Planck's constant, and ω is the angular frequency of the photon, is sufficient to excite an electron from an occupied valence band state $\left|v, \vec{k}\right\rangle$ across the gap into an unoccupied conduction band state $\left|c, \vec{k}\right\rangle$. At $T = 0$ K, only vertical transitions in $\vec{k}$ space are permitted because a photon has negligible momentum when compared to the range of wavevectors used to describe the electron band structure of

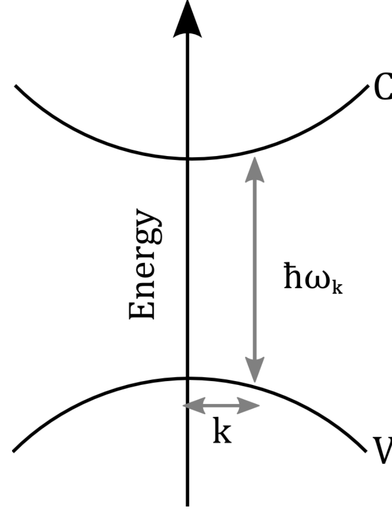

Figure 2.1: In an absorption process, a photon with energy $\hbar\omega$ can excite an electron from the valence (V) to the conduction band (C). The energy of the photon dictates which momentum states can be involved in electronic transitions.

a semiconductor. As a result, optical excitation results in vertical transitions between the valence and conduction bands, and for each electron wavevector $\vec{k}$, the associated states $\left|c, \vec{k}\right\rangle$, $\left|v, \vec{k}\right\rangle$ represent an effective two-level system within the semiconductor. Each such two-level system is an electron-hole pair and represents an optical dipole with a natural frequency ω_k and dipole moment μ_k. This resonance frequency will be larger the higher above the band gap that the electron-hole pair is excited. In addition, according to Fermi's golden rule, energy must be conserved in an optical transition. These two constraints result in the following relationship between the magnitude of the wavevector $\vec{k}$ of the electron and hole involved in the transition and the photon energy:

$$k^2 = \frac{2m_r}{\hbar^2}\left(\hbar\omega_k - E_g\right) \tag{2.3}$$

where m_r represents the reduced mass of an electron hole pair, where $1/m_r$ is given by the sum of the reciprocal effective masses of each carrier. This relationship is illustrated in Fig. 2.1. The total number of transitions that are coupled to an optical laser field is reflected by the frequency spectrum of the laser source and the density of conduction states and valence states involved in the process [58]. Taking this into account, the optical joint density of states for allowed interband transitions in a direct

band gap semiconductor is given by:

$$\begin{aligned} \rho(\omega) &= \tfrac{(2m_r)^{3/2}}{\pi\hbar^2}\left(\hbar\omega - E_g\right)^{1/2} & \hbar\omega \geq E_g \\ &= 0 & \hbar\omega < E_g \end{aligned} \tag{2.4}$$

The absorption spectrum can reveal the coupling strength of light to matter which is a direct reflection of the electronic band structure. The linear absorption spectrum obtained in this way is given by:

$$\alpha\left(\omega\right) \propto H\left(\hbar\omega - E_g\right)\frac{\left(\hbar\omega - E_g\right)^{1/2}}{(\hbar\omega)^2} \tag{2.5}$$

where $H\left(\hbar\omega - E_g\right)$ is the Heaviside step function, and is responsible for the onset of absorption above E_g. As shown by Eqn. 2.5, this absorption is proportional to the square root of the energy of the electron-hole pair (*i.e.*, the difference between the photon energy and the band gap). Equation 2.5 is plotted in Fig. 2.2 (dashed curve) taking into account the band gap of GaAs at 10 K (1.519 eV) [28].

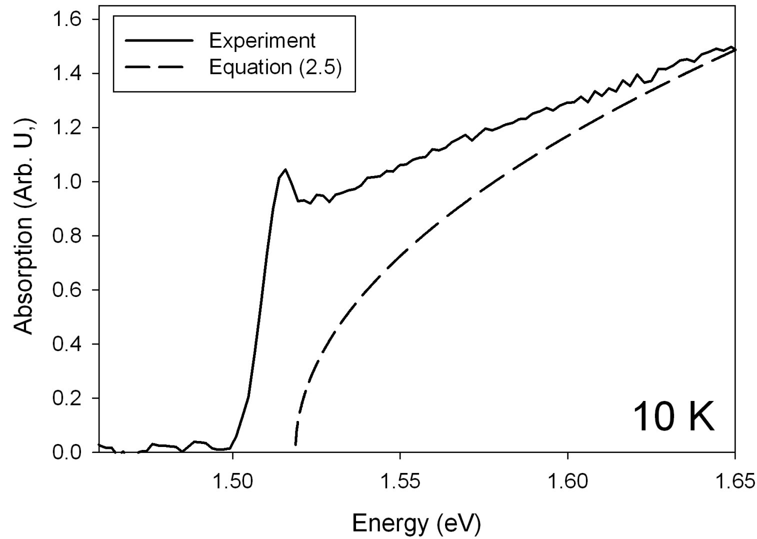

Figure 2.2: The absorption spectrum for interband transitions in GaAs from Eqn. 2.5 (dashed curve) is compared with an experimentally measured absorption spectrum (solid curve). The Coulomb interaction between the electron and hole leads to the formation of excitons and a corresponding sharp absorption peak below the band gap. In addition, the electron-hole interaction leads to Sommerfeld enhancement of the continuum absorption near the band edge, reflected in the experimental data.

The Coulomb interaction between free-carriers has thus far been ignored, but in real systems it can lead to very interesting and important phenomena. The solid

curve in Fig. 2.2 shows the measured absorption curve for bulk GaAs at 10 K. In contrast to the predicted result for interband transitions without the Coulomb interaction (Eqn. 2.5; dashed curve in Fig. 2.2), a sharp peak is visible below the band gap, together with an enhanced absorption above (but near) the band gap relative to the dashed curve. The attractive Coulomb interaction leads to the formation of hydrogenic bound states of electron-hole pairs, *i.e.*, excitons, that dominate the linear optical response in direct band gap semiconductors near the band gap [59]. For linear absorption measurements in bulk GaAs, the fundamental exciton appears as a sharp bump below the band gap. Because the exciton binding energy in bulk GaAs is very small (4.8 meV) and there are various scattering processes for excitons in a real semiconductor at finite temperatures (*e.g.* phonons, defects) that broaden the associated optical transition, higher energy bound exciton states are not separately visible in Fig. 2.2. In addition to the formation of bound exciton states, the attractive electron-hole interaction enhances the optical dipole moment μ_k for unbound electron-hole pair transitions above the band gap. This effect is referred to as Sommerfeld enhancement [58], and is responsible for the strong absorption near the band edge in the experimental data in Fig. 2.2.

2.3 Optical Properties of Low-Temperature-Grown GaAs

The description provided in the preceding section applies to the interband optical response of high purity semiconductors (*e.g.* GaAs), which have a clean band structure (*i.e.*, a low density of defects) due to decades of perfected growth techniques. As discussed in Sec. 1.2, in disordered semiconductors such as low-temperature grown GaAs, the presence of defects leads to additional states in the electronic band structure that complicate the optical response. In particular, excess As leads to a deep donor band tied to As_{Ga} impurities near the middle of the band gap as well as localized states near the edge of the valence and conduction bands, as shown in Fig. 2.3(b).

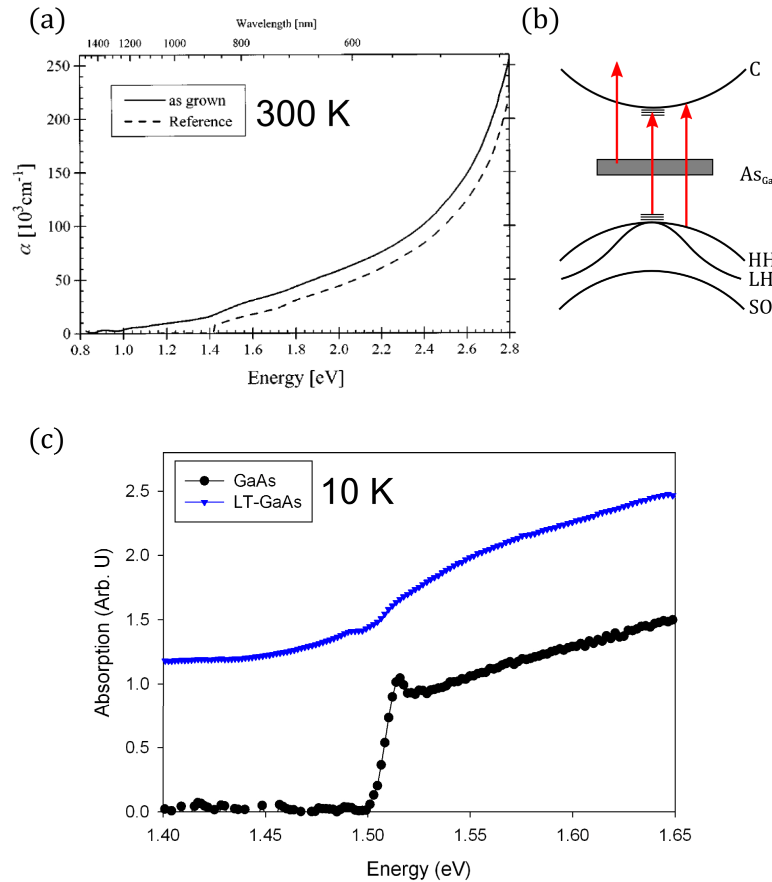

Figure 2.3: (a) A plot of the linear absorption for as-grown LT-GaAs (solid line) and GaAs (dashed line). The smooth linear absorption profile of LT-GaAs is characteristic of the high density of defects present that cause smearing of the band edge. (b) A simple band structure diagram of LT-GaAs at the band edge is shown, illustrating the possible transitions that contribute at energies near the band gap. (c) Linear absorption spectrum of GaAs (black circles) and LT-GaAs (blue triangles) taken at 10K. The plot in (a) has been adapted with permission from [19], as well as the data reproduced in (c) from [16].

The additional defect levels present in LT-GaAs significantly alter the optical response when compared to traditonal high-temperature-grown GaAs. The measured linear absorption at 300 K in LT-GaAs by Streb *et al.* [19] is shown in figure 2.3(a). The corresponding absorption spectrum in the GaAs and LT-GaAs samples in this thesis work at 10 K is shown in Fig. 2.3(c). The most notable difference between the linear absorption in LT-GaAs and GaAs is the appearance of strong absorption below the band gap in LT-GaAs. In particular, the sharp band edge in GaAs is replaced in LT-GaAs by a featureless tail. There are two primary contributions to

absorption in LT-GaAs for energies below the fundamental bandgap of GaAs: (i) transitions involving band tail states; and (ii) transitions from the occupied donor impurity band to states high in the conduction band. These allowed transitions are indicated by vertical arrows in Fig. 2.3(b), together with an arrow indicating the usual interband transition. (Note: The contribution from transitions between states deep in the valence band and unoccupied $\mathrm{As}_{\mathrm{Ga}}^{+}$ states is insignificant because of the small optical cross section for such transitions at cryogenic temperatures [10].) The most significant difference between the absorption spectrum for GaAs and LT-GaAs for the purpose of the present work is the absence of a sharp spectral peak near the band gap at low temperature associated with the exciton in LT-GaAs. This absence has been attributed to large broadening due to potential fluctuations, strong internal field inhomogeneities, and the ultrashort carrier lifetime [14].

2.4 Overview of Relaxation Processes Following Optical Excitation by a Pulsed Laser

The above discussion was focused on the linear absorption spectrum, which is typically measured using a weak continuous-wave optical source such as a lamp or attenuated laser. Insight into the dynamics of an electron-hole pair following optical excitation can be gained by instead using a short optical pulse to inject electron-hole pairs and ultrafast spectroscopy techniques to monitor the resulting dynamic evolution. A short optical pulse may be used to inject an ensemble of such electron-hole pairs into the semiconductor, where the number of electron-hole pairs in a given range of energies is dictated by both the optical joint density of states and the pulse spectrum. An optically excited electron-hole pair will undergo a complex cascade of relaxation processes before the electrons ultimately recombine with the holes, signaling a return to thermal equilibrium. Before any scattering processes occur involving either electrons or holes, the quantum state describing the electron-hole pairs has a well-defined phase that is dictated by the phase of the coherent optical pulse used to excite the system. These phase-coherent electron-hole pairs have associated with them a macroscopic polarization density that persists until scattering processes cause the phase of individual excitons within the ensemble to abruptly change to a random value. The macroscopic polarization associated with the ensemble of excitons decays as the individual

excitons undergo phase-breaking scattering processes until eventually no coherence remains and the macroscopic polarization is zero. The decay time associated with this process is called the T_2 time. The time between initial excitation by the optical pulse and the decay of the polarization is referred to as the coherent regime. The phase breaking scattering processes that contribute to loss of coherence include scattering of carriers with phonons, defects, or other carriers.

The same scattering processes that contribute to loss of coherence will cause the nearly monoenergetic electron-hole pairs to transform into a thermal distribution described by the Fermi-Dirac distribution function. The initial temperature of this distribution will be dictated by the excess energy of the electron-hole pair, *i.e.* the photon energy minus the band gap. Emission and absorption of phonons by these carriers will cause the carrier temperature to equalize with the lattice temperature. Ultimately the electrons and holes will recombine, bringing the system back to thermal equilibrium. The timescale associated with decay of the population of electron-hole pairs is called the T_1 time.

In a four-wave mixing experiment, one detects the light emitted from a particular spatial component of the coherent macroscopic polarization density excited on the transitions in the semiconductor that are resonant with the laser pulse. The four-wave mixing signal represents an optical excitation process that is third order in the light interaction, and the associated spatial component emits radiation along $2\vec{k}_2 - \vec{k}_1$, where $\vec{k}_1$ and $\vec{k}_2$ are the wavevectors for pulses $\vec{E}_1$ and $\vec{E}_2$. This four-wave mixing signal can be calculated using the optical Bloch equations by performing an order expansion in powers of the electric fields $\vec{E}_1$ and $\vec{E}_2$ taking into account their propagation directions [54, 60, 57]. This analysis is presented in the sections below, first for a simple two-level system (*e.g.* an exciton) to illustrate the origins of various signal contributions. This two-level model analysis is first presented considering only the non-interacting terms (Sec. 2.5) and subsequently including additional coupling terms referred to as excitation-induced dephasing (Sec. 2.6). EID is shown to lead to an additional source of diffraction (*i.e.*, an additional four-wave mixing signal). Finally, in Sec. 2.7, the experimental conditions relevant to this thesis work are considered, in which a wide bandwidth of continuum transitions is excited together with the exciton.

2.5 Four-Wave Mixing for a Two-Level System without Interactions

The OBE's for a non-interacting two-level system are given in the rotating wave approximation by:

$$\begin{aligned} \left\{\tfrac{d}{dt}+\gamma_1\right\} n_x(t) &= -\left(\tfrac{i}{\hbar}\right)\left(\mu_x E(\vec{R},t)p_x^*(t) - p_x(t)\mu_x E^*(\vec{R},t)\right) \\ \left\{\tfrac{d}{dt}+\gamma\right\} p_x(t) &= \left(\tfrac{i\mu_x}{\hbar}\right)\left(E(\vec{R},t)\right)\left(1-2n_x(t)\right). \end{aligned} \tag{2.6}$$

where $\vec{E} = E(\vec{R},t)\hat{x}$ is the electric field of the laser pulse at $\vec{R}$, μ_x is the $\hat{x}$ component of the dipole moment, $\gamma = \frac{1}{T_2}$, where T_2 is the dephasing time of the coherence $p_x(t)$, $\gamma_1 = \frac{1}{T_1}$ is the population relaxation time, $n_x(t)$ is the probability at time t that the exciton is populated (*i.e.*, the state occupation) and $p_x(t)$ describes the coherence on the exciton transition. The polarization excited on the exciton transition denoted by $P_x(t)$ is related to the coherence $p_x(t)$ by:

$$P_x(t) = \mu_x p_x(t) \tag{2.7}$$

The rotating wave approximation is appropriate when the laser pulse is resonant or near resonant with the optical transitions in the system, as is the case for the experiments considered in this thesis work. The rotating wave approximation has been implemented in Eqn. 2.6 by setting the reference frequency equal to the exciton resonance frequency.

In a four-wave mixing experiment, the total laser field is the sum of pulses propagating in the $\vec{k}_1$ and $\vec{k}_2$ directions. Considering both $\vec{E_1}$ and $\vec{E_2}$ to be polarized in $\hat{\mathrm{Y}}$ direction, the total laser field is given by:

$$\vec{E}(t) = E_1(t)e^{i\vec{k}_1\cdot\vec{R}} + E_2(t-\tau)e^{i\vec{k}_2\cdot\vec{R}}\hat{Y} \tag{2.8}$$

where τ is the interpulse delay. Due to the dependence of the laser field on $\vec{R}$, the excitation of the system (described by the occupation n_x and the coherence p_x) will also depend on $\vec{R}$. We can take this into account by writing:

$$\begin{aligned} p_x(t) = &\ p_x^{(1)}(t)e^{i\vec{k}_1\cdot\vec{R}} + p_x^{(-1)}(t)e^{i\vec{k}_2\cdot\vec{R}} + p_x^{(3)}(t)e^{i(2\vec{k}_1-\vec{k}_2)\cdot\vec{R}} + p_x^{(-3)}(t)e^{i(2\vec{k}_2-\vec{k}_1)\cdot\vec{R}} \\ n_x(t) = &\ n_x^{(0)}(t) + n_x^{(2)}(t)e^{i(\vec{k}_1-\vec{k}_2)\cdot R} + n_x^{(-2)}(t)e^{i(\vec{k}_2-\vec{k}_1)\cdot R} \end{aligned} \tag{2.9}$$

Here, only terms up to third order in the light-matter interaction have been retained and the superscripts together indicate the order in the light matter interaction as well

as the spatial component reflected by the exponential factor. (For instance, the four-wave mixing signal emitted by the polarization in the $2\vec{k}_2 - \vec{k}_1$ direction is determined by $p_x^{(-3)}$.) We let $N_x(t)$ be the total excited population density of excitons, which is given by the product of the number density of excitons times the occupation $n_x(t)$ such that the exciton concentration in an intensity maximum is equal to the experimentally measured concentration (*i.e.* N_x has units of cm^{-3}, whereas the occupation is unitless with a value between 0 and 1). In this case, $N_x(t)$ will also have a spatial dependence, determined by the spatial dependence of the occupation given by:

$$N_x(t) = N_x^{(0)}(t) + N_x^{(2)}(t)e^{i(\vec{k}_1-\vec{k}_2)\cdot R} + N_x^{(-2)}(t)e^{i(\vec{k}_2-\vec{k}_1)\cdot R} \tag{2.10}$$

Here $N_x^{(0)}(t)$ is the average exciton density, and $N_x^{(2)}(t)$ describes the population grating resulting from $\vec{E}_1$ and $\vec{E}_2$. The polarization resulting from the coherence in Eqn. 2.9 (*i.e.* using Eqn. 2.7) is a source of electromagnetic radiation governed by Maxwell's equations. For example, $P_x^{(1)}(t)$ emits light in the direction $\vec{k}_2$ (collinear with the excitation pulse $\vec{E}_2$) and $P_x^{(-3)}(t)$ emits light in the direction $2\vec{k}_2 - \vec{k}_1$. In a four-wave mixing experiment, selective positioning of the photodetector allows for the isolation of the spatial component $2\vec{k}_2 - \vec{k}_1$ of the light emission after incidence with pulses E_1 and E_2. One can calculate the four-wave mixing signal by inserting Eqn. 2.9 into the OBE's in Eqn. 2.6 and matching different spatial components of n_x and p_x with their respective driving terms. This results in the following differential equation for the component $p_x^{(-3)}$:

$$\left\{\frac{d}{dt} + \gamma\right\} p_x^{(-3)}(t) = 2\left(\frac{i\mu_x}{\hbar}\right) E_2(t-\tau)n_x^{(-2)}(t) \tag{2.11}$$

Eqn. 2.11 shows that $p_x^{(-3)}(t)$ is driven by the second order occupation $n_x^{(-2)}$, and the second pulse ($\vec{E}_2$). The term $n_x^{(-2)}(t)$ describes the grating in the exciton occupation (proportional to the population grating) and the driving term on the right side of Eqn. 2.11 corresponds to diffraction of E_2 from the carrier density grating induced by both $\vec{E}_1$ and $\vec{E}_2$. The equation describing the dynamics of $n_x^{(-2)}(t)$ is given by:

$$\left\{\frac{d}{dt} + \gamma_1\right\} n_x^{(-2)}(t) = \left(\frac{i\mu_x}{\hbar}\right) \left(E_2(t+\tau)p_x^{(1)*}(t) + E_1^*(t)p_x^{(-1)}(t)\right) \tag{2.12}$$

$n_x^{(-2)}(t)$ is driven by coherent coupling (*i.e.* interference via the light interaction) pulse $\vec{E}_2$ with the linear polarization $p_x^{(1)}(t)$ established by pulse $\vec{E}_1$, and the interference of

pulse $\vec{E}_1$ with the linear polarization $p_x^{(-1)}(t)$ established by pulse $\vec{E}_2$. In particular, the polarization $p_x^{(-1)}(t)$ is governed by:

$$\left\{\frac{d}{dt} + \gamma\right\} p_x^{(-1)}(t) = \left(\frac{i\mu_x}{\hbar}\right) E_2(t-\tau) \tag{2.13}$$

It is clear from the above development that: (i) the four-wave mixing signal arises at third order in the light interaction; and (ii) the four-wave mixing signal resulting from diffraction of pulse $\vec{E}_2$ from the carrier density grating. The latter result is the reason for the name "two pulse self-diffraction four-wave mixing".

Analytical solutions to the above set of equations can be found if the pulse envelopes of $\vec{E}_1$ and $\vec{E}_2$ are taken to be described by Dirac functions. This approximation is valid when the relaxation processes are much longer lived than the pulse duration. For semiconductors, which have rapid dephasing rates, this approximation is not accurate; however this approach is nevertheless useful for building intuition. In this case, we can write:

$$E_1(t) = \varepsilon_1 \delta(t) \qquad\qquad E_2(t-\tau) = \varepsilon_2 \delta(t-\tau) \tag{2.14}$$

and the solution for $p_x^{-3}(t)$ is:

$$p_x^{(-3)}(t) = \frac{2i\mu_x^3}{\hbar^3} \varepsilon_2^2 \varepsilon_1^* e^{-\gamma t} H(\tau) H(t-\tau) \tag{2.15}$$

In a four-wave mixing experiment, $p_x^{(-3)}(t)$ is either measured as a function of time (TR-FWM), or as a function of interpulse delay (TI-FWM). The TR-FWM signal may be obtained from Eqn. 2.15 using:

$$\mathrm{S_{TR}}(t) \propto \left|\mu_x p_x^{(-3)}(\tau, t)\right|^2 \tag{2.16}$$

which gives:

$$\mathrm{S_{TR}}(t) = 2\xi e^{-2\gamma t} H(\tau) H(t-\tau) \tag{2.17}$$

where $\xi = \frac{N^2|\mu_x|^8}{\hbar^6} \varepsilon_2^4 \varepsilon_1^2$. The TI-FWM signal may then be found using:

$$\mathrm{S_{TI}}(\tau) = \int_{-\infty}^{\infty} dt \mathrm{S_{TR}}(t) \tag{2.18}$$

which gives (from [33]):

$$\mathrm{S_{TI}}(\tau) = 2\xi e^{-2\gamma\tau} H(\tau) \tag{2.19}$$

The result in Eqn. 2.19 shows that no signal is predicted for negative delay, which is expected since diffraction of pulse $\vec{E}_2$ off of an optical grating generated by $\vec{E}_2$ and $\vec{E}_1$ will not occur unless pulse $\vec{E}_1$ arrives before pulse $\vec{E}_2$. Eqn. 2.19 also indicates that for positive interpulse delays, the generated coherence peaks at the arrival time of $\vec{E}_2$ and exponentially decays as a function of delay at a rate 2γ. γ is the dephasing rate and describes the lifetime of the generated coherence in the system due to pulses $\vec{E}_1$ and $\vec{E}_2$. Such a signal describing an isolated two-level system (*i.e.*, a transition that is homogeneously broadened [60]) in the absence of interactions is commonly referred to as free-polarization decay (FPD).

We can also use the above results when considering an inhomogeneously broadened transition, which corresponds to a series of closely spaced transitions with a range of resonance frequencies, such as for the interband transitions above the band gap. In this case, contributions from these different transitions must be added together. Here we use the electron wave vector to indicate a particular transition energy above band gap via Eqn. 2.3, in which case the TR-FWM signal is found from:

$$\mathrm{S}_{\mathrm{TR}}(t) \propto \left| \sum_{\vec{k}} \mu_k p_k^{(-3)}(\tau, t) \right|^2 \tag{2.20}$$

where $p_k^{(-3)}(\tau, t)$ is the coherence on a particular two-level system at k. The summation in Eqn. 2.20 has the important consequence that the TR-FWM signal is detected after pulse $\vec{E}_2$, at a time corresponding to approximately twice the interpulse delay relative to the arrival time of pulse $\vec{E}_1$. Such a signal is commonly referred to as a photon-echo, and has been observed for interband transitions above the band gap [16, 17]. The time integrated response obtained using Eqn. 2.18 for the interband transitions exhibits prompt decay originating at mutual zero delay, as given by (from [33]):

$$\mathrm{S}_{\mathrm{TI}}(\tau) \propto e^{-4\gamma\tau} \left(1 + \phi \left(\frac{\delta\omega\tau}{\sqrt{\pi}} \right) \right) \tag{2.21}$$

where $\delta\omega$ is the inhomogeneous bandwidth of resonantly excited continuum states, and ϕ is the error function. Comparison of Eqn. 2.21 with Eqn. 2.19 shows that the rate of decay is different for an isolated two level system and a continuum of transitions: In the latter case, the TI-FWM signal decays at twice the rate of homogeneously broadened ones.

2.6 Influence of Excitation-Induced Dephasing on Two-Level System Dynamics

Excitation-induced dephasing is a Coulomb-mediated process by which the electron-hole pair undergoes a phase-breaking scattering process with another carrier. Exciton-carrier scattering is a many-body effect that goes beyond the optical Bloch equations. A rigorous treatment of the optical response of the semiconductor would involve applying the semiconductor Bloch equations, which include other processes such as local field effects. It has been shown through both theoretical analysis [54] and experiments over a wide range of conditions [36, 57, 35, 50] that the influence of EID is the dominant many-body effect governing the FWM response of semiconductors. In this case, the effects of EID can be accounted for in the OBEs by phenomenologically including a density-dependent dephasing rate, *i.e.*,

$$\frac{1}{T_2} = \gamma_0 + \Gamma N_x \tag{2.22}$$

where γ_0 is the dephasing rate of excitons in the absence of an excited population, and reflects the dephasing mechanisms such as scattering of carriers by phonons and defects. The parameter Γ in the second term quantifies the strength of exciton-exciton (or exciton-carrier) scattering. Although the phenomenological treatment of EID in Eqn. 2.22 lacks the rigor of microscopic scattering theories, it has been shown to account for many of the observed features in experimental observations [55].

To understand how EID can lead to a four-wave mixing signal *in addition to* the non-interacting signal discussed in the preceding section, we consider the EID-modified equation describing the spatial component $p_x^{(-3)}$ for the exciton in the $\hat{\text{Y}}\hat{\text{Y}}$ geometry:

$$\left\{\frac{d}{dt} + \gamma + \Gamma N_x^{(0)}(t)\right\} p_x^{(-3)}(t) = 2\left(\frac{i\mu_x}{\hbar}\right) n_x^{(-2)}(t) E_2(t+\tau) - \gamma p_x^{(-1)}(t) N_x^{(-2)}(t) \tag{2.23}$$

Unlike Eqn. 2.11, there are two driving terms on the right side of Eqn. 2.23. The first corresponds to diffraction of pulse $\vec{E}_2$ from the occupation grating $n_x^{(-2)}$, and is the non-interacting signal considered in the preceding section. The second term corresponds to the diffraction of the polarization $p_x^{(-1)}(t)$ induced by pulse $\vec{E}_2$ from the grating in the *total* carrier density $N_x^{(-2)} = \sum n_x^{(-2)}(t)$, where the summation is over all optically-excited transitions, which could include both exciton and continuum

transitions in general. If we restrict our attention to only the isolated two-level system at the exciton, then we can let $N_x^{(-2)}(t) = Nn_x^{(-2)}(t)$ where N is the experimentally measured concentration of excitons. In this case, the solution for δ-function pulses for $p_x^{(-3)}(t)$ (from [45]) is:

$$p_x^{(-3)}(t) = \frac{i\mu_x^3}{\hbar^3}\varepsilon_2^2\varepsilon_1^* e^{-(\gamma_0+\Gamma N^{(0)})t} \cdot \left\{ \begin{array}{l} H(\tau)H(t-\tau)\left[2+\frac{\Gamma N}{\gamma_1}\left(1-e^{-\gamma_1(t-\tau)}\right)\right] \\ +H(-\tau)H(t)\frac{\gamma N}{\gamma_1}e^{2(\gamma_0+\Gamma N^{(0)})\tau}\left(1-e^{-\gamma_1 t}\right) \end{array} \right\} \quad (2.24)$$

where the TR-FWM signal may be found from Eqn. 2.16. Eqn. 2.24 indicates that the four-wave mixing signal including EID is composed of two contributions: (i) The first term in Eqn. 2.24 is the general solution for a non-interacting model leading to free-polarization decay; and (ii) the second and third terms arise from EID effects, where the first corresponds to the EID signal for positive delay and the second gives the EID signal for negative delay. This EID signal is proportional to the EID coefficient Γ. The characteristic features of such a many-body signal are: (i) a slow rise of the signal in t, characterized by the factor $(1-\exp(-\gamma_1(t-\tau)))$; and (ii) the appearance of a signal for negative time delay. As discussed in Sec. 1.5, experiments in III-V semiconductors over a wide range of excitation conditions indicate that the additional signal caused by EID is large compared to the free polarization decay signal for excitons due to the strength of exciton-exciton collisions. One can readily show [45, 54] that for an *inhomogeneously*-broadened transition (such as the interband transitions above the band gap) that the EID signal is *weak* compared to the photon-echo (non-interacting) response due to destructive interference between contributions to the signal from electron-hole pair transitions at different energies. In particular, as pointed out by El Sayed *et al.* [54], EID only contributes significantly at a discontinuity in the density of states (such as at an exciton) due to destructive interference. For this reason, the photon-echo response in Eqn. 2.21 provides a reasonable model for the four-wave mixing response in the continuum.

It is also important to note that the exciton-carrier and exciton-exciton scattering processes, which are mediated by the Coulomb interaction, are not dependent on the spin-state of the carrier involved. In order to properly include EID effects, one would have to include a separate set of OBE's for each optical transition including spin (see Fig. 1.3(b)), and the dephasing rate would contain the total density (including both

spin populations). For example, in the above development, the grating in the *total* exciton population would be given by:

$$N_x^{(-2)} = \sum_s N_s n_{xs}^{(-2)} \tag{2.25}$$

where the index s runs over the two optically active exciton spin states, and $n_{xs}6(-2)$ is the occupation grating for the exciton population with spin s.

For parallel polarized excitation pulses, the population N_s and grating $n_{xs}^{(-2)}$ are equal for both spin states ($s = s1, s2$), and the above development is accurate; however as shown in Fig. 1.3(d), if the excitation pulses are orthogonally polarized, the spin gratings are out of phase such that

$$n_{\text{total}}^{(-2)} = n_{xs1}^{(-2)} + n_{xs2}^{(-2)} = 0 \tag{2.26}$$

In this case, *no EID signal occurs for orthogonally polarized pulses.* In contrast, the free polarization decay (non-interacting) signal remains since this signal corresponds to diffraction of pulse $\vec{E}_2$ from each of the gratings $n_{xs}^{(-2)}$ and $n_{xs2}^{(-2)}$ separately, rather than their sum.

2.7 Four-Wave Mixing under Conditions of Simultaneous Excitation of Excitons and Continuum Transitions

For excitation with a wide-band optical pulse, it is possible to excite excitons and continuum interband transitions simultaneously. In such a case, one must apply the optical Bloch equations to each transition separately, and add up the contributions from all transitions to the total polarization and use this to calculate the four-wave mixing signal. For general laser tuning conditions, the situation is quite complex because the occupations and coherences associated with different two-level systems (with different transition energies) are coupled to each other through the EID coupling. An approximate analytic treatment is possible when the excitation pulses are tuned above the band gap, such that only the low-energy tail of the pulse spectrum overlaps with the exciton. In this case, the total population of electron-hole pairs excited in the continuum is much larger than the total population of excitons, *i.e.*,

$$N_k(t) \propto \sum_k n_k(t) \gg n_x(t). \tag{2.27}$$

In this case, the occupation of the exciton can be taken to be zero for all time, so that only the equation for p_x needs to be solved. In addition, since EID does not contribute significantly to the four-wave mixing signal in the continuum, as discussed in the preceding section, a density-dependent dephasing rate need only be included for the exciton transition. In this case, one can solve the optical Bloch equations for the continuum transitions *separately* from the exciton transition. The equation of motion for the polarization at the exciton is then given by:

$$\left\{ \frac{d}{dt} + i\nu_x + \gamma_x \right\} p_x = \frac{i\mu_x}{\hbar} E(t) \tag{2.28}$$

where

$$\gamma_x = \gamma_0 + \Gamma N \tag{2.29}$$

and $N = \sum_{\vec{k}} n_{\vec{k}}$ is the total population of carriers excited *in the continuum only* since $n_x = 0$. The EID signal at the exciton then corresponds to diffraction of the exciton polarization$p_x^{(-1)}$ induced by pulse $\vec{E_2}$ from the total population grating in the continuum $N^{(-2)} = \sum_k n_k^{(-2)}$. EID in this case leads to a coupling of the exciton polarization to carriers at all energies within the continuum; *i.e.*, the EID process is insensitive to the energy of the electron-hole pair. (The energy-independent nature of the EID coupling process was verified experimentally using partially non-degenerate four-wave mixing experiments by Cundiff *et al.* [52].)

The fact that the EID signal at the exciton is caused by diffraction from a population grating composed of electron-hole pairs excited on the continuum has an important consequence for the dependence of this signal on interpulse delay: In particular, the continuum population grating is only nonvanishing at zero delay, with the consequence that the exciton four-wave mixing due to EID is also only nonzero at zero delay. To see why this is true, we consider (following Allan *et al.* [57]), the solution to the optical Bloch equations for the continuum transitions for the population grating at a given transition $\vec{k}$:

$$n_k^{(-2)}(t) = \mu_k^2 \varepsilon_1 \varepsilon_2 e^{-(E_g - E_b + \hbar\omega_k)\tau} e^{-\gamma_k|\tau|} \left(H(\tau)H(t-\tau) + H(-\tau)H(t) \right) \tag{2.30}$$

where $\hbar\omega_k$ is the transition energy of the electron-hole pair at $\vec{k}$, E_b is the binding energy of the exciton, μ_k is the dipole moment of the continuum transition and γ_k is the (density-independent) dephasing rate of the electron-hole pair. Since γ_k and μ_k

are approximately constant for transitions near the band gap, the result of summing Eqn. 2.30 over $\vec{k}$ will produce a negligible result unless $\tau = 0$, *i.e.*,

$$N^{(-2)}(t) = \sum_{\vec{k}} n_k^{(-2)} = \mu_k^2 \varepsilon_1 \varepsilon_2 H(t-\tau)\delta(\tau) \tag{2.31}$$

In this case, one obtains the following:

$$p_x^{(-3)}(t) \propto N^{(-2)} \frac{\mu_x \varepsilon_2}{\hbar} t e^{-(\gamma + \Gamma N^{(0)})t} H(t) \tag{2.32}$$

The most distinctive feature of this EID signal at the exciton is the appearance of $\delta(\tau)$. For excitation pulses with a finite duration, the above shows that an exciton four-wave mixing signal associated with EID is pulse-width limited versus delay. This is in stark contrast with free polarization decay contributions, which would decay with delay at a rate determined by the dephasing rate. The Fourier transform of Eqn. 2.32 is a squared Lorentzian with a width determined by the total dephasing rate, γ. in the presence of the continuum population ($N^{(0)}$ is the spatially uniform component). This is in contrast with a Lorentzian spectrum, as expected for a non-interacting model. In addition to the exciton EID signal in Eqn. 2.32, a photon-echo response is predicted, given by the non-interacting result (Eqn. 2.21). In this case, the total four-wave mixing signal is the sum of the exciton EID signal and the continuum photon echo response.

The exciton and continuum signal contributions can be separately measured using spectrally-resolved four-wave mixing techniques. The associated signal may be found from:

$$\mathrm{S_{SR}}(\tau,\omega) = \left| \sum_{\vec{k}} \mu_k p_k^{(-3)}(\tau,\omega) + \mu_x p_x^{(-3)}(\tau,\omega) \right|^2 \tag{2.33}$$

where $p_k^{(-3)}(\tau,\omega)$ and $p_x^{(-3)}(\tau,\omega)$ are the Fourier transforms of of $p_k^{(-3)}(\tau,t)$ and $p_x^{(-3)}(\tau,t)$ respectively. The signal at the exciton is a squared Lorentzian, while the continuum produces a broadband signal with a spectral width determined by the bandwidth of the excitation pulses. The exciton response is pulse width limited versus pulse delay, as discussed in above, while the continuum response peaks at positive delay determined by both γ_k and $\delta\omega$ [33]. These predictions are in agreement with the results of Rappen *et al.* (Fig. 1.5) in GaAs.

The above discussion neglected the spin states of the electrons and holes involved in the optical transitons. As discussed in Sec. 2.6, the exciton EID signal vanishes for orthogonally-polarized pulses since no grating in the total population exists in this geometry. (For the case considered here, the grating results from carriers in the continuum, and the total grating vanishes at each $\vec{k}$.) We can use this strong polarization dependence for the exciton EID signal to interpret the experimental results in this thesis work for the four-wave mixing signal at the exciton. For the continuum contribution and orthogonally-polarized pulses, an overall drop in signal is expected due to the smaller magnitude of the $\chi^{(3)}_{\mathrm{XYXY}}$ dielectric susceptibility tensor compared to $\chi^{(3)}_{\mathrm{YYYY}}$, however the *qualitative* features of the signal are not expected to be otherwise affected [35]. This result is in agreement with the experiments of Rappen *et al.* in GaAs, and will aid in the interpretation of the experimental results in this thesis on LT-GaAs since a *relative drop* of the exciton signal in comparison to the continuum response when changing from parallel to perpendicular pulse polarization is an indication that EID is contributing at the exciton.

Chapter 3

Apparatus and Experimental Techniques

3.1 Overview

In this thesis work, the experimental technique of degenerate two-pulse four-wave mixing was used to investigate the charge carrier dynamics in GaAs and low-temperature grown GaAs samples. The main challenge in acquiring a FWM signal is that the signal is very weak, and commonly masked by noise from scattered light from the two excitation pulses. The alignment of the experimental setup, and the techniques used to obtain the high signal-to-noise ratio (SNR) in the results presented in thesis are described in this chapter. The samples under investigation are described in detail in Sec. 3.2 including the procedure for preparing these samples for optical transmission studies. A diagram of the apparatus employed for both pulse measurement and optimization and four-wave mixing experiments is shown schematically in Fig. 3.1. This apparatus was constructed by a former member of our research group (Murat Yildirim) and subsequently modified by the author to enable prepulse experiments as well as measurements of the spectrally-resolved FWM signal as a function of the polarization state of the excitation pulses. Optical pulses of approximately 30 fs duration were used in the four-wave mixing experiments in this thesis work. These pulses were achieved using pulse compression techniques and were measured using zero-background autocorrelation techniques. The setup, alignment, and theoretical basis for these techniques are described in Sec. 3.3. The design and method of a prepulse experiment, including the incorporation of polarization optics into a traditional two-pulse four-wave mixing setup, are discussed in section 3.4.

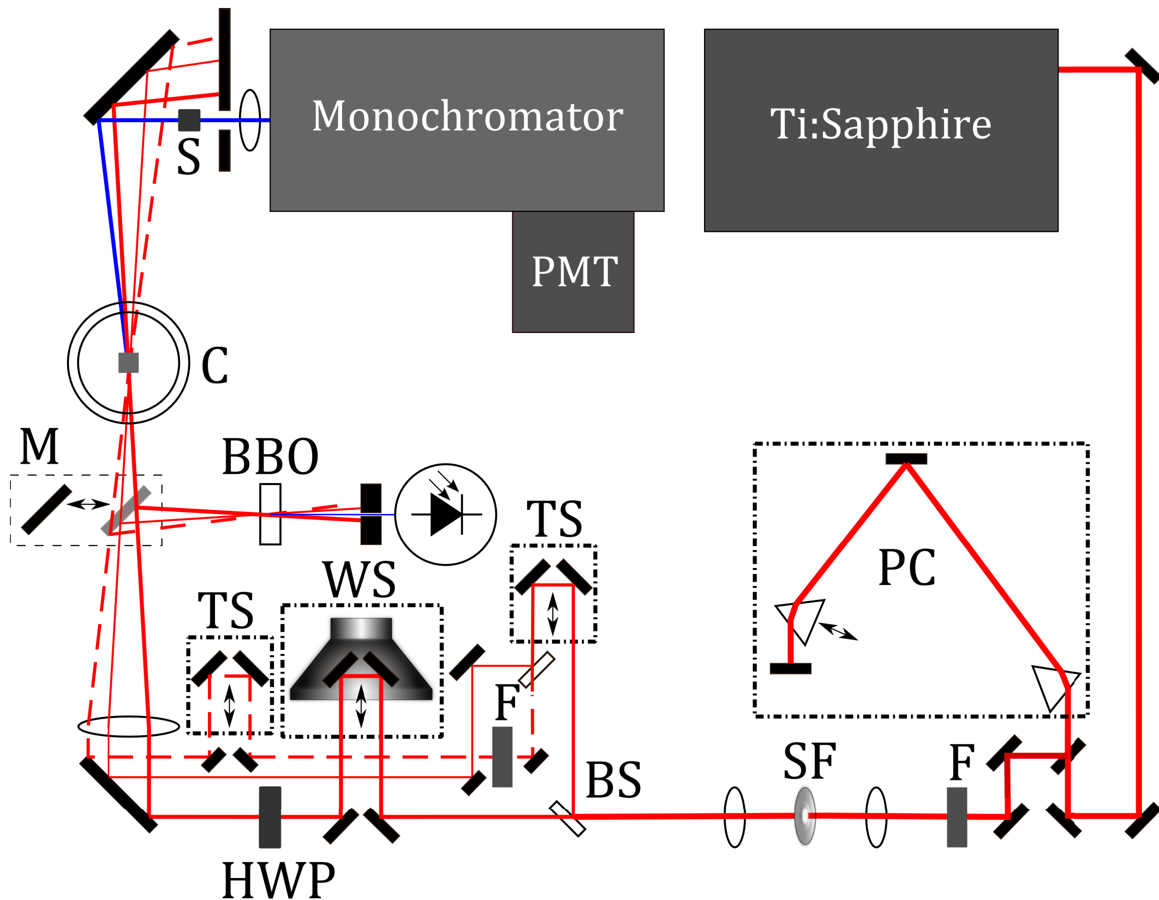

Figure 3.1: A schematic diagram of the four-wave mixing apparatus used in this thesis work. The labels refer to: BBO: Beta-barium borate crystal, BS: Beam splitter, C: cryostat, F: Neutral density filter, HWP: Half-wave plate, PC: Pulse compressor, PMT: Photomultiplier tube, S: Polarized beam splitting cube, SF: Spatial filter, TS: Linear translation stage, WS: Woofer speaker. The three beams incident on the sample are: Thick solid line: $\vec{E}_2$, Thin solid line: $\vec{E}_1$, Dashed thick line: Prepulse. The thick blue line exiting the sample corresponds to the four-wave mixing signal in the $2\vec{k}_2 - \vec{k}_1$ direction. The pulse duration is measured (and spatial overlap is optimized) by inserting mirror M to redirect the excitation beams to an equivalent focus containing a BBO crystal.

3.2 Samples

Under investigation in this thesis were two GaAs thin film samples, one grown at 250°C and the second grown at 600°C. The samples were grown using molecular beam epitaxy by Jacek Furdyna's group at the University of Notre Dame. On a GaAs (001) substrate, a 100 nm buffer layer of GaAs was deposited, followed by 175 nm of $Al_{0.3}Ga_{0.7}As$, and then 750 nm of GaAs, representing the thin film on which four-wave mixing experiments were performed. For the sample grown at high-temperature, the entire structure was grown with the GaAs substrate held at 600 °C. For the low-temperature grown GaAs sample, prior to deposition of the final 750 nm of GaAs, the growth temperature was reduced from 600 °C to 250 °C.

To prepare the samples for optical transmission experiments, the heterostructures were glued sample-side down to a 500 μm thick sapphire window using a UV-curing optical adhesive (Norland 61), which is transparent in the wavelength range of interest (750 - 850 nm). The multilayer structure of LT-GaAs is shown in Fig. 3.2(a). The window and heterostructure, which from this point on will be referred to as the sample, were exposed to a mercury lamp overnight (from the sapphire side) to cure the adhesive (Electro-Lite 10 mW/cm^2 #82469). After curing, the samples were adhered sapphire side down to aluminum pucks using mounting wax (Buehler Mounting Wax #408150) to allow the samples to be placed in the mechanical polisher. The polishing unit has six puck slots to mount samples, however, it was deemed that the safest approach was to polish one sample at a time with the other five slots containing sacrificial GaAs wafers of similar cross-sectional area as the sample. Each of these sacrificial GaAs wafer segments was bonded to sapphire windows as well as to aluminum pucks using the same method as for the sample. Approximately 300 μm of the GaAs substrate was removed in 40 μm increments using the polishing system. Each such increment involved 45 s exposure of the substrate to 900 μm grit sand paper at a pressure of 20 N, while flushing with nanopure water. The remainder of the substrate was removed via chemical etching, resulting in the structure shown in Fig. 3.2(c). The etchant solution was composed of 30% H_2O_2 and 6.28 M citric acid in a 5:1 volumetric ratio, as indicated by the etchant recipe provided by Eric J. Loren at the University of Iowa. Aqueous citric acid was prepared a day prior to etching by dissolving 60.34 g of anhydrous citric acid in 50 mL of nanopure water. The samples

were immersed in the etchant, alongside a magnetic stirrer to keep the solution well mixed during the etching process. This resulted in uniform etching of the substrate at a rate of 20 μm/hour. The etching process was halted once the visible appearance of the sample transitioned from a dull grey to a mirror-like surface, indicating that the stop etch layer had been reached. (The mirror like finish reflects the nominally monolayer flat interface between the GaAs buffer layer and the $Al_{0.3}Ga_{0.7}As$ stop etch layer produced by MBE growth.) The sample was subsequently removed from the etchant, and rinsed with nanopure water followed by spectroscopic grade methanol to remove any remaining etchant.

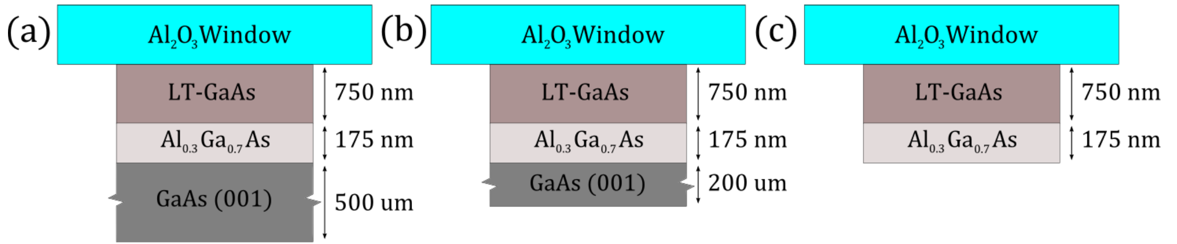

Figure 3.2: The sample at various stages of preparation. The as-grown sample is mounted sample-side down to the sapphire window using optical adhesive, as shown in (a). Mechanical polishing is used to remove approximately 300 μm of the GaAs substrate, as illustrated in (b). In (c), chemical etching removes the remainder of the substrate leaving only the sample and a thin stop etch layer.

Samples were mounted on a brass coldfinger tip inside a liquid helium flow cryostat (ST-300) that was evacuated to 10^{-6} Torr prior to and during cryogenic cooling of the sample. The results in this thesis were all collected with the sample held at 10 K as it gave a good performance compromise between the limit of our cryogenic source (cold gaseous He) and the PID temperature controller responsible for maintaining uniform sample temperature.

The linear absorpton spectrum of the GaAs and LT-GaAs samples is shown in Fig. 3.3. The presented data was collected by a past member of our research group, and subsequently published in Yildirim *et al.* [16]. Linear transmission measurements on both samples were performed using a continuous-wave white-light source (Ocean Optics LS-1) with the samples held at 10 K in a liquid He flow cryostat. In GaAs, the sharp spectral feature located at 1.515 eV corresponds to the fundamental exciton. The sharp onset of absorption for energies above 1.50 eV reflects the clean band

structure in this high quality sample. In stark contrast, the LT-GaAs sample displays significant sub-gap absorption and a gradual transition through the band edge. This sub-gap absorption has been associated with strong defect-related contributions that are described in more detail in Sec. 2.3.

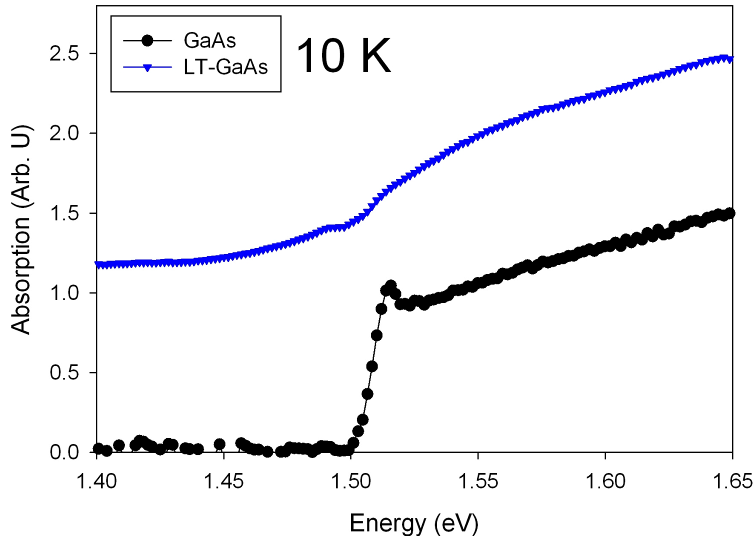

Figure 3.3: Linear absorption spectrum of GaAs (black circles) and LT-GaAs (blue triangles) taken at 10 K. Modified with permission from [16].

3.3 Pulse Measurement and Optimization

3.3.1 Zero-Background Autocorrelation Techniques

To investigate the fast temporal evolution of charge carriers in a semiconductor, very short pulses of light are required. The source of ultrafast pulses in this thesis is a Nd:YO_4 (Coherent Verdi V-18) pumped Ti:Sapphire oscillator (Coherent Mira). The technique of mode-locking is used in the Mira to generate these short pulses, in which the phases of the resonant modes of the laser cavity are equalized through a process called Kerr lens mode-locking. The wide bandwidth of the excited Ti:Sapphire gain medium results in a wide band of cavity modes which results in intense ultrashort Gaussian-shaped pulses of light. Zero-background autocorrelation techniques were used to measure and optimize the pulse duration, to optimize spatial overlap in the four-wave mixing experiments, and to determine the path lengths of the excitation

beams corresponding to zero delay. Autocorrelation techniques were used to determine the widths of the ultrashort optical pulses used in these experiments because conventional electronics (*e.g.* photodetectors) are too slow to directly measure optical pulse widths on these short timescales. When two optical pulses of identical frequency with wavevectors $\vec{k}_1$ and $\vec{k}_2$ are spatially- and temporally-overlapped in a nonlinear crystal (such as a BBO), additional light at double the frequency can be generated in the phase-matched direction $\vec{k}_1 + \vec{k}_2$. This is called *second-harmonic generation.* Detection of the time-envelope of this emission as a function of interpulse delay can reveal information about the pulses used in its generation. Because this is a second-order process, the nonlinear crystal must possess a $\tilde{\chi}^{(2)}$ component in the nonlinear susceptibility tensor. For two optical pulses separated by delay τ and intensities given as $I_1(t)$, $I_2(t-\tau)$, the generated second harmonic signal (*i.e.*, autocorrelation) is given as the cross-correlation of the two pulse intensity envelopes:

$$\mathrm{S}_{\mathrm{auto}}(\tau) = \int_{-\infty}^{\infty} dt I_1(t) I_2(t-\tau) \tag{3.1}$$

For two Gaussian-shaped pulses with FWHM w, the autocorrelation signal envelope is also Gaussian with a FWHM of $\sqrt{2}w$, allowing the laser pulse duration to be determined from the measured width of the autocorrelation. When $\vec{k}_1$ and $\vec{k}_2$ are in different directions, (as is the case described here), the resulting autocorrelation is called the zero background autocorrelation because the second harmonic signals propagating collinearly with each of $\vec{k}_1$ and $\vec{k}_2$ (due to $\vec{E}_1$ and $\vec{E}_2$ alone) are separated spatially from the cross correlation in Eqn. 3.1. In this work, a BBO crystal was used, which is birefringent meaning that it possesses a distinct index of refraction for light polarized parallel and perpendicular to a particular crystal direction (called the optical axis). The BBO crystal was cut so that the orientation of the optical axis is optimum for type I phase matching at 800 nm for normal incidence on the crystal. In this case, the fundamental beams (*i.e.*, $\vec{E}_1$ and $\vec{E}_2$) are “ordinary rays” (polarized in the plane perpendicular to the optical axis) and the second harmonic is an “extraordinary ray” (polarized parallel to the optical axis), often referred to as “oo-e” (or type I) phase matching. The thickness of the crystal is 100 μm, representing a compromise between the intensity of the generated second harmonic light and minimization of pulse distortion in the crystal due to group velocity dispersion.

The autocorrelation is detected by directing the excitation beams used for four-wave mixing to an equivalent focus using mirror M, as shown in Fig. 3.1. The alignment of the autocorrelation therefore coincides with the alignment of the four-wave mixing setup itself. In an optical setup, the direction of the beam is critical. Day-to-day alignment was maintained using a set of irises and mirrors at the entrance to the optical setup. By iteratively adjusting each mirror to align the beam spot on the corresponding iris, the beam direction can be roughly aligned between experimental days. The laser was then passed through a pulse compressor (labelled P.C. in Fig. 3.1), consisting of two prisms. The operation and alignment of the pulse compressor is described below. Two excitation beams, $\vec{E_1}$ and $\vec{E_2}$ are created by splitting the beam after the pulse compressor, and setting up two optical delay lines. The rapid-scan approach was used in these experiments, in which a retroreflector is mounted on the cone of a speaker, allowing the optical path length of $\vec{E_2}$ to be rapidly varied by driving the speaker with a suitable current waveform. In this case, both the TI-FWM signal and the autocorrelation may be collected over a range of time delays using a digital oscilloscope to average multiple scans and to record the resulting autocorrelation. For four-wave mixing experiments, this approach is ideal for studying samples with fast dephasing rates due to the limited range of delays accessible to the speaker motion. The woofer speaker was mounted vertically so that any transverse motion of the retroreflector (which can lead to lateral translation of the optical beam during the motion of the speaker) is minimized.

It is essential that the motion of the retroreflector mounted on the speaker be as linear in time as possible over the range of delays the TI-FWM signal (and autocorrelation) is measured. The motion of the speaker head as a function of time is harmonic, but at a point midway between the displacement extrema, the motion is approximately linear. To change the mutual delay between the two beams so that zero delay occurs in the linear region of the speaker motion, the optical path length of $\vec{E_1}$ was varied using a fixed optical delay line, which consists of a pair of mirrors mounted to a micrometre-controlled linear translation stage. In creating a fixed optical delay line, it is essential to ensure that the axis of motion of the translation stage is parallel to the incoming beam, as otherwise the beam will translate spatially as the micrometer is adjusted, preventing spatial overlap to be maintained as the pulse

delay is scanning. This is ensured by aligning both the incoming beam and the stage with the grid of holes on the optical table. In order to verify accurate alignment, the second-harmonic crystal is replaced by a pinhole and the transmitted power is monitored as the delay is scanned.

Spatial and temporal overlap of the two excitation pulses is required to generate sum-frequency light (and perform an autocorrelation). In order to obtain spatial overlap, parallel alignment of the two optical paths is required so that on insertion of a focusing lens, the two beams are focused to the same point in space. The beam height (with respect to the optical table) and separation was made constant at three different positions on the optical table using a custom alignment tool (shown in Fig. 3.4(b)) The alignment positions are shown as the blue rectangles in the diagram in Fig. 3.4(a). Once the $\vec{E_1}$ and $\vec{E_2}$ beams are made as close to parallel as possible using this approach, a focusing lens is inserted prior to alignment position 2 which focuses the two beams onto the nonlinear crystal. The autocorrelation signal is then located by first ensuring that the BBO crystal is at the correct position along the mean propagation direction of the laser beams. This is verified by using a lens tissue to view the converging beams associated with $\vec{E_1}$ and $\vec{E_2}$ just before and just after the crystal. A high-pass filter is placed immediately after the crystal to block the pump beams so that the sum-frequency light can be observed on a white card just beyond the filter. The ultimate goal was to observe three blue second-harmonic spots on the card, are along each of the two pump beams propagation directions (*i.e.*, along $\vec{k_1}$ and $\vec{k_2}$) and one in the centre ($\vec{k_1} + \vec{k_2}$). The two blue spots collinear with $\vec{E_1}$ and $\vec{E_2}$ are the result of sum frequency generation of each beam with itself and the centre spot (along $\vec{k_1} + \vec{k_2}$) is the desired autocorrelation signal. One must optimize the phase matching angle of the crystal to maximize the intensity of the centre spot. The crystal holder has two axes of rotation that may be adjusted to maximize the generation of the autocorrelation: (i) the angle perpendicular to the normal to the crystals, and (ii) the angle of the crystal face about the incoming light polarization ($\hat{\mathrm{Y}}$ or vertical in the case considered here). The angle in (i) is slowly-varying and can easily be optimized using the second harmonic from the outer two spots. The angle in (ii) (*i.e.*, about $\hat{\mathrm{Y}}$) is the critical angle for phase matching. To determine this angle, one must take into account the fact that $\vec{E_1}$ and $\vec{E_2}$ have different powers. The optimal angle of the

crystal about $\hat{\mathrm{Y}}$ for the centre $(\vec{k}_1 + \vec{k}_2)$ beam may be estimated by ensuring that the intensity of each of the outer two spots is half of its corresponding maximum (*i.e.*, with respect to angle). The corresponding angle is half way in between, allowing it to be approximately located. Once the angle and position of the crystal is set, the delay in $\vec{E}_1$ is scanned using the optical delay stage in the $\vec{E}_1$ path until the autocorrelation signal between $\vec{E}_1$ and $\vec{E}_2$ is visible as a third blue spot located halfway between the other two spots on the white card. The signal, once located, is maximized using: (i) the crystal translation along the mean propagation directions of the two beams; (ii) fine adjustment of the two crystal angles; and (iii) fine adjustment of the incident direction of $\vec{E}_1$, ensuring maximum spatial overlap.

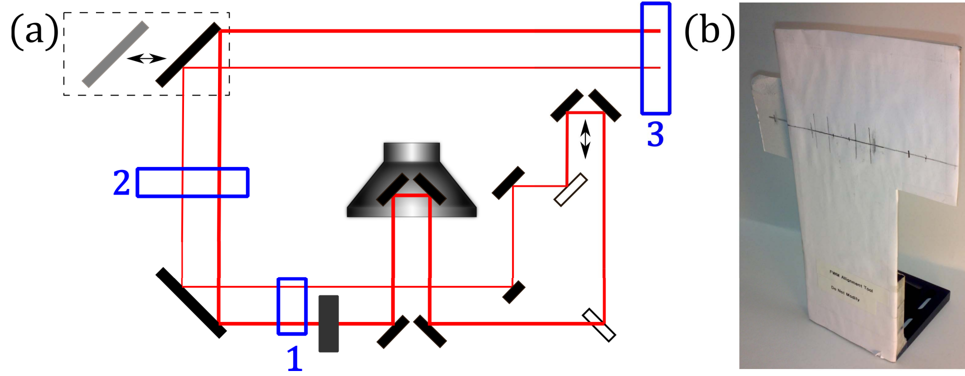

Figure 3.4: (a) A schematic diagram of the portion of the four-wave mixing apparatus used for measurement of the pulse autocorrelation. Parallel alignment of the two excitation beams was performed by placing an alignment tool at three different locations in the optical setup, as indicated by the numbered blue squares. (b) The tool used in the alignment procedure.

3.3.2 Optimization of Pulse Duration using a Pulse Compressor

In transient four-wave mixing studies, the temporal resolution of the experiment is limited by the temporal width of the pulses. When a laser pulse interacts with an optical element (e.g. lens), different frequency components of the pulse can accumulate differing amounts of phase, which leads to a temporal reshaping of the pulse. This is referred to as group velocity dispersion (GVD), and in normal media this value is positive, resulting in lower frequency components traveling faster than higher frequency components, and consequently temporal broadening of the pulse. A pulse compressor compensates by introducing negative GVD. A schematic diagram of a prism pulse

compressor similar to the one in Fig. 3.1 is shown in Fig. 3.5, highlighting the basic operation. A pulse that has been subjected to optical elements with positive GVD is illustrated by the spectrum-coloured oval entering the pulse compressor at position 1 in Fig. 3.5. The wavelength-dependence of the index of refraction leads to a frequency-dependent angle of refraction. By arranging a set of prisms as illustrated in Fig. 3.5, the path lengths of individual frequency components can be adjusted, so that upon exit of the compressor different frequency components are realigned as shown by the second oval at position 2 in Fig. 3.5. Utilizing the approach described by Fork *et al.* [61], the amount of GVD introduced by this setup is given by:

$$\mathrm{GVD_{PC}} \approx \left(\frac{\lambda^3}{2\pi c^2}\right)\left[-4(l_1+l_2)\left\{2\left(\frac{dn}{d\lambda}\right)^2\right\}+4\left(\frac{d^2n}{d\lambda^2}\right)(2D)\right] \tag{3.2}$$

where $l_1 + l_2$ is the interprism separation, n is the index of refraction of the prism material, and D is the $1/e^2$ width of the spatial profile of the laser beam at the first prism. Coarse adjustment of the amount of GVD is performed by translating the second prism, thus changing the interprism distance $l_1 + l_2$ in Eqn. 3.2. Fine adjustment of the GVD is realized by translating the second prism parallel to the symmetry axis, as shown by the double arrow in Fig. 3.5. The optimum amount of negative GVD is obtained when the pulse width, and correspondingly the autocorrelation trace width, is a minimum. For the results presented in this thesis work, pulses of 29 fs were achieved using 74.0 meV bandwidth Gaussian pulses. The autocorrelation and spectrum traces used to measure these values are shown in Fig. 3.6(a) and Fig. 3.6(b) respectively.

3.4 Two-Pulse Four-Wave Mixing

As discussed in Sec. 1.3, in a four-wave mixing experiment two pulses of the same centre frequency with wavevectors $\vec{k}_1$ and $\vec{k}_2$ are used to excite electron-hole pairs in a semiconductor, which are monitored by detecting the self-diffracted polarization emitted in the $2\vec{k}_2 - \vec{k}_1$ direction. The same setup used for pulse measurement is used for four-wave mixing experiments, as discussed above. When performing a four-wave mixing experiment, one begins by locating and optimizing the size of the pulse autocorrelation, as described in Sec. 3.3. On establishment and optimization of the autocorrelation, the pick-off mirror used to reroute the beams to the nonlinear

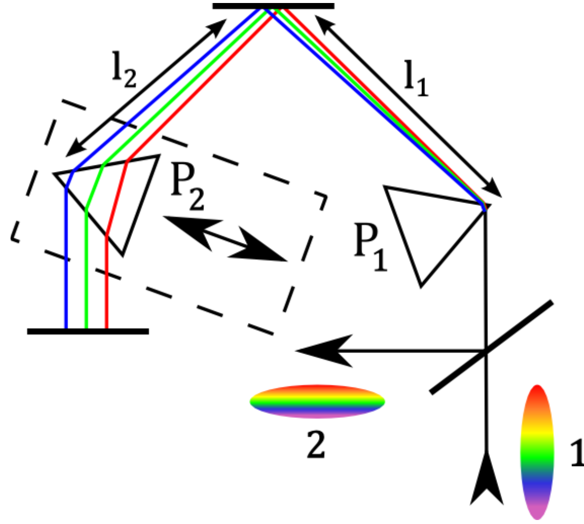

Figure 3.5: A schematic diagram of a pulse compressor containing prisms P_1 and P_2 in a folded geometry. The compressor is used to compensate positive GVD by introducing a uniform wavelength dependent time-delay to each component. Prism P_2 can be moved into the beam path using a micrometre-controlled translation stage, as indicated by the double-ended arrow.

crystal is removed so that the beams are now focused onto the sample in the cryostat. Strong sample inhomogeneities require that the beam position on the sample be scanned while simultaneously observing and optimizing the four-wave mixing emission. A three-dimensional translation stage mounted to the cryostat permitted both transverse and on-axis translation of the sample with micrometre precision.

Spectrally-resolved four-wave mixing experiments were conducted in this thesis work. To perform SR-FWM the diffracted beam in the $2\vec{k}_2 - \vec{k}_1$ direction is collimated and then tightly focused into the entrance slit of a monochromator (Oriel Cornerstone 260). A Czerny-Turner type monochromator was used in these experiments and its operation is described in the following: The entrance slit of the monochromator acts as a point source. Light transmitted through the exit slit is collected by a parabolic focusing mirror and collimated onto a diffraction grating. Individual wavelength components of the light source are diffracted, so that after refocusing with a second parabolic mirror, different wavelength components are spatially separated and isolated by an exit slit. The grating type and slit-widths used in these experiments have yielded a spectral resolution of ± 1 nm as obtained through calibration with a Helium-Neon laser. To perform the calibration, a CW helium-neon laser was focused into

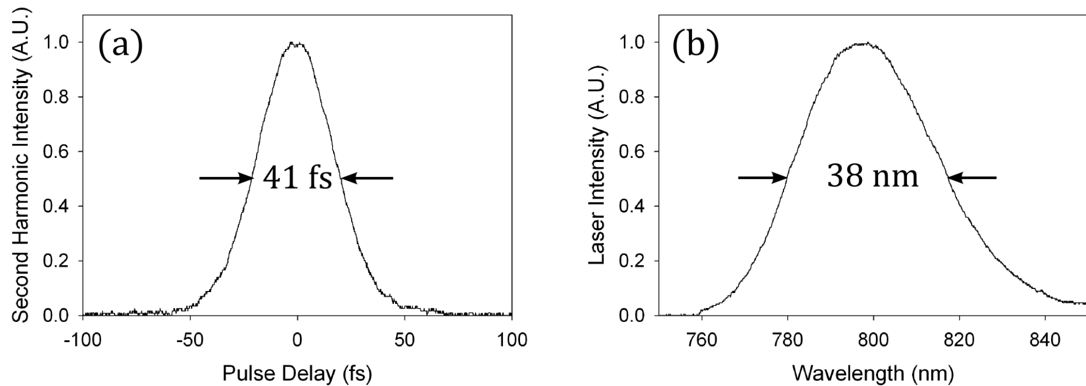

Figure 3.6: (a) Measured pulse autocorrelation. A Gaussian fit to the autocorrelation trace yielded a FWHM of 41 fs, corresponding to a pulse duration of 29 fs; (b) The laser pulse spectrum collected just outside the laser source. For the experiments conducted in this thesis, the laser was centred at 1.553 eV, with a bandwidth of 74.0 meV. The low-energy tail of the pulse does not go to zero due to the laser source.

the monochromator by coupling the helium-neon beam into the FWM beam path using a pair of irises. The helium-neon laser source used produces narrow (spectrally) emission with a centre wavelength at 632.8 nm. The wavelength of light emerging from the monochromator is determined by the angle of the diffraction grating (oriented in the $\hat{Y}$ direction). The relationship between angle and output wavelength is set by the monochromator controller, for which on selection of a specific wavelength the diffraction grating is rotated and ideally that wavelength is projected through the exit slit on the output of the monochromator. If an offset in the grating angle exists, this will be reflected by an offset in the selected wavelength. The offset is minimized by rotating the monochromator, and then scanning the wavelength in the expected range while observing the emission on a white card placed beyond the output coupler. The emission has a Gaussian profile as a function of wavelength and so the peak is difficult to determine accurately with the naked eye. Instead, the centre wavelength is determined by finding the wavelengths for which the signal vanishes and taking the midpoint. In addition to the first order diffracted peak, the second order peak was also used to provide an additional level of calibration.

The power of the FWM signal is very weak and for the samples investigated in this

thesis work, peak powers of 216 nW for GaAs and 1 nW for LT-GaAs were measured, both of which are significantly weaker than the measured transmitted power of 10-15 mW in the E_2 path. In order to detect the weak FWM signal, a photomultiplier tube (PMT) was used because of its high photosenstivity in the near-IR wavelength range. The operation of a PMT is based on two principles: the photoelectric effect; a photon with sufficient kinetic energy to overcome a materials work function can emit excited electrons, and secondary emission; mobile electrons can collide with a material, causing emission of additional electrons. In a photomultiplier tube, a photocathode material generates electrons on incidence with photons, and these electrons are accelerated between a series of charged plates, such that an electron cascade process occurs leading to strong amplification of the initially weak optical signal.

The response time of the detection system (photomultiplier tube) is limited by the intrinsic capacitance in the coaxial cable used to connect the PMT to the oscilloscope, and the input on the oscilloscope itself. A capacitance compensation circuit, designed by Kimberley Hall and constructed by Murat Yilidirim, was utilized on the output terminal of the PMT to compensate for the capacitance in the cables. A circuit diagram of this device is shown in Fig. 3.7.

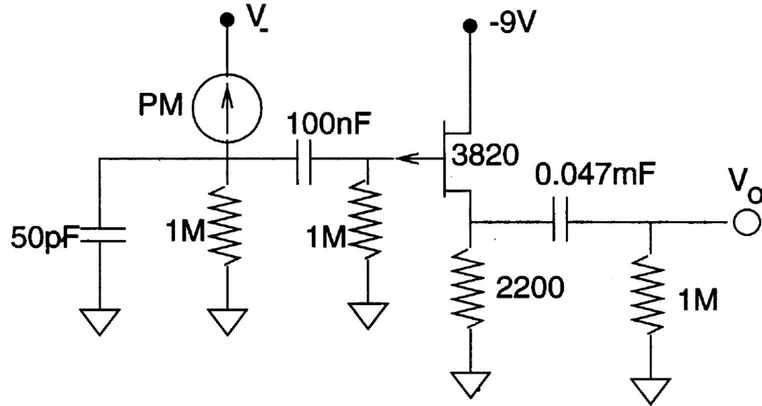

Figure 3.7: A circuit diagram of the compensation circuit used to correct for the response of the PMT. Taken with permission from [62].

Optimization of the signal-to-noise ratio is very important in FWM experiments because the signal is commonly masked in noise from $\vec{E_1}$ and $\vec{E_2}$ by strong scattered light and imperfect laser phase fronts. Noise from scattered light can mostly be removed with proper alignment and careful sample position, but the latter requires

spatial filtering techniques. In an ideal optical experiment, the laser pulse would resemble the lowest order (TEM_{00}) Gaussian beam, which is characterized by a uniform (approximately spherical) phase front. Due to imperfections and clipping on optical elements, distortion of the phase fronts can occur. A spatial filter can be used to remove these unwanted features, which has been implemented in the optical setup. In a spatial filter, light is focused using a lens onto a plane, which radially separates different spatial frequency components of light. A spatial filter (pinhole) placed in this plane can block higher-order $\mathrm{TEM}_{\mathrm{nm}}$ modes, since such modes contain larger transverse wavevector components than the TEM_{00} mode. In this case, on passing to the second lens for recollimation, the beam is a good approximation to a TEM_{00} Gaussian beam. The diameter of the pinhole is selected based on the Gaussian spot size of the TEM_{00} beam; the spot size is determined by the size of the beam entering the arrangement, and the focal power of the lens [63]. It is critical that the spatial filter is located exactly at the beam waist so that clipping of the beam is avoided. In order to verify accurate alignment, the spatial filter is scanned transversely through the optical path while observing the Airy-ring pattern on a white card just past the filter. Uniform, even rings indicate that the pinhole is located on the optical axis. To verify the spatial-filter is at the correct position along the optical axis, the filter is iteratively translated along the optical axis while checking the abruptness to which the beam is sliced when the pinhole is translated horizontally at each position. The ideal position is reach when the beam spot is most sensitive to changes in the horizontal pinhole position. At this ideal position, the beam after the spatial filter resembles a smooth large sized spot.

In addition to the standard two-pulse four-wave mixing experiments, a third optical pulse ($\vec{E_{PP}}$) coincident on the same location on the sample can be used to preinject a population of excited carriers prior to arrival of $\vec{E_1}$ and $\vec{E_2}$. A schematic diagram of this arrangement is illustrated in Fig. 3.8. These are commonly referred to as prepulse experiments, and can reveal important many-body related contributions to the nonlinear response. In order to perform prepulse experiments, a third optical delay line was added into the pre-existing four-wave mixing setup. As shown in Fig. 3.1, the prepulse line is sourced from a non-polarizing plate beam splitter. A micrometre-controlled linear translation stage was used to precisely control the delay of this third

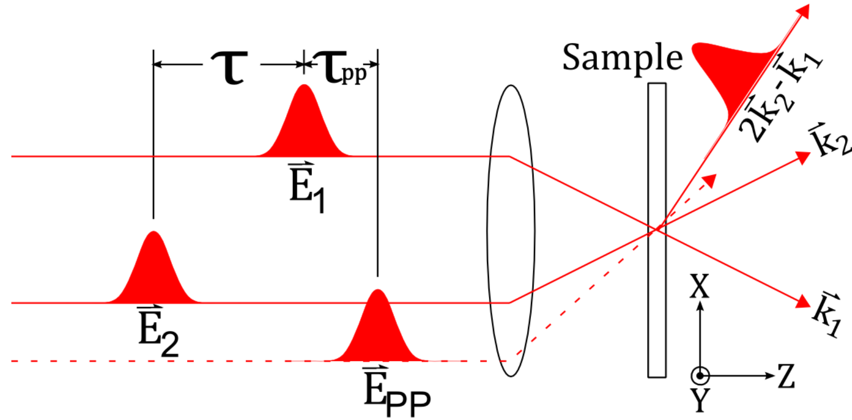

Figure 3.8: A schematic illustration of a two-pulse four-wave-mixing geometry with a prepulse. The two investigatory pulses $\vec{E_1}$ and $\vec{E_2}$ are are separated by an interpulse delay τ. At a time τ_{PP} before (or after) arrival of $\vec{E_1}$ and $\vec{E_2}$, a spectrally-identical prepulse $\vec{E_{PP}}$ injects a population of free-carriers into the system. The prepulse does not affect the phase-matching condition for two-pulse FWM, and so the diffracted macroscopic polarization still lies in the $2\vec{k}_2 - \vec{k}_1$ direction.

line, and its construction and alignment are identical to that for the fixed delay line in the path of pulse $\vec{E_1}$ described in Sec. 3.3. To achieve spatial overlap of the prepulse with the two FWM investigatory beams, an autocorrelation between $\vec{E_2}$ and $\vec{E_{PP}}$ is performed that parallels the procedure outlined in Sec. 3.3. In a prepulse experiment, the prepulse does not contribute to grating formation and so phase-matching conditions imposed on $\vec{E_1}$ and $\vec{E_2}$ are not applicable to $\vec{E_{PP}}$. To achieve perfect spatial overlap with $\vec{E_1}$ and $\vec{E_2}$, the prepulse was scanned into position by adjusting the final mirror and maximizing the strength of the mutual autocorrelation. To prevent any undesirable coherent contributions to the FWM signal, the wavevector of the prepulse is different than $\vec{k}_1$, $\vec{k}_2$, and $2\vec{k}_2 - \vec{k}_1$.

Accurate control of the excited carrier density is necessary to determine the effects of screening and EID in these systems. The amount of absorption was determined from the measured power in each beam before and after the sample position and the reflected power off of the cryostat windows and sample. The pulse fluence was calculated from the measured spot size, repetition rate, and centre wavelength of the optical source. The excited carrier density was estimated based on the thickness of the sample, the spot size of the laser beam at the sample location, and the power absorbed in the sample.

The laser source is horizontally polarized, which is rotated to vertical polarization using a periscope located after the pulse compressor (just prior to filter F in Fig. 3.1). For the polarization-dependent studies, two polarization configurations of $\vec{E}_1$ and $\vec{E}_2$ were investigated: parallel linear and perpendicular linear polarizations. Due to the polarization-selection rules outlined in Hu *et al.* [40], the polarization state of the FWM emission matches that of $\vec{E}_1$, such that to ease analysis of the collected results, the polarization-state of $\vec{E}_2$ was modified using a half-wave plate placed in the $\vec{E}_2$ optical delay line. A half wave plate is a birefringent optical element with a thickness designed to impose a phase shift between polarization components aligned parallel to and perpendicular to the optical axis. In this case, the emerging light will also be linearly-polarized, but at a different angle as set by the orientation of the optical axis of the half wave plate relative to the incident light polarization. It was verified that for arbitrary half-wave plate angle the setup alignment was preserved, so that refraction does not result in significant beam steering.

Chapter 4

Results and Discussion

4.1 Overview

The results of a four-wave mixing experiment performed on GaAs and low-temperature grown (LT) GaAs are presented in this chapter. These experiments were performed under a range of experimental conditions in order to characterize the optical response of the exciton in LT-GaAs and to elucidate the contribution of many-body effects to the four-wave mixing response. In particular, polarization dependent SR-FWM was performed for linearly co-polarized and cross-polarized pulse geometries to illuminate the effect of EID on the excitonic FWM response. The influence of excess electron-hole pairs on the optical response was also examined by exposing the sample to an extra optical pulse prior to the arrival of the two excitation pulses used to generate the FWM signal. These prepulse experiments involved measurement of the change in the signal characteristics as a function of both the power in the prepulse beam and the time of arrival of the prepulse relative to the FWM excitation pulses.

As revealed through this thesis work, a sharp spectral feature is visible at the fundamental exciton in LT-GaAs, in contrast to linear spectroscopy experiments. Unique signatures of many-body related effects were also observed and are shown to be responsible for the excitonic response. These results are supported by similar observed trends in GaAs, which are well-documented in the literature as being attributed to excitation-induced-dephasing (EID). All of the experimental results presented in this chapter, with the exception of the linear absorption measurements, were obtained by the author. The analysis and interpretation of the results were conducted by the author.

4.2 Experimental Results

The linear absorption spectrum for both samples and the pulse spectrum used in

the four-wave-mixing experiments are plotted in Figure 4.1. The linear absorption spectrum is included here with permission from a prior publication [16], and was obtained by extracting the absorption coefficient from transmission experiments using a self-consistent model incorporating Fabry Perot effects. The peak at 1.515 eV in the data for GaAs coincides with the fundamental exciton energy at 10 K [28]. Due to the low density of defects, a sharp band edge is also observed below the exciton in GaAs. The linear absorption spectrum in LT-GaAs is characterized by a smooth featureless response due to the strong contributions to absorption involving defects in this material, as seen previously [19]. In particular, optical transitions between the As_{Ga} mid gap donor band (which is partially occupied with electrons) and the conduction band as well as transitions involving the band tail states contribute strongly to absorption below the band gap (see Fig. 2.3). No exciton response is observed in the linear absorption spectrum for LT-GaAs, consistent with previous work [19]. (Note: the small bump in the data for both samples at approximately 1.49 eV is an artifact of the imperfect cancellations of Fabry Perot oscillations.)

For four-wave mixing experiments, the mode-locked laser source is tuned 35 meV above the band gap of GaAs. Due to the wide 74 meV bandwidth of the femtosecond optical pulses used, this tuning condition is expected to provide a strong response in the interband continuum in both samples. This condition will permit the relative importance of the exciton and continuum signals in GaAs and LT-GaAs to be assessed, and was used for all experimental results presented in this thesis. All of the experiments were also performed with the same average power in the two excitation pulses used to generate the FWM signal, corresponding to 53 mW for $\vec{E}_2$ and 14 mW for $\vec{E}_1$ measured at the sample location.

4.2.1 Spectrally-Resolved Four-Wave Mixing

The four-wave-mixing spectral profile at zero delay between pulses $\vec{E}_1$ and $\vec{E}_2$ is plotted for both GaAs and LT-GaAs in figure 4.2(a), together with the spectrum of the laser pulses. For these data, $\vec{E}_1$ and $\vec{E}_2$ were collinearly polarized in the $\hat{Y}$ direction. The signals have been normalized to the peak values to allow the characteristics of the optical response to be compared between the two samples. (The total four-wave mixing signal is much smaller in LT-GaAs than in GaAs: 1 nW for LT-GaAs,

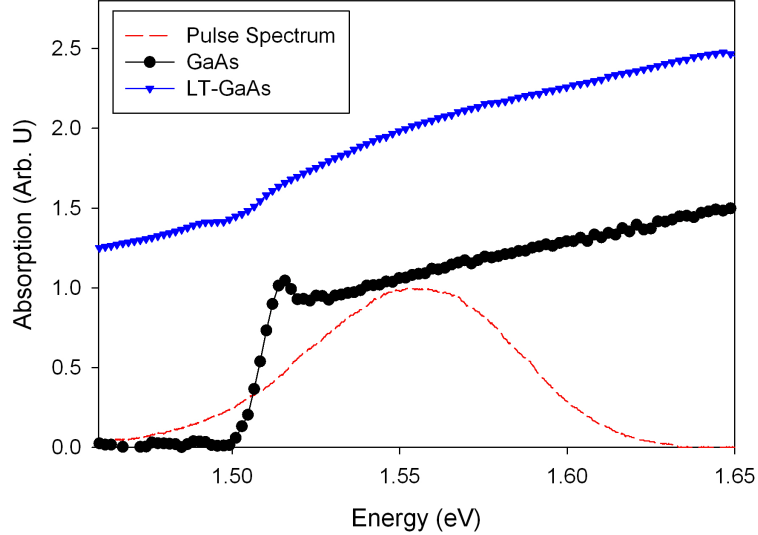

Figure 4.1: Linear absorption spectrum of GaAs and LT-GaAs at 10 K. The dashed red line shows the laser spectrum for the FWM data presented in this chapter. Modified with permission from [16].

compared to 216 nW for GaAs.) The FWM spectrum in GaAs (indicated by black circles) has a sharp peak located at 1.515 eV, which corresponds to the energy of the fundamental exciton at 10 K [28]. There is also a weaker signal at higher energies that may be ascribed to the four-wave mixing response of the interband continuum transitions above the band gap. The shape of the FWM spectrum in LT-GaAs is qualitatively similar to the results for GaAs, with a peak at the exciton energy and a shoulder at higher energies associated with the optical response of the interband continuum. The exciton peak is broader and the continuum response is larger relative to the exciton in LT-GaAs in comparison to the results in GaAs.

The general features of the nonlinear optical response of GaAs in figure 4.2 are similar to the results of Rappen *et al.* [35, 50]. For the four-wave mixing response in LT-GaAs, two aspects are surprising: (i) No signal contributes below the band gap of GaAs despite the presence of pump pulse intensity for lower photon energies (*i.e.*, there is a sharp band edge in the *nonlinear* response, as in the case of GaAs); and (ii) there is a prominent peak at the energy of the exciton. Both of these observations are in stark contrast to the linear optical response of LT-GaAs in Fig. 4.1. In SR-FWM experiments on low-temperature grown GaMnAs, the former has been explained by a

reduced dipole moment associated with transitions between the As_{Ga} impurity band and the conduction band in comparison to the interband transitions [16]. Since the four-wave mixing signal is proportional to the magnitude of the dipole moment to the power 8, the larger dipole moment of the interband transitions (and therefore also the exciton) in comparison to the transitions involving the impurity band causes the interband transitions to dominate the four-wave mixing response. The observation of an optical response at the exciton in LT-GaAs is interesting, given its absence in the linear absorption spectrum. As shown through the course of this thesis work, the ability to observe the exciton in four-wave mixing experiments is a consequence of the sensitivity of the signal characteristics to many-body effects.

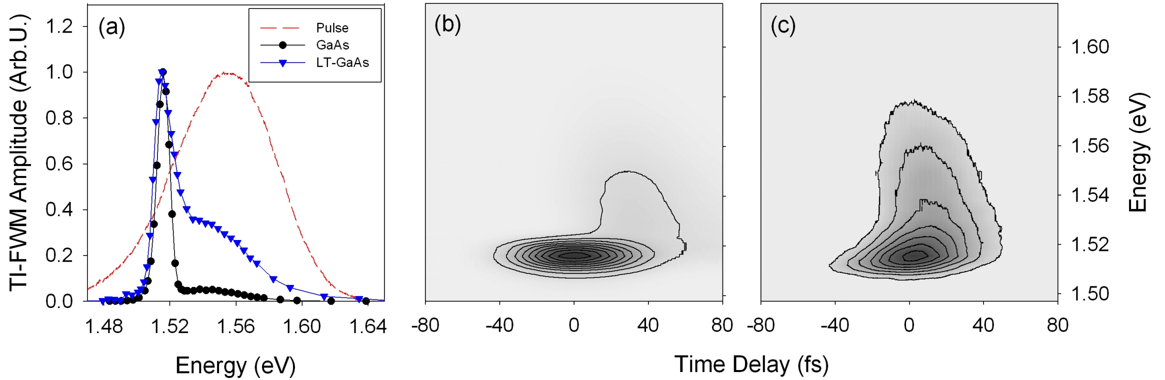

Figure 4.2: (a) The FWM spectrum at zero pulse delay for GaAs (circles) and LT-GaAs (triangles) shown together with the excitation pulse spectrum (red curve). (b) Spectrally-resolved four-wave mixing measurement on GaAs and (c) LT-GaAs.

4.2.2 Dependence of FWM results on Interpulse Delay

The SR-FWM results for collinearly $\hat{\mathrm{Y}}$ polarized pulses are shown as a function of time delay for GaAs in Fig. 4.2(b). As discussed in the preceding section, the signal consists of a sharp peak at the exciton and a weaker, spectrally-broad contribution associated with the interband continuum at higher photon energies. The dependence of the signal on pulse delay indicates that the exciton peak is only present for pulse delays in the region of overlap between the two excitation pulses (*i.e.*, around zero

delay). In contrast, the continuum response peaks at positive time delay and subsequently decays. The primary characteristic of both the exciton and continuum FWM signals in Fig. 4.2(b) have been observed in FWM experiments on GaAs under similar excitation conditions by Rappen *et al.* [35] and Lohner *et al.* [56]. The delay dependence of the SR-FWM results for LT-GaAs are shown in Fig. 4.2(c). The signal to noise ratio is lower for the data in Fig. 4.2(c) compared to Fig. 4.2(b) due to the smaller overall signal in LT-GaAs, but the primary signal characteristics are nevertheless clear. As in the case of GaAs, the peak at the exciton only persists for a narrow range of pulse delays around zero delay. The response associated with the interband continuum in LT-GaAs peaks at positive time delays, although it decays faster in LT-GaAs than in GaAs. For both GaAs and LT-GaAs, the contour plots in Fig. 4.2(b) and Fig. 4.2(c) allow the exciton and continuum responses to be more easily distinguished in comparison to an examination of the four-wave mixing spectrum at a single value of the interpulse delay. In particular, the exciton peaks at zero delay, in contrast to the continuum response, which peaks at positive delay values in both samples.

4.2.3 Comparison of Signal Characteristics for Colinear and Cross-Linear Polarization Geometries

Four-wave mixing experiments were performed for two polarization states for the two excitation pulses $\vec{E}_1$ and $\vec{E}_2$: (i) parallel linear polarizations (the $\hat{\mathrm{Y}}\hat{\mathrm{Y}}$ configuration described in Sec. 1.5.1); and (ii) perpendicular linear polarizations ($\hat{\mathrm{Y}}\hat{\mathrm{X}}$). As discussed in Sec 1.5.1, a comparison of the FWM results in these two polarization geometries provides information about the importance of EID in determining the four-wave mixing response since EID-related four-wave mixing signals are suppressed in the $\hat{\mathrm{Y}}\hat{\mathrm{X}}$ geometry [54, 41, 45, 40]. For these experiments, the linear polarization of pulse $\vec{E}_2$ was rotated using a half-wave plate while the linear polarization of $\vec{E}_1$ remained fixed. In this case, the polarization of the FWM signal will remain unchanged as it is dictated by pulse $\vec{E}_1$ due to the symmetry of the third order dielectric susceptibility tensor [40]. Changing the polarization state of pulse $\vec{E}_2$ instead of pulse $\vec{E}_1$ therefore avoids difficulties associated with polarization-dependence in the detection apparatus since the signal is always polarized in the $\hat{\mathrm{Y}}$ direction.

The SR-FWM results for GaAs in Fig. 4.2(b) are presented again in Fig. 4.3(a) together with the results in the cross-polarization geometry in Fig. 4.3(b). Fig. 4.3(c) shows a comparison of spectra at a time delay of 20 fs for the two polarization configurations. The most notable change in the FWM signal characteristics is a reduced signal contribution from the exciton in comparison to the continuum response. The overall SR-FWM signal is approximately 15 times smaller for cross-polarized excitation. (The four-wave mixing spectrum in the $\hat{\mathrm{Y}}\hat{\mathrm{X}}$ geometry in Fig. 4.3(c) has therefore been scaled by a factor of 5.08 to aid in comparison in the relative size of the exciton and continuum responses for the $\hat{\mathrm{Y}}\hat{\mathrm{Y}}$ and $\hat{\mathrm{Y}}\hat{\mathrm{X}}$ polarization geometries.) From the contour plot in Fig. 4.3(b), it is clear that the remaining exciton signal for the cross-polarized geometry is still peaked at zero delay, and persists only for the region of temporal overlap of the two excitation pulses. A reduction in the strength of the exciton signal relative to the continuum signal with the rotation of the linear polarization of one of the excitation pulses was also observed by Rappen *et al.* [35, 50] and interpreted in terms of a diminished EID signal contribution in the cross-polarization geometry, as discussed in more detail in Sec. 4.3. The smaller *overall* signal for $\hat{\mathrm{Y}}\hat{\mathrm{X}}$ excitation is also in agreement with previous experiments on GaAs [35, 41, 45].

For experiments on LT-GaAs, the SR-FWM results in the $\hat{\mathrm{Y}}\hat{\mathrm{Y}}$ and $\hat{\mathrm{Y}}\hat{\mathrm{X}}$ polarization configurations are shown in Fig. 4.4(a) and Fig. 4.4(b) respectively, together with cuts through these contour plots at -10 fs delay in Fig. 4.4(c). A delay of -10 fs was chosen for this spectral cut to reflect the earlier peak position and more rapid decay of the continuum response in LT-GaAs. The different shape of the contour lines in Fig. 4.4(a) and Fig. 4.4(b) indicates that the qualitative features of the nonlinear optical response in LT-GaAs are modified considerably by rotating the polarization state of pulse $\vec{E}_2$. In particular, the peak at zero delay associated with the exciton in Fig. 4.4(a) is absent in Fig. 4.4(b), leaving only a broad spectral feature that peaks at positive time delays for all photon energies. This suggests that the optical response of the exciton is diminished to zero in LT-GaAs for the $\hat{\mathrm{Y}}\hat{\mathrm{X}}$ polarization geometry, in contrast to GaAs where a small exciton peak remains for cross-polarized pulses. For LT-GaAs, the overall signal is reduced in the $\hat{\mathrm{Y}}\hat{\mathrm{X}}$ configuration relative to the $\hat{\mathrm{Y}}\hat{\mathrm{Y}}$ configuration, but not by as large a factor as in GaAs (approximately 5.5 times). (The spectral cut at -10 fs in Fig. 4.4(c) was scaled by a factor of 3.6 to allow

comparison of the overall difference in the spectral shape of the signal for the two polarization configurations.) The four-wave mixing spectrum in LT-GaAs for the $\hat{Y}\hat{X}$ polarization geometry is still peaked at the exciton energy, but the spectral shape has transformed into a single peak encompassing photon energies within the excited continuum transitions, in contrast to GaAs in which a distinct exciton peak remains for $\hat{Y}\hat{X}$.

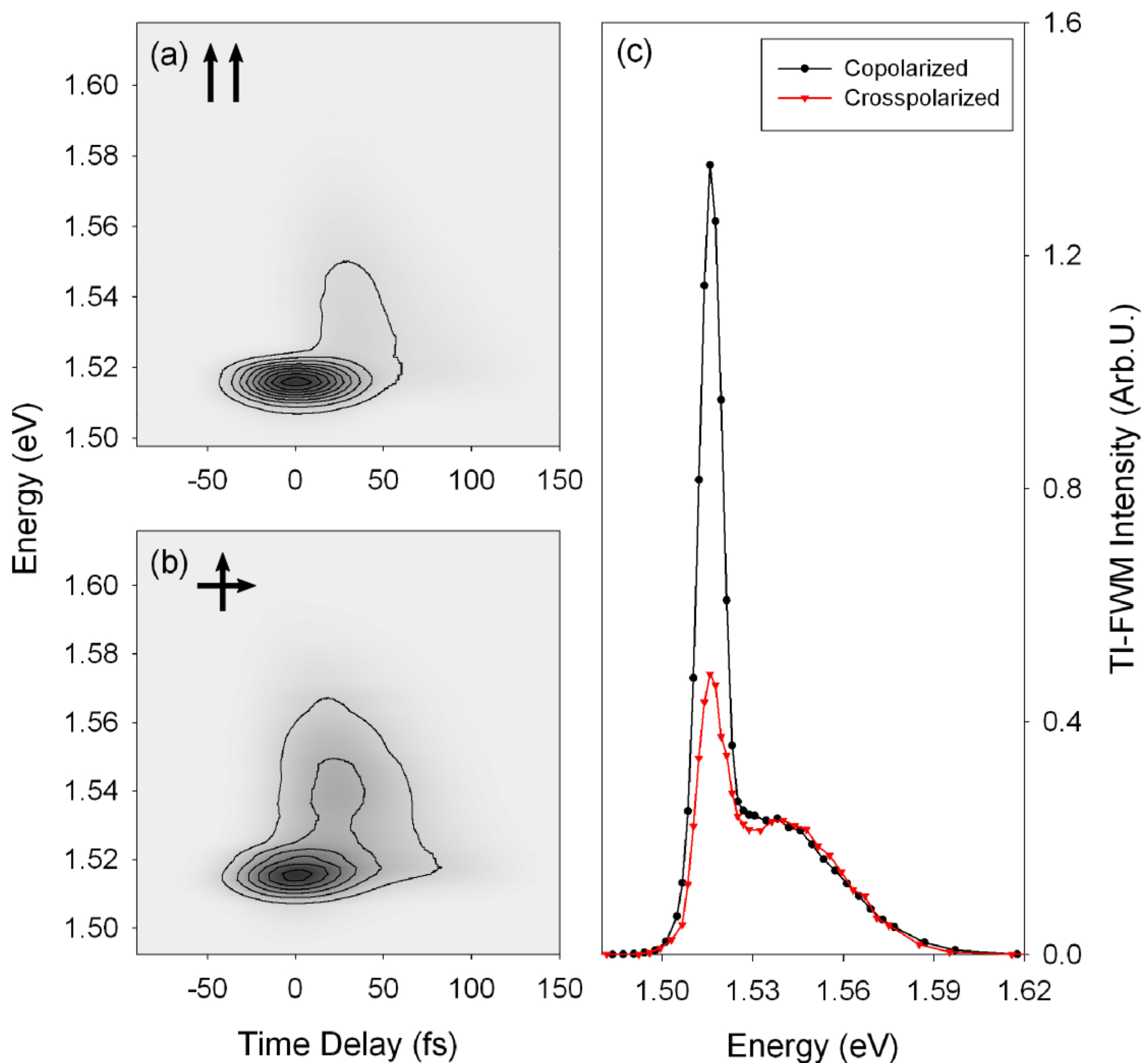

Figure 4.3: SR-FWM results for GaAs for the two polarization geometries investigated in this thesis. For (a) co-polarized pulses and (b) cross-polarized pulses. (c) An energy slice at $\tau = 20$ fs reveals the strong enhancement at the exciton resonance for the co-polarized configuration in comparison to cross-polarized case. The results of the cross-polarized case have been magnified 5.08 times for clarity.

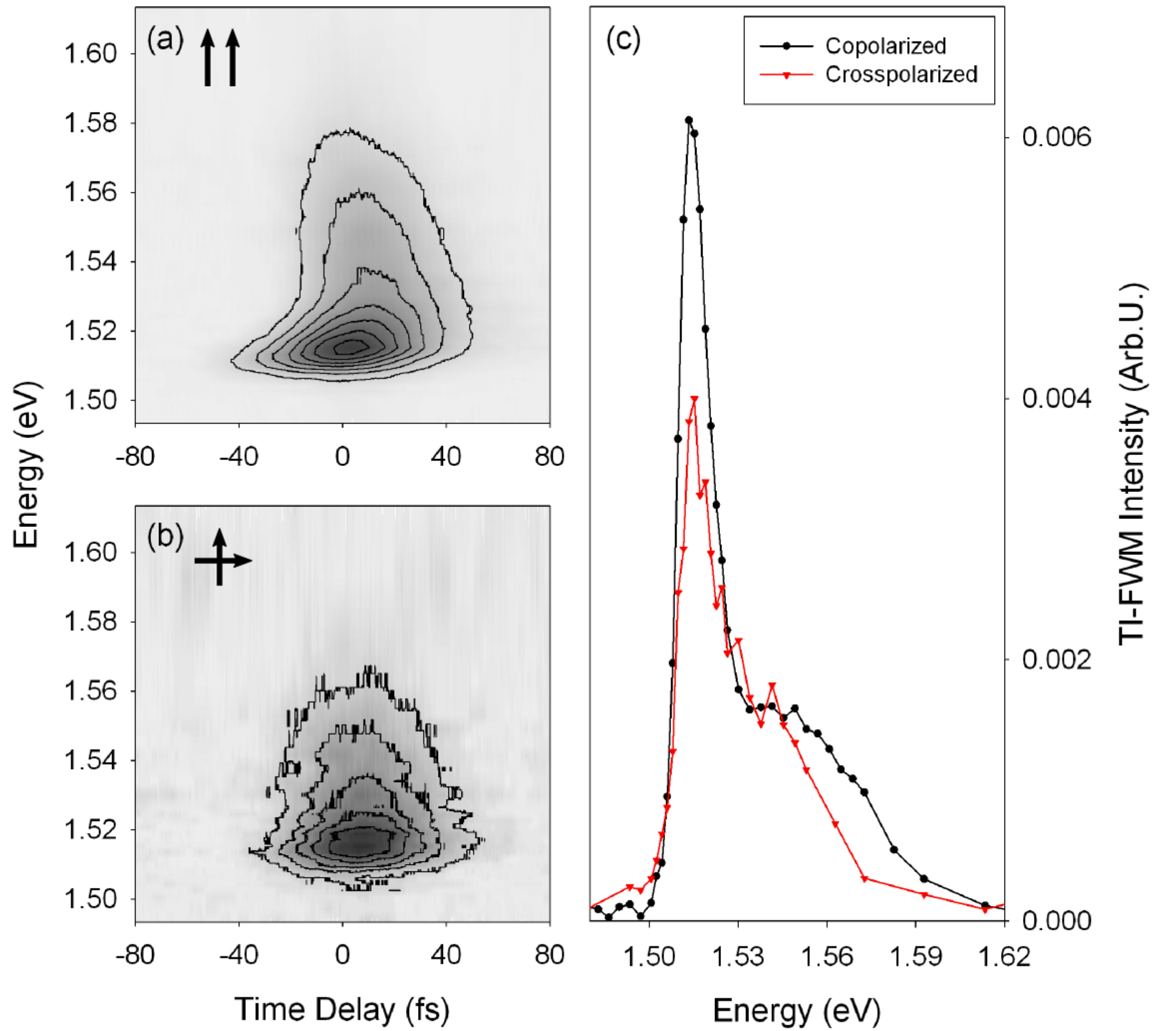

Figure 4.4: SR-FWM results for LT-GaAs for the two polarization geometries investigated in this thesis. For (a) co-polarized pulses and (b) cross-polarized pulses. (c) An energy slice at $\tau = -10$ fs . The results of the cross-polarized case have been magnified 3.57 times for clarity.

4.2.4 Influence of an Optical Prepulse on the Four-Wave Mixing Response

Experiments were also performed in the presence of an additional optical excitation pulse (a prepulse), which permits the influence of excess electron-hole pairs on the nature of the four-wave mixing response to be determined. For these experiments, a third optical delay line was utilized to control the relative delay between the prepulse ($\vec{E}_{PP}$) and the two excitation pulses used to generate the four-wave mixing signal ($\vec{E}_1$ and $\vec{E}_2$). In particular, this second delay line controls the path length of $\vec{E}_{PP}$ relative to $\vec{E}_2$, while the delay line in the path of pulse $\vec{E}_2$ is used to control the delay between pulses $\vec{E}_1$ and $\vec{E}_2$. For these experiments, all three excitation beams were polarized in the $\hat{\text{Y}}$ direction. The average power in the $\vec{E}_1$ and $\vec{E}_2$ beams are the same as for the experiments described in the preceding sections. The average power in the prepulse beam is varied, as described below.

The SR-FWM results for GaAs under excitation with a prepulse are shown in Fig. 4.5. For these experiments, the average power in the prepulse beam was 52 mW. For the results in Fig. 4.5(a), $\vec{E}_{PP}$ arrived at the sample 600 fs after pulse $\vec{E}_1$, as indicated in the diagram in the inset, while for the data in Fig. 4.5(b), the prepulse was coincident with $\vec{E}_1$. The data in Fig. 4.5(a) and Fig. 4.5(b) are shown on the same contour scale so that the quantitative changes in the signal characteristics with exposure to the prepulse may be assessed. In Fig. 4.5(a), the SR-FWM signal is indistinguishable from the results in Fig. 4.3(a), indicating that the prepulse has no effect on the four-wave mixing response when it arrives 600 fs after $\vec{E}_1$. As a result, the excess carriers injected by $\vec{E}_{PP}$ have no influence on the optical response when they are injected with a delay of 600 fs. The absence of a prepulse-related change in the signal characteristics at 600 fs delay also indicates that sample heating effects associated with the additional prepulse beam are negligible. In contrast, when the prepulse is coincident with $\vec{E}_1$ (Fig. 4.5(b)), the exciton peak is strongly reduced. Fig. 4.5(c) shows the four-wave mixing spectrum for the two cases of prepulse delay for a delay of 20 fs between $\vec{E}_1$ and $\vec{E}_2$, as in Fig. 4.3(c). The data in Fig. 4.5(c) have not been scaled for either the case of the delayed or coincident prepulse. The exciton is reduced by a factor of 3 by the prepulse, while the continuum response only drops by approximately 10%. Prepulse experiments were carried out in GaAs

quantum wells by Schultheis *et al.*[46] and Honold *et al.* [47]. In these experiments, the four-wave mixing signal was not spectrally-resolved, preventing an independent assessment of the influence of the excess carriers injected by the prepulse on the exciton and continuum signals. The results in Fig. 4.5 indicate that the primary effect of these excess carriers in GaAs is to reduce the exciton four-wave mixing signal.

The results of SR-FWM measurements in LT-GaAs for excitation by a prepulse that is delayed by 600 fs with respect to $\vec{E}_1$ is shown in Fig. 4.6(a) and for coincident $\vec{E}_{PP}$ and $\vec{E}_1$ in Fig. 4.6(b). The four-wave mixing spectra corresponding to these contour plots for a delay of -10 fs between $\vec{E}_1$ and $\vec{E}_2$ is shown in Fig. 4.6(c). The data are shown on the same scale for both the contour plots in Fig. 4.6(a) and Fig. 4.6(b) as well as the spectra in Fig. 4.6(c). In Fig. 4.6(c), the continuum signal is slightly larger relative to the exciton when compared with the results without a prepulse (Fig. 4.4(c)), but the overall signal characteristics are similar in the two cases, indicating that carriers injected 600 fs after $\vec{E}_1$ do not modify the nonlinear response substantially. In contrast, when the prepulse is coincident with $\vec{E}_1$ (Fig. 4.6(b)), the excess carriers injected by the prepulse transform the SR-FWM response in a dramatic way: The exciton response peaked at zero delay in Fig. 4.6(a) is completely absent in Fig. 4.6(b). In addition, for coincident $\vec{E}_{PP}$ and $\vec{E}_1$, the optical response for photon energies within the interband continuum is *larger* in the presence of these excess carriers than for excitation 600 fs after $\vec{E}_1$. The overall signal characteristics in LT-GaAs for coincident prepulse excitation in Fig. 4.6(a) are qualitatively similar to the results for cross linear polarized excitation in Fig. 4.4(b), consisting of a signal peaked at positive delay encompassing photon energies within the excited continuum transitions.

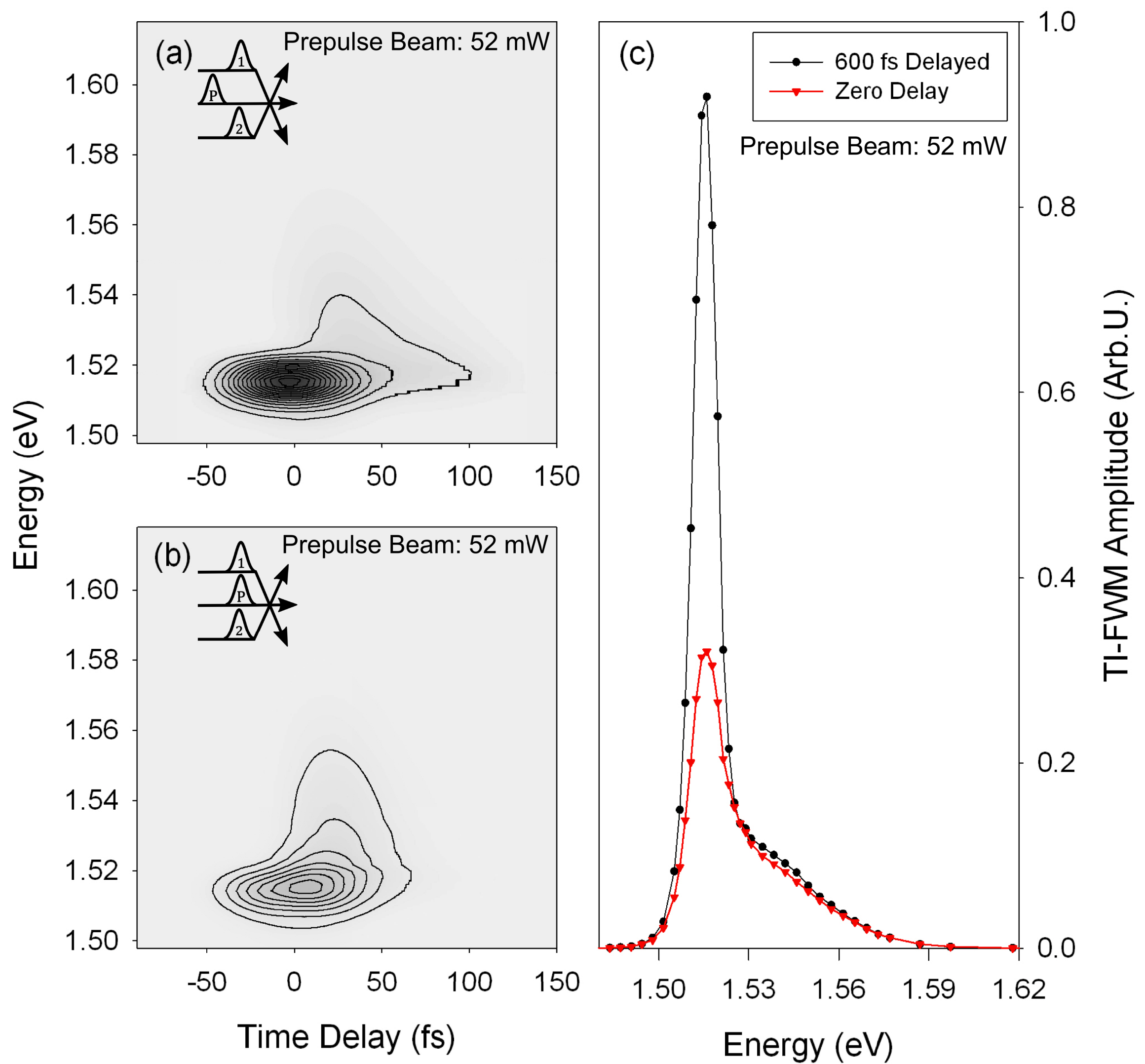

Figure 4.5: SR-FWM results for GaAs for two prepulse conditions investigated in this thesis. For a (a) prepulse delayed 600 fs and (b) at zero delay with respect to mutual zero delay. (c) An energy slice at $\tau = 20$fs is shown to highlight the change in TI-FWM signal at the excitonic resonance.

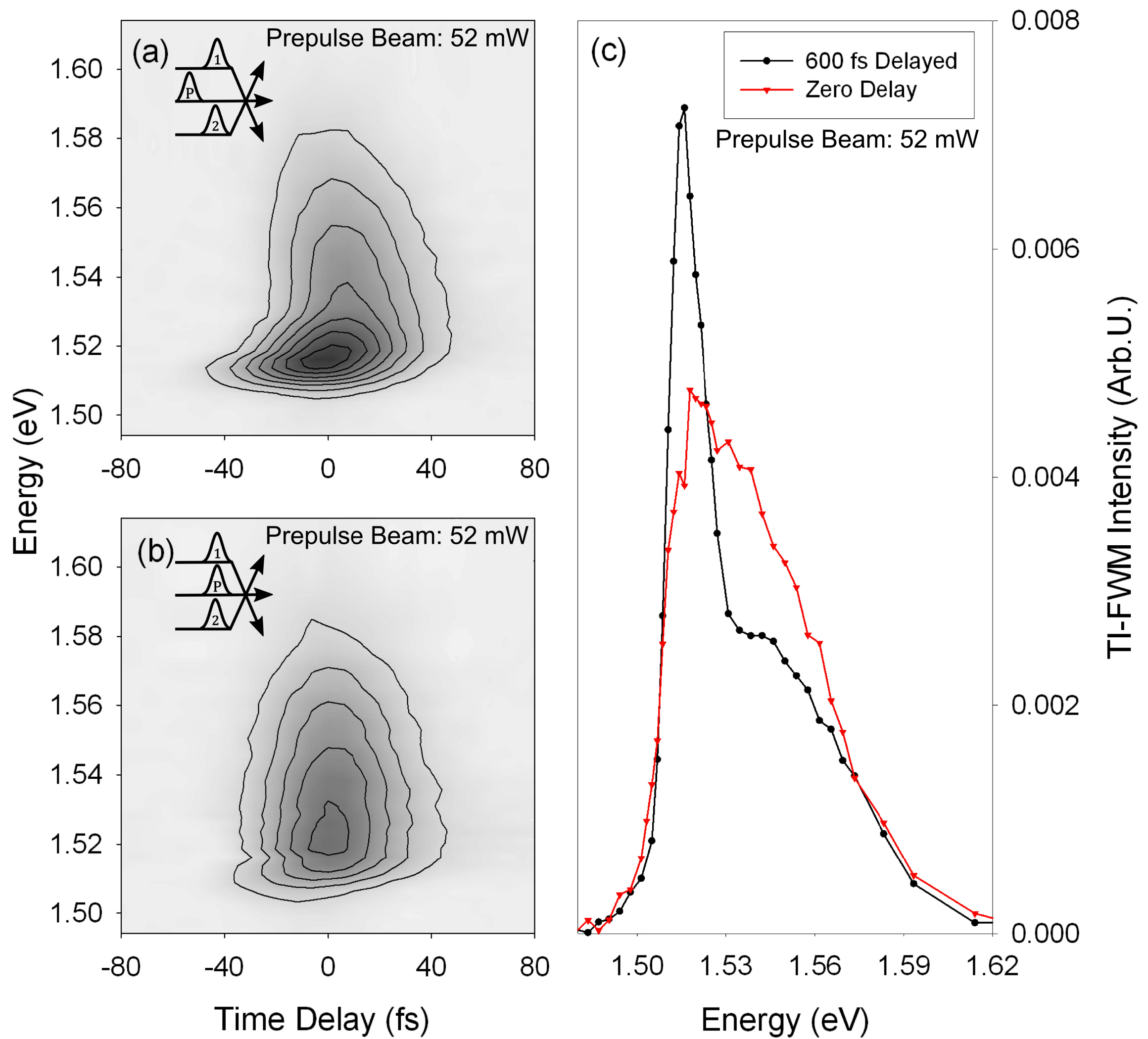

Figure 4.6: SR-FWM results for LT-GaAs for two prepulse conditions investigated in this thesis. For a (a) prepulse delayed 600 fs and (b) at zero delay with respect to mutual zero delay. (c) An energy slice at $\tau = -10$fs highlights the dramatic change in the TI-FWM line shape with the addition of the prepulse.

4.2.5 Variation of Exciton and Continuum Response with Prepulse Excitation Conditions

In order to further elucidate the influence of the prepulse on the four-wave mixing signal in GaAs and LT-GaAs, experiments were performed as a function of the power in the prepulse beam and the time delay between $\vec{E}_{PP}$ and $\vec{E}_1$. For these experiments, the signal was detected at the centre of the exciton peak (1.515 eV) or at a transition energy within the interband continuum (1.553 eV). The dependence of the exciton response in GaAs on the power in the prepulse beam is shown in Fig. 4.7(a). The strength of the TI-FWM signal monotonically decays as a function of increasing prepulse power for the full range of powers (0 - 52 mW) used in the experiments. The peak signal versus delay between $\vec{E}_1$ and $\vec{E}_2$ at each prepulse power is shown in Fig. 4.7(c), also indicating a monotonic decay with increasing prepulse power. Each data point has been averaged over a 2 fs interval, centred at the delay corresponding to the peak signal. The TI-FWM signal as a function of the delay between $\vec{E}_1$ and $\vec{E}_2$ versus prepulse power for the continuum is shown in Fig. 4.7(b) and the corresponding peak continuum response is shown versus prepulse power in Fig. 4.7(d). The strength of the continuum response exhibits a much smaller decay with increasing prepulse power than the exciton, and the trend is approximately linear within the signal to noise. The decay of the four-wave mixing signal at both the exciton and the continuum energies is consistent with the results in Fig. 4.5, showing the influence of the prepulse on the full four-wave mixing spectrum.

The prepulse power results for LT-GaAs at the exciton are shown in Fig. 4.8(a) and Fig. 4.8(c). The magnitude of the four-wave mixing signal at the exciton decays with increasing prepulse power in Fig. 4.8(c), as in the results for GaAs in Fig. 4.7(c), however the total decay range is smaller (about 30% in LT-GaAs compared to 70% in GaAs). The dependence of the continuum response at 1.533 eV on prepulse power in LT-GaAs is shown in Fig. 4.8(b) and Fig. 4.8(d). In contrast with the results in Fig. 4.7(d) for GaAs, in Fig. 4.8(d), an enhancement in the continuum response with increasing prepulse power is observed in LT-GaAs. The signal at 1.515 eV is characterized by a large continuum signal component. This is apparent from the observation of a temporal shift in the peak of the signal to larger time delays with increasing prepulse power (Fig. 4.8(a)).

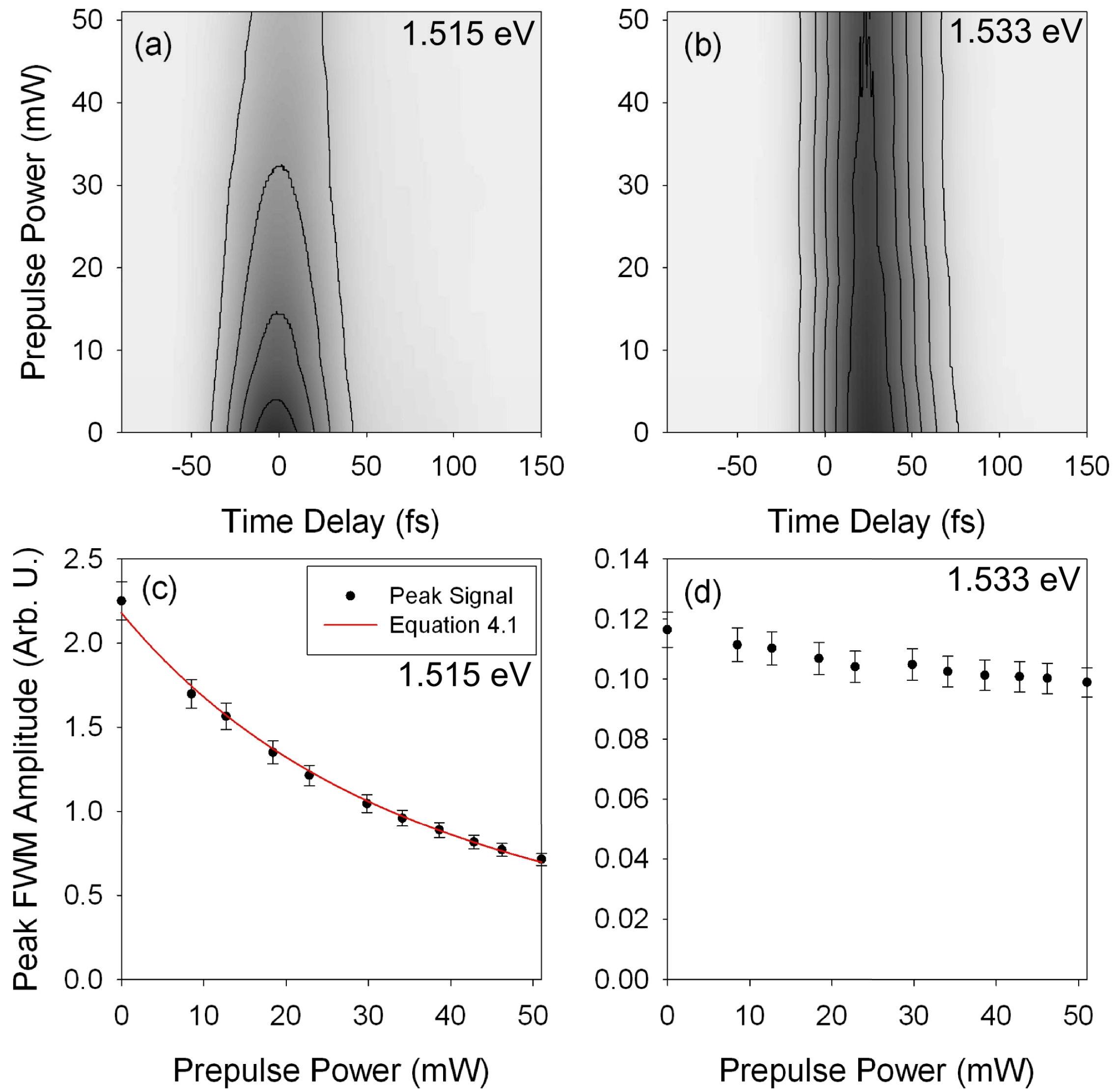

Figure 4.7: Results for GaAs for varying prepulse power. For a range of prepulse powers, the FWM emission as a function of pulse delay was collected at two energies probed in this thesis work. The TI-FWM contour as a function of prepulse power is depicted in (a) for the exciton, and (b) for the continuum. The peak value versus pulse delay corresponds to the data in (a) and (b) and is plotted in (c) and (d) respectively.

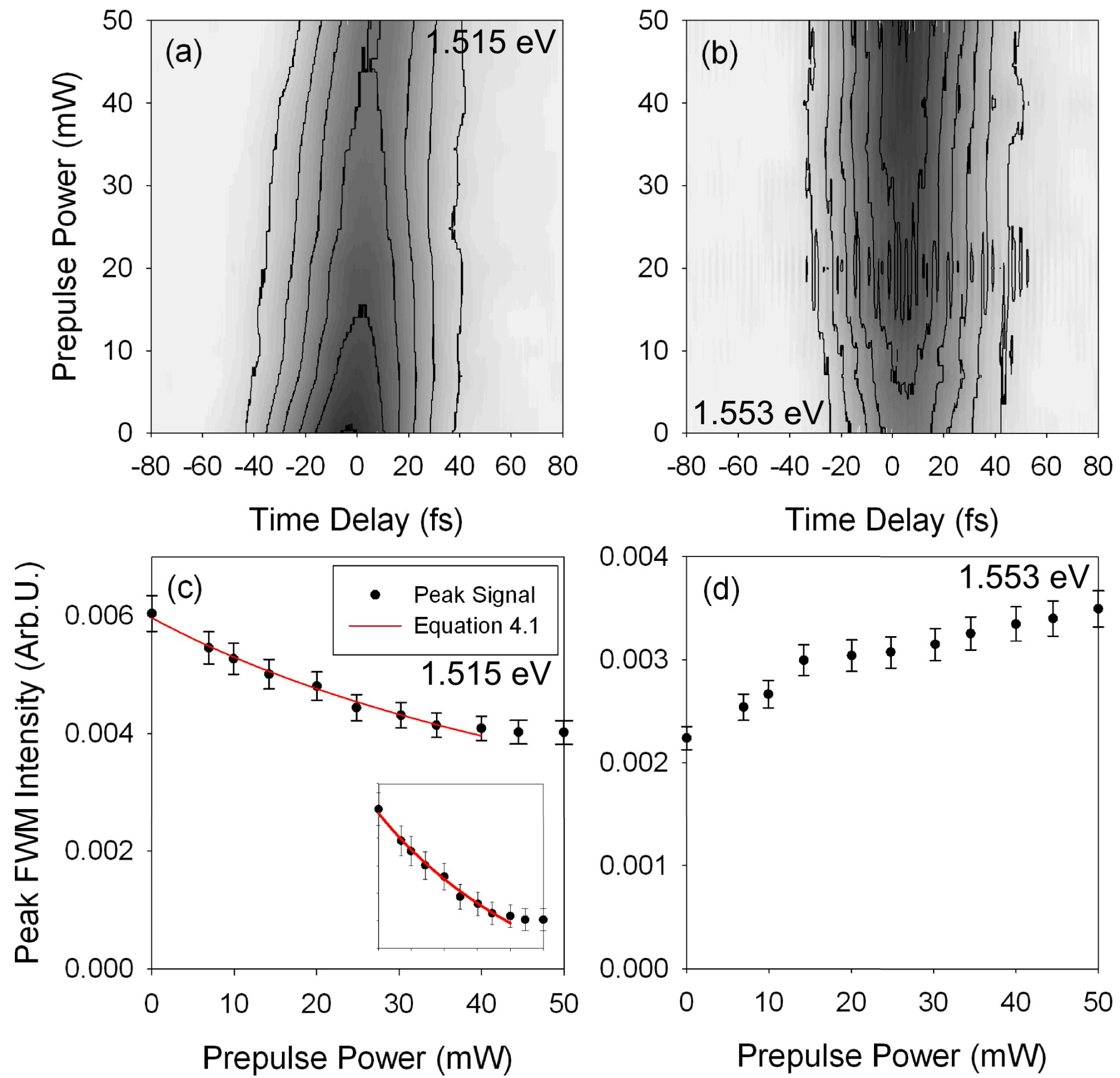

Figure 4.8: Results for LT-GaAs for varying prepulse power. For a range of prepulse powers, FWM emission as a function of pulse delay was collected at two energies probed in this thesis work. The TI-FWM contour as a function of prepulse power is depicted in (a) for the exciton, and (b) for the continuum. The peak value as a function of prepulse power for both of these contours are plotted in c) and d) respectively.

The prepulse delay dependence of the four-wave mixing response in GaAs is shown in Fig. 4.9(a) and (c) for the exciton (1.515 eV) and in Fig. 4.9(b) and (d) for the continuum (1.533 eV). As in the case of the power-dependent experiments described above, for each data point in Fig. 4.9(c) and (d), the signal amplitude was averaged over a 2 fs interval centred at the delay corresponding to the peak of the signal. The grey bars in Fig. 4.9 indicate the region of temporal overlap between $\vec{E}_1$ and $\vec{E}_{PP}$. The cross correlation between these pulses is also shown as the solid black curve. The signal at the exciton in GaAs is most strongly diminished within the region of pulse overlap. When the prepulse arrives before $\vec{E}_1$ (*i.e.*, for negative prepulse delay), the exciton signal strength is independent of prepulse delay. For positive prepulse delay (*i.e.*, when the prepulse arrives after $\vec{E}_1$), the signal increases with increasing prepulse delay, saturating at 600 fs. When the prepulse is incident 600 fs after $\vec{E}_1$, it has no impact on the four-wave mixing signal, as discussed in the preceding section. In contrast to the exciton response in Fig. 4.9(c), the continuum four-wave mixing signal is only weakly dependent on prepulse delay, reflecting the small influence of the prepulse on the continuum signal in Fig. 4.5(a). Within the signal to noise ratio, the small decrease in the continuum signal associated with the prepulse appears to occur abruptly at zero prepulse delay, and with relatively constant signal strength within the positive and negative regions away from zero delay.

The dependence of the four-wave mixing response in LT-GaAs on prepulse delay differs significantly from that in GaAs, as shown in Fig. 4.10. The prepulse delay dependence at the exciton is shown in Fig. 4.10(a) and Fig. 4.10(c). As in the case of GaAs, the exciton is most strongly suppressed in the region of zero prepulse delay; however, the exciton is unaffected by the prepulse for delays outside the region of pulse overlap. This is in contrast to the situation in GaAs, where the exciton four-wave mixing signal was reduced for the full range of negative prepulse delays. For the continuum response, shown in Fig. 4.10(b) and Fig. 4.10(d), the four-wave mixing signal is enhanced by the prepulse, as discussed in the preceding section. From Fig. 4.10(d), we see that it is enhanced only in the region of pulse overlap. Within the signal to noise ratio, the continuum response is not affected significantly for positive or negative prepulse delays, in contrast to the situation in GaAs in Fig. 4.9(d), where the slight decrease in the continuum response persists for the full range of negative

prepulse delays investigated.

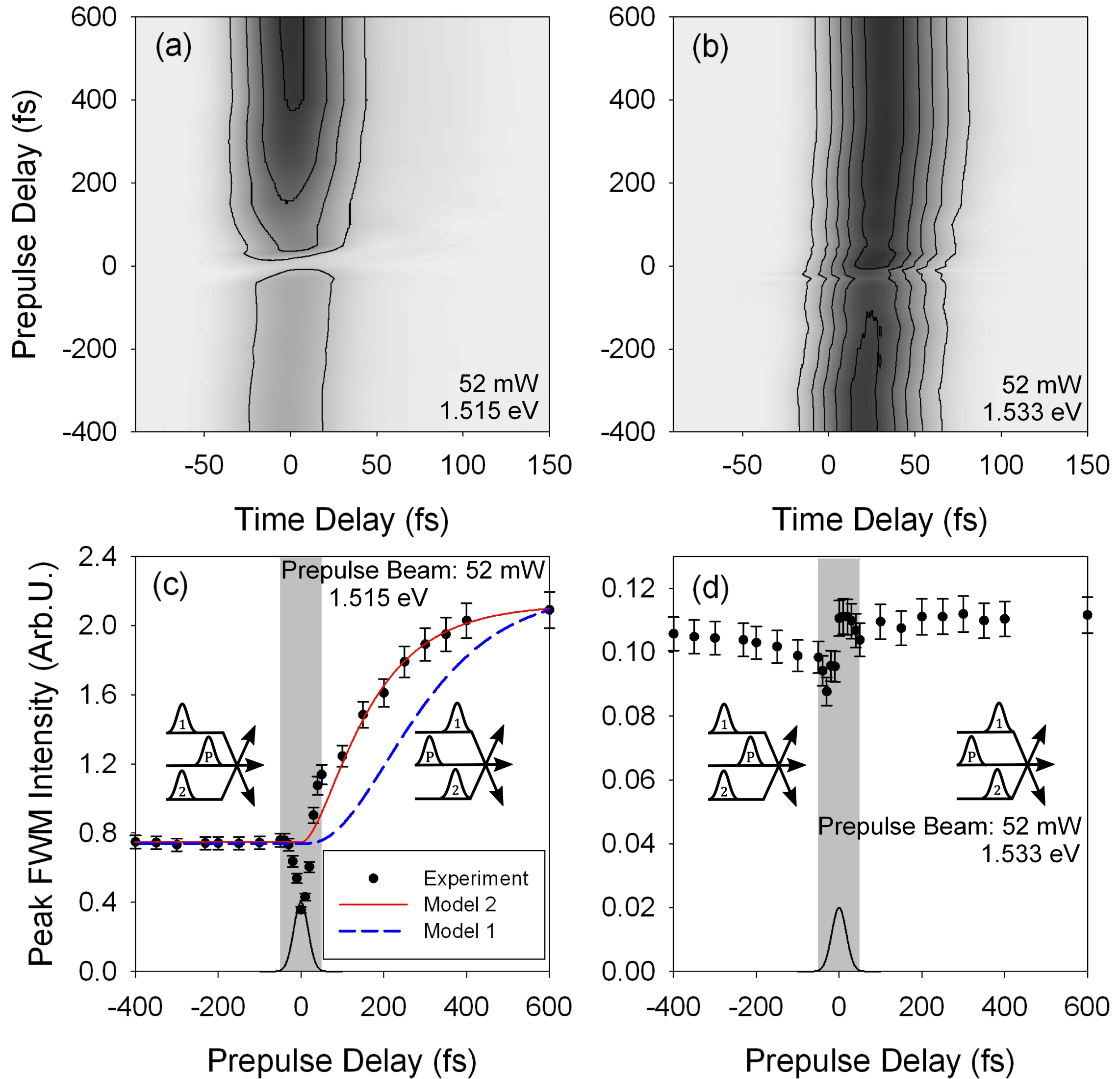

Figure 4.9: Results for GaAs for varying prepulse delay with respect to mutual zero delay. For a range of prepulse delays, FWM emission as a function of pulse delay was collected at the two energies probed in this thesis work. The TI-FWM contour as a function of prepulse delay is plotted in (a) for the exciton, and (b) for the continuum. The peak value as a function of prepulse delay for both of these contours are plotted in (c) and (d) respectively. The solid black line is the autocorrelation of $\vec{E}_1$ and $\vec{E}_2$, and the gray shaded area is the region of pulse overlap. The solid red and dashed blue lines represent fits to two models of the FWM response considered in this thesis work.

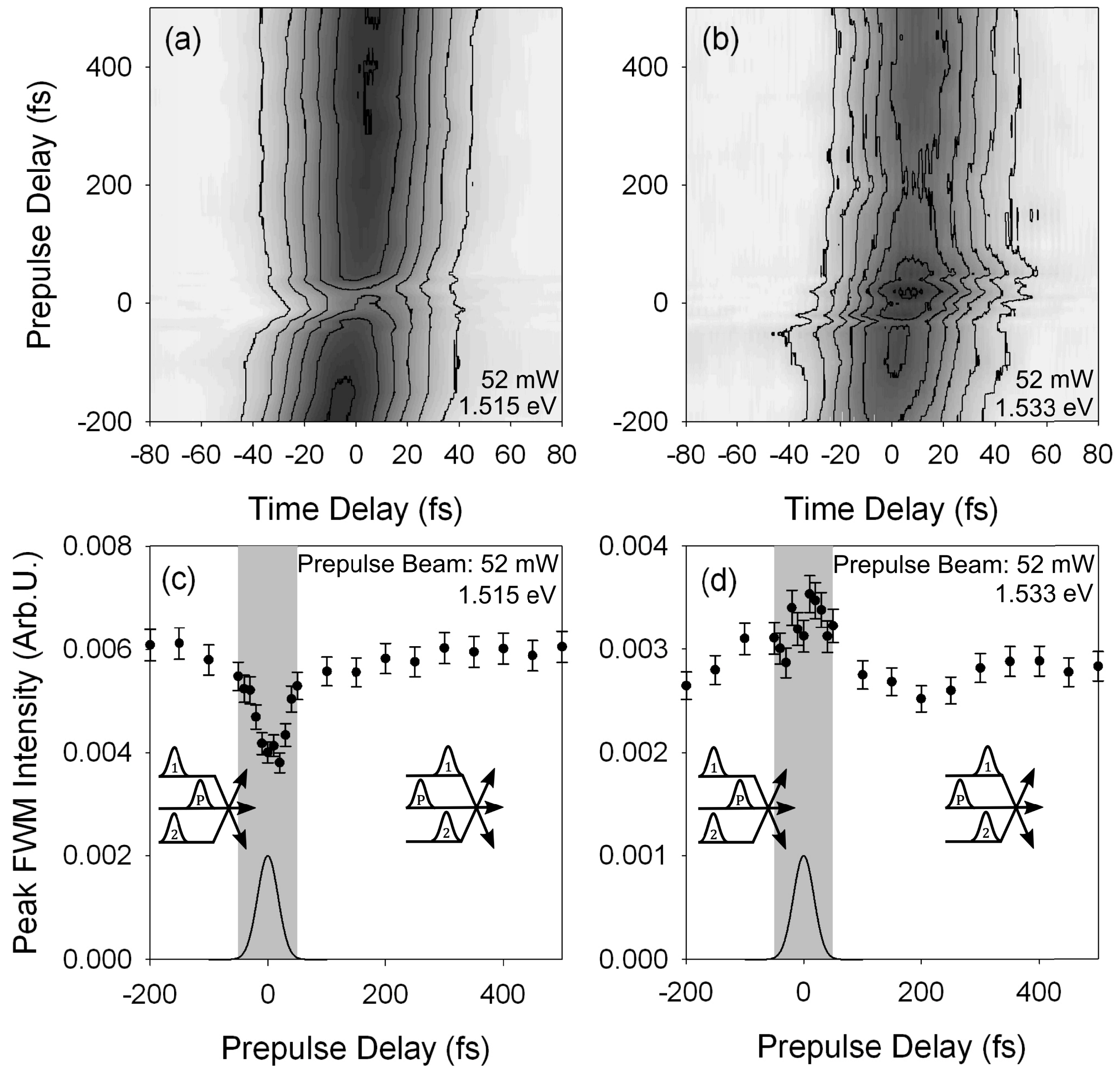

Figure 4.10: Results for LT-GaAs for varying prepulse delay with respect to mutual zero delay. For a range of prepulse delays, FWM emission as a function of pulse delay was collected at the two energies probed in this thesis work. The TI-FWM contour as a function of prepulse delay is plotted in (a) for the exciton, and (b) for the continuum. The peak value as a function of prepulse delay for both of these contours are plotted in (c) and (d) respectively. The solid black line is the autocorrelation of $\vec{E_1}$ and $\vec{E_2}$, and the gray shaded area is the region of pulse overlap.

4.3 Discussion

4.3.1 Observation of the Exciton in LT-GaAs

The discrete response observed in LT-GaAs in the experiments described in the preceding section has been identified as the fundamental exciton because this feature appears at the exciton energy in GaAs. The observation of the exciton is surprising because the linear absorption spectrum shows no evidence of an exciton, even at low temperature. There have been a variety of speculations as to why the exciton is absent in linear spectroscopy [14]. For example, the large density of defects in LT-GaAs is expected to modify the description of elementary excitations since carriers in the material will exhibit a varying degree of localization due to binding to defects and defect complexes. Bound excitons would exhibit varying transition energies as a result of the differing environments for excitons in different positions in the material, resulting in a smearing out of the exciton resonance. There are built-in electric fields inside the material associated with defects that would shift the transition energy by a varying extent. The lifetime of free electrons in LT-GaAs has been shown to be very short (∼1 ps), attributed to fast trapping to the As_{Ga} impurity band [14]. This short lifetime would broaden the exciton resonance. There is also a strong linear absorption associated with transitions between the As_{Ga} impurity band and the conduction band. Such transitions have an energetic onset near the middle of the band gap and increase in density with increasing photon energy due to the increasing density of states in the conduction band. Carriers within the As_{Ga} mid-gap impurity band may contribute to screening of the attractive Coulomb interaction responsible for formation of the exciton. The effectiveness of these trapped electrons for screening (in particular in comparison to the influence of delocalized electrons and holes in band states) is not known. Nevertheless, only an explanation based on screening can account for the *complete* lack of any feature in the absorption tied to the exciton, suggesting that the electron-hole Coulomb interaction may be neglected in models of the optical response of LT-GaAs. This thesis work illustrates that these Coulomb effects cannot, in fact, be neglected since the exciton is visible in the nonlinear optical response. This finding has important implications for the description of ultrafast optical switches and detectors fabricated from LT-GaAs, since for such devices, absorption is well-within

the nonlinear regime. This result is also of value in the interpretation of past ultrafast pump probe measurements of carrier recovery and recombination times in this system [1, 14].

4.3.2 Excitation-Induced Dephasing Dominates Exciton Signal in LT-GaAs

The characteristic feature of the exciton response in both GaAs and LT-GaAs is that it is pulse-width limited versus the delay between $\vec{E}_1$ and $\vec{E}_2$ despite being spectrally narrow in energy. These observations cannot be accounted for using a simple description based on free polarization decay since, in that case, the rate of decay versus pulse delay and the spectral linewidth are inversely related, both being determined by the dephasing rate. As described in Sec. 1.5.2, the emergence of an understanding of the optical response at the exciton for conditions in which both excitons and continuum transitions are simultaneously excited took a number of experiments over a span of several years, together with a variety of theoretical models describing many-body effects to varying degrees of complexity. The correct description ultimately emerged [54] in terms of excitation-induced dephasing, by which the dephasing rate of the exciton is linearly dependent on the total density of excited electron-hole pairs. Such a feature is pulse width limited versus delay due to destructive interference between contributions to the signal arising from scattering with carriers in the continuum with different energies. Due to this interference, an EID signal is only significant for transition energies at which there exists a rapid change in the optical joint density of states, such as at an exciton. EID therefore does not contribute for energies within the interband continuum above the band gap. As a result, the response of the continuum is characteristic of a simple photon-echo since it represents a two-level system with a continuous range of transition energies. As shown by Yajima and Taira *et al.*[33], for such a photon-echo response, the four-wave mixing signal peaks at positive time delay and decays at a rate determined by the dephasing time of carriers in the continuum. These predictions account well for the optical response of the continuum transitions observed in this thesis in both GaAs and LT-GaAs. The observation of a pulse width-limited response at the exciton in LT-GaAs indicates that, as in GaAs, the nonlinear response at the exciton is mediated by EID.

As discussed in Sec 1.5.1, the EID contribution to the four-wave mixing signal at the exciton is a very sensitive function of the relative orientation of the polarization states of the excitation beams. The polarization-dependent experiments carried out in this thesis work have therefore allowed the effects of EID on the nonlinear optical response of the exciton in LT-GaAs to be further investigated. The strong EID-related signal contribution at the exciton in experiments with in the $\hat{\mathrm{Y}}\hat{\mathrm{Y}}$ polarization configuration are predicted to vanish when cross linearly-polarized excitation (the $\hat{\mathrm{Y}}\hat{\mathrm{X}}$ geometry) is used [40], in agreement with past experiments in GaAs [41, 45] as well as the experiments on GaAs in this thesis work. The exciton response is not reduced to zero for cross-linear polarization in GaAs, as seen in Fig. 4.3(c). Since the residual exciton response retains the pulse-width limited character, it is still consistent with an EID response. This residual signal may be due to imperfections in the polarization states of the laser beams due to the limited accuracy of retardation in the wave plate used in these experiments. (Using a Wallaston prism, the estimated $\hat{\mathrm{X}} : \hat{\mathrm{Y}}$ polarization ratio for $\vec{E_2}$ is 15:1.) In LT-GaAs, the exciton is also reduced in the cross linear polarization configuration, as seen in Fig. 4.4. This is consistent with the identification of EID as the source of the four-wave mixing signal at the exciton in LT-GaAs. As discussed in the preceding section, the exciton in LT-GaAs is diminished more strongly for cross linear polarization than in GaAs. This is likely due to the smaller size of the EID signal in LT-GaAs tied to a shorter dephasing time, as discussed in the next section.

4.3.3 Dephasing Dynamics in LT-GaAs

The exciton peak is smaller in magnitude relative to the continuum response in LT-GaAs than in GaAs. In a time-integrated four-wave mixing experiment, the total amplitude of the signal provides one measure of the dephasing time within the material under study because the longer the dephasing time the longer in time the four-wave mixing signal persists. As a result, a larger dephasing time corresponds to a larger total (time-averaged) power in the four-wave mixing signal beam. The lower exciton response in LT-GaAs compared to GaAs can therefore be traced back to a shorter dephasing time. This is consistent with the broader width of the exciton peak versus photon energy in LT-GaAs than in GaAs. The continuum peak also decays faster

versus time delay in LT-GaAs than in GaAs. The dephasing process in the continuum states was studied by Yildirim *et al.* in LT-GaAs and LT-GaMnAs [17] and has been attributed to carrier-carrier scattering. In particular, the rate of scattering is larger in LT-GaAs than in GaAs because the total optically-excited carrier density is larger for a given average power for LT-GaAs due to the large strength of absorption below the band gap. Possible origins of the larger dephasing rate for excitons in LT-GaAs are described below. The smaller overall signal in LT-GaAs compared to GaAs is due in part to the higher rate of dephasing in LT-GaAs. Additionally, inhomogeneities in the thin film caused by defects represents a source of scattering of the incident light for LT-GaAs, and the presence of defects redistributes the optical joint density states, increasing the density of transitions tied to defects at the expense of the interband transitions. Both of these effects contribute to a reduced four-wave mixing signal in LT-GaAs compared to GaAs.

Since the EID-mediated signal at the exciton is pulse width limited versus the time delay between $\vec{E}_1$ and $\vec{E}_2$, the delay dependence carries no useful information about the dephasing time of the exciton, as discussed above. Instead, the dephasing rate of the exciton may be determined from the measured linewidth of the four-wave mixing peak. The EID signal has a spectral line shape described by a squared Lorentzian [54]. In order to extract T_2, the four-wave mixing spectrum for co-polarized excitation at the exciton zero delay was fit to a squared Lorentzian for both GaAs and LT-GaAs, while for the purpose of extracting T_2 for the exciton, the continuum response was modeled by a Gaussian peak with a full-width half-maximum equal to the pulse bandwidth (74 meV) multiplied by a Heaviside step function at 1.519 eV and 1.510 eV to reflect the band gap in GaAs and LT-GaAs respectively. The lower band gap energy in LT-GaAs in comparison to GaAs can be explained by the four-wave mixing response from bandtail states. These fits are shown in Fig. 4.11 and yielded dephasing times of 250 fs and 135 fs for GaAs and LT-GaAs, respectively. The shorter T_2 time obtained in LT-GaAs could be attributed to additional dephasing brought on by two different scattering mechanisms: (i) carrier-carrier scattering, reflecting the larger total electron-hole pair density excited in LT-GaAs for the same average power; and (ii) scattering of the exciton with As-related defects. In experiments by Yildirim *et al.*, carrier-carrier scattering was found to strongly dominate the dephasing process

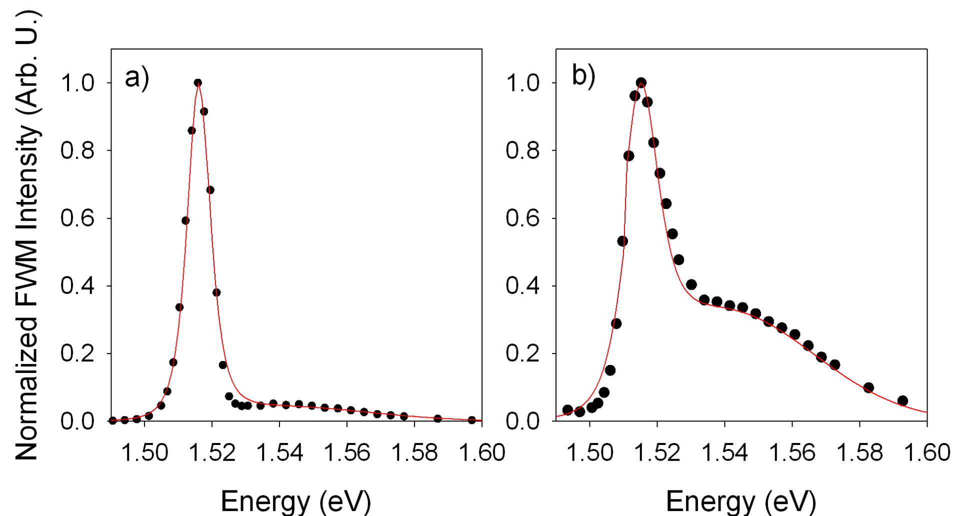

Figure 4.11: (a) TI-FWM signal slice at zero delay for GaAs. (b) TI-FWM signal slice at zero delay for LT-GaAs. The red line is a fit using a Gaussian and a squared Lorentzian.

for continuum transitions; however, the exciton dephasing process could still be influenced by defects since exciton-carrier and exciton-exciton scattering processes are much weaker than carrier-carrier scattering [17]. In order to determine which of these two processes dominates dephasing at the exciton, one could carry out SR-FWM experiments in GaAs and LT-GaAs for conditions of equal excited carrier density. In this case, a greater rate of dephasing for LT-GaAs would signal the dominant influence of defects. Such an experiment is not feasible, however, because the signal to noise ratio in LT-GaAs does not permit a low enough carrier density to be used in experiments on LT-GaAs and higher average powers have been found in experiments on GaAs to lead to significant sample heating (observed via a shift in the exciton transition energy from the known value). Alternatively, one may perform measurements of the spectral linewidth of the exciton signal as a function of prepulse power. In such a case, a linear dependence of T_2 with power would indicate the dominant role of exciton-carrier scattering. Such experiments would be a useful extension to the present work.

4.3.4 Prepulse Power Dependence

In order to understand the dependence of the four-wave mixing results in both GaAs and LT-GaAs on the power in the prepulse beam, we must take into account the influence of an excess distribution of electron-hole pairs on the four-wave mixing signal. There are two primary physical effects to consider: (i) the extra carriers modify the total dephasing rate; and (ii) these carriers may contribute to screening of the Coulomb interaction within the system. Neglecting the prepulse carriers for the moment, and considering only the exciton response for the conditions of our experiment, the time-integrated signal (found by integrating the norm square of Eqn. 2.32 over time after multiplying by μ_x, as carried out in [57]) is given by:

$$\mathrm{S_{TI}}(\tau) \propto \frac{(1/4)(\Gamma N^{(-2)})^2(\varepsilon_2^2\mu_x^2)/\hbar^2}{(\gamma_0 + \Gamma N^{(0)})^3} \tag{4.1}$$

which is a function of pulse delay via a factor $\delta(\tau)$ in $N^{(-2)}$. The denominator contains the total dephasing rate to the power 3, indicating that a larger carrier density will decrease the signal at the exciton. The signal also contains the EID coefficient (Γ), in both the numerator and denominator. It is also proportional to the dipole moment of the exciton to the 4$^{\text{th}}$ power($N^{(-2)}$ contains μ_k^4 as well.) Prepulse injected carrier will reduce γ_0 in the above formula, reducing the total signal via a reduction in the dephasing time. Screening will also reduce (in principle) Γ and/or μ_x, since each of these parameters is tied to the Coulomb interaction (μ_x is the dipole moment of the exciton). Evidence for screening of the EID coefficient has been seen in InP [57] and GaAs [41]. In those experiments, the carrier densities were $\sim 5 \times 10^{16}$ cm^{-3} in Allan *et al.* [57] and $\sim 5 \times 10^{15}$ cm^{-3} in Wang *et al.* [41]. Using the power transmitted through the samples, the injected carrier densities in our experiments are 5×10^{15} cm^{-3} (2×10^{16} cm^{-3}) in HT-GaAs (LT-GaAs) due to $\vec{E}_1$ and $\vec{E}_2$, and a similar density of additional carriers due to the prepulse. These densities are comparable to those used in these earlier experiments, and so some degree of screening of the EID coefficient is expected. Screening of the dipole moment of the exciton should occur when the intercarrier separation is comparable to the exciton Bohr radius [57], which is 9.5 nm in GaAs [47]. For our extracted densities, the intercarrier separation is 59 nm (35 nm) in HT-GaAs (LT-GaAs). Since these values exceed the exciton Bohr radius by a considerable amount, it is likely that screening of the EID coefficient is

more important than screening of the exciton dipole moment for the conditions of our experiment. In any event, it is clear that both screening of the EID coefficient and the increase in dephasing rate caused by the prepulse carriers should decrease the optical response at the exciton in both HT-GaAs and LT-GaAs in agreement with the results in Fig. 4.5 and Fig. 4.6. Fits to the signal at the exciton using Eqn. 4.1 for both GaAs and LT-GaAs were carried out neglecting the influence of screening of the EID coefficient. These fits appear as the solid curves in Fig. 4.7(c) and Fig. 4.7(c). The good agreement suggests that the dephasing time dependence on prepulse power may dominate over that tied to screening, however a nonzero influence of screening cannot be ruled out given the available information. The nonzero residual exciton in HT-GaAs in Fig. 4.5 compared to 4.6 is likely due to the larger dephasing time in HT-GaAs, as discussed in Sec. 4.3.3. This also accounts for the monotonic decay in the magnitude of the exciton response in both HT-GaAs and LT-GaAs with increasing prepulse power. The small shift to positive delay of the four-wave mixing response of the exciton energy in LT-GaAs with increasing prepulse power (Fig. 4.8) is due to the larger importance of the continuum response in LT-GaAs in comparison to the exciton: As the exciton response is diminished, the continuum signal begins to dominate, which peaks at positive time delay. This also explains why a fit to Eqn. 4.1 was only possible for powers below 40 mW since the exciton contribution to the total signal becomes negligible above 40 mW.

The influence of the prepulse on the magnitude of the continuum response differs qualitatively in LT-GaAs and HT-GaAs. As discussed in the preceding section, the continuum response in HT-GaAs is reduced in the presence of the prepulse, although by a small amount ($\sim$ 10%) whereas in LT-GaAs it is enhanced. The decrease in HT-GaAs could be explained by screening of the Sommerfeld enhancement of the band edge, but the opposite trend in LT-GaAs is more difficult to account for. In experiments at the exciton tied to the spin-orbit split-off valence band, screening was also found to enhance the continuum response for energies above the exciton [36]. This was explained in terms of destructive interference of the EID emission at the exciton with the continuum photon-echo, an explanation that was supported by corresponding theoretical calculations. A similar interference effect may be occurring in LT-GaAs,

causing the continuum signal to recover once the exciton signal is removed. In HT-GaAs, the larger dephasing time prevents the exciton from being fully eliminated through screening. In this case, the reduction in destructive interference competes with screening of the Sommerfeld effect, with the latter process (weakly) dominating in HT-GaAs.

4.3.5 Prepulse Delay Dependence

In order to understand the dependence of the four-wave mixing signal on the time delay of the prepulse, one also must take into account the effects of the prepulse-injected carrier distribution on the EID coefficient (due to screening) and the total dephasing rate. In order to model these two processes, Eqn. 4.1 was modified such that, at the time of arrival of the prepulse, both the dephasing rate and the magnitude of the EID coefficient are abruptly reduced. In the model, the relative importance of these two processes can be independently controlled. The resulting modified polarization was used to evaluate the time-integrated signal strength as a function of prepulse delay. The result of a fit to this model for the signal in GaAs is shown in Fig. 4.9(c) by the blue dashed curve (labeled Model 1). For this fit, the dephasing times were taken such that $\gamma_0 = 1/200$fs and $\gamma = 1/189$fs and the EID coefficient is reduced by a factor of 0.4 with the presence of the prepulse. A corresponding fit was also made to these data using the noninteracting model in Eqn. 2.15 in which only the dephasing time was modified by the prepulse (solid red curve in Fig. 4.9(c), with $\gamma_0 = 1/270$fs, labeled Model 2). Both models provide reasonable qualitative agreement, although the influence of the prepulse on the EID coefficient leads to a qualitative dependence on prepulse delay. In particular, the signal is constant for negative prepulse delays, but leads to an increase in the signal for positive prepulse delays. This interdependence makes it impossible to assess the relative importance of sceening and the density-dependence of the dephasing rate. Interestingly, the noninteracting model provides the best overall agreement. The deviation in the model including EID was traced back to the linear t dependence, which leads to an underestimate of the signal for small positive prepulse delays. This discrepancy may be tied to the simplicity of the EID model in Eqn. 4.1, which treats exciton-carrier scattering phenomenologically [55] and possibly the need to treat the buildup of screening dynamically [64].

In LT-GaAs, the carrier lifetime is extremely short as observed in pump probe experiments by several groups [1, 14, 65, 66, 67, 68]. This short carrier lifetime must be taken into account when considering the influence of the prepulse on the four-wave mixing response for different values of the prepulse delay. The observation of the maximum influence of the prepulse when the prepulse coincides with pulses $\vec{E}_1$ and $\vec{E}_2$ is expected because in this case all of the carriers injected by the prepulse are contributing to screening as well as to a reduction of the exciton dephasing time. However, for nonzero prepulse delay (either positive or negative) the carriers are rapidly trapped by defects, preventing these carriers from having a significant influence on the magnitude of the exciton response. This is consistent with the results in Fig. 4.10(b), which shows a reduced exciton signal only near zero prepulse delay. Rapid trapping of carriers also restricts the influence of the prepulse on the continuum response to delays in the vicinity of zero prepulse delay, consistent with the results in Fig. 4.10(d). The electron trapping time has been observed in the range of 100 - 250 fs in LT-GaAs [1, 14, 65, 66, 67, 68] and has been found to be highly sensitive to the growth conditions, as these conditions affect the density and type of trap sites [1, 14, 65, 66, 67, 68]. These four-wave mixing results, which indicate a recovery of screening in < 100 fs, suggests an even faster carrier trapping time. A useful extension to the present work would be to carry out differential transmission experiments on our LT-GaAs sample, as such experiments would provide an independent measurement of the electron trapping time. This would help to solidify the interpretation of the prepulse delay dependence of the four-wave mixing signal in LT-GaAs presented here.

Chapter 5

Conclusion

5.1 Overview

In this thesis work, the coherent dynamics of the fundamental exciton in low-temperature grown GaAs has been investigated using spectrally-resolved two-pulse four-wave mixing techniques. Four-wave mixing is a powerful experimental technique because it is sensitive to Coulomb-mediated many-body interactions that can modify the nonlinear optical response. It has been shown through a series of tailored experiments that excitation induced dephasing (EID) is the dominant contribution to the nonlinear exciton response in LT-GaAs. This conclusion was made possible through comparison to results in GaAs conducted using the same experiments and excitation conditions. The experiments in this thesis are in qualitative agreement with the two level model from Allan *et al.* [57] incorporating EID in the context of short pulse excitation above the band gap. The conclusions reached are presented in this chapter.

5.2 Summary: Conclusions of this Thesis Work

Spectrally-resolved (time-integrated) four-wave mixing has revealed that the exciton dynamics in LT-GaAs are heavily influenced by Coulomb-mediated many-body effects. In particular, the rapid decay of the SR-FWM signal versus delay on a timescale set by the width of the pulse autocorrelation is indicative of a many body effect referred to as excitation-induced dephasing, which leads to a broadband coupling between the exciton and unbound electron-hole pairs excited in the interband continuum. The resulting EID signal at the exciton, often called the *continuum contribution*, is shown to dominate the optical response at the exciton in LT-GaAs under the conditions of the experiments reported in this thesis work. (In particular in which the laser pulse is tuned above the band gap, resulting in the excitation of primarily continuum states.) For linearly co-polarized excitation, the fast decay of the exciton

FWM signal as a function of interpulse delay is a signature of such a *continuum contribution*. Contributions to the total population grating in the interband continuum stemming from a distribution of continuum transitions with different energies interfere constructively at zero interpulse delay, which leads to the observed large spectrally and temporally narrow signal at zero delay. The results presented here also permitted the extraction of the dephasing time of the exciton in LT-GaAs of $T_2 = 135$ fs from the spectral width of the exciton response. This T_2 time is shorter than the value of 250 fs in GaAs.

The identification of the exciton FWM signal as caused by EID is consistent with the experiments investigating the dependence of the signal on the polarization states of the two excitation pulses. In particular, for cross-polarized excitation, the signal at the exciton is completely suppressed in LT-GaAs. The dramatic drop in signal can be explained by the formation of a grating in the total carrier density only for linearly co-polarized pulses. In contrast, for linearly cross-polarized pulses, no such grating is formed since the grating associated with oppositely spin-polarized carriers is π out of phase, leading to no signal associated with EID. The lack of free-polarization decay in LT-GaAs that is observed in GaAs under the same conditions indicates that EID is much more influential in dictating the exciton response in LT-GaAs than in GaAs.

This thesis work was motivated by the lack of understanding of the coherent dynamics of the fundamental exciton in LT-GaAs and the recent FWM observation of a large nonlinear signal at the exciton resonance [16]. Incorporation of excess arsenic during low-temperature growth alters the electronic and optical properties of GaAs, such that linear optical techniques have been unsuccessful to resolve the spectral signature of the fundamental exciton. This has been attributed to the large presence of defects incorporated during low-temperature growth, which lead to strong defect-related contributions in the linear absorption that mask the exciton response. This thesis work establishes the importance of the exciton in understanding the nonlinear optical response of LT-GaAs. These findings will be important to the development and optimization of optoelectronic devices using LT-GaAs since such devices exploit the ultrafast nonlinear response.

A series of prepulse experiments were performed to investigate the influence of excess optically-excited carriers on the four-wave mixing response. The experimental

results have uncovered the sensitivity of the exciton FWM signal to the presence of these additional carriers through both screening and an increased dephasing rate. The strength of the TI-FWM signal is reduced by an increase in the dephasing rate as well as by screening of the exciton-carrier scattering rate. Due to these effects, the exciton FWM signal in LT-GaAs was diminished in the presence of excess carriers, being reduced to zero (within the signal to noise ratio) for a preinjected carrier density of 2.5×10^{16} cm^{-3}. This elimination of the exciton FWM signal due to the prepulse was found to persist only for a narrow range of prepulse delays around zero delay. This was explained in terms of a rapid (< 100 fs) electron trapping time in LT-GaAs, in agreement with previous studies of trapping dynamics in LT-GaAs. In contrast to the situation in GaAs, in which the density dependence of the overall reduction in the dephasing rate was found to govern the prepulse delay dependence. In LT-GaAs, the relative importance of screening and a reduction in the total dephasing rate cannot be assessed due to the short electron trapping time in this material.

5.3 Future Work

Useful extensions to this thesis work include measurements of the exciton linewidth as a function of prepulse power, and measurements of the electron trapping time in the samples studied in this work. The former measurements will permit the identification of the relative importance of exciton-carrier scattering and scattering with defects in determining the total exciton dephasing rate in LT-GaAs. The latter experiments would support the interpretation of the prepulse delay dependence at the exciton four-wave mixing response. These experiments may also be extended to other defect-laden semiconductors,including GaMnAs or other diluted magnetic semiconductors, such as LT-InP or LT-InGaAs.

Bibliography

[1] S. Gupta, M. Y. Frankel, J. A. Valdmanis, J. F. Whitaker, G. A. Mourou, F. W. Smith, and A. R. Calawa. Subpicosecond carrier lifetime in GaAs grown by molecular beam epitaxy at low temperatures. *Applied Physics Letters*, 59(25):3276–3278, 1991.

[2] H. M. van Driel, X.Q. Zhou, W. W. Rhle, J. Kuhl, and K. Ploog. Photoluminescence from hot carriers in low temperature grown gallium arsenide. *Applied Physics Letters*, 60(18), 1992.

[3] A. Orthonos S.D. Benjamin and P.W.E. Smith. Large ultrafast optical nonlinearities in as-rich gaas. *Electronic Letters*, 30:1704–1705, 1994.

[4] A. Krotkus. Semiconductors for terahertz photonics applications. *Journal of Applied Physics D: Applied Physics*, 43:273001, 2010.

[5] P. W. E Smith, S. D. Benjamin, and H. S. Loka. Tailoring of trap-related carrier dynamics in low-temperature-grown GaAs. *Applied Physics Letters*, 71(9):1156–1158, 1997.

[6] Marc Currie, Fabio Quaranta, Adriano Cola, Eric M. Gallo, and Bahram Nabet. Low-temperature grown GaAs heterojunction metal-semiconductor-metal photodetectors improve speed and efficiency. *Applied Physics Letters*, 99(20):–, 2011.

[7] F. W. Smith, H. Q. Le, V. Diadiuk, M. A. Hollis, A. R. Calawa, S. Gupta, M. Frankel, D. R. Dykaar, G. A. Mourou, and T. Y. Hsiang. Picosecond GaAs-based photoconductive optoelectronic detectors. *Applied Physics Letters*, 54(10):890–892, 1989.

[8] R. Adam, M. Mikulics, A. Förster, J. Schelten, M. Siegel, P. Kordoš, X. Zheng, S. Wu, and R. Sobolewski. Fabrication and subpicosecond optical response of low-temperature-grown GaAs freestanding photoconductive devices. *Applied Physics Letters*, 81(18):3485–3487, 2002.

[9] Sajeev John, Costas Soukoulis, Morrel H. Cohen, and E. N. Economou. Theory of electron band tails and the urbach optical-absorption edge. *Phys. Rev. Lett.*, 57:1777–1780, Oct 1986.

[10] P. Silverberg, P. Omling, and L. Samuelson. Hole photoionization cross sections of EL2 in GaAs. *Applied Physics Letters*, 52(20):1689–1691, 1988.

[11] M. O. Manasreh, D. C. Look, K. R. Evans, and C. E. Stutz. Infrared absorption of deep defects in molecular-beam-epitaxial GaAs layers grown at 200°C: Observation of an *EL*2-like defect. *Phys. Rev. B*, 41:10272–10275, May 1990.

[12] Cheng H.J. Gupta S. Whitaker J. Nichols K. Smith F.W. Liliental-Weber, Zuzanna. Structure and carrier lifetime in LT-GaAs. *Journal of Electronic Materials*, 22(12):1465–1469, 1993.

[13] N. Hozhabri, S.-H. Lee, and K. Alavi. Infrared measurements in annealed molecular beam epitaxy gaas grown at low temperature. *Applied Physics Letters*, 66(19):2546–2548, 1995.

[14] G. Segschneider, T. Dekorsy, H. Kurz, R. Hey, and K. Ploog. Energy resolved ultrafast relaxation dynamics close to the band edge of low-temperature grown gaas. *Applied Physics Letters*, 71(19):2779–2781, 1997.

[15] H. Němec, A. Pashkin, P. Kužel, M. Khazan, S. Schnüll, and I. Wilke. Carrier dynamics in low-temperature grown GaAs studied by terahertz emission spectroscopy. *Journal of Applied Physics*, 90(3):1303–1306, 2001.

[16] M. Yildirim, S. March, R. Mathew, A. Gamouras, X. Liu, M. Dobrowolska, J. K. Furdyna, and K. C. Hall. Electronic structure of $Ga_{1-x}Mn_xAs$ probed by four-wave mixing spectroscopy. *Phys. Rev. B*, 84:121202, Sep 2011.

[17] M. Yildirim, S. March, R. Mathew, A. Gamouras, X. Liu, M. Dobrowolska, J. K. Furdyna, and K. C. Hall. Interband dephasing and photon echo response in GaMnAs. *Applied Physics Letters*, 101(6):062403, 2012.

[18] L. Desplanque, J. F. Lampin, and F. Mollot. Generation and detection of terahertz pulses using post-process bonding of low-temperature-grown gaas and algaas. *Applied Physics Letters*, 84(12):2049–2051, 2004.

[19] D. Streb, M. Ruff, S. U. Dankowski, P. Kiesel, M. Kneissl, S. Malzer, U. D. Keil, and G. H. Döhler. Optical characterization of low temperature grown gaas by transmission measurements above the band gap. *The 15th North American conference on molecular beam epitaxy*, 14(3):2275–2277, 1996.

[20] John F. Whitaker. Optoelectronic applications of {LTMBE} iiiv materials. *Materials Science and Engineering: B*, 22(1):61 – 67, 1993.

[21] H. Ohno, A. Shen, F. Matsukura, A. Oiwa, A. Endo, S. Katsumoto, and Y. Iye. (ga,mn)as: A new diluted magnetic semiconductor based on gaas. *Applied Physics Letters*, 69(3), 1996.

[22] S. A. Wolf, D. D. Awschalom, R. A. Buhrman, J. M. Daughton, S. von Molnr, M. L. Roukes, A. Y. Chtchelkanova, and D. M. Treger. Spintronics: A spin-based electronics vision for the future. *Science*, 294(5546):1488–1495, 2001.

[23] R. C. Myers, B. L. Sheu, A. W. Jackson, A. C. Gossard, P. Schiffer, N. Samarth, and D. D. Awschalom. Antisite effect on hole-mediated ferromagnetism in (Ga,Mn)As. *Phys. Rev. B*, 74:155203, Oct 2006.

[24] M. Poggio, R. C. Myers, N. P. Stern, A. C. Gossard, and D. D. Awschalom. Structural, electrical, and magneto-optical characterization of paramagnetic GaMnAs quantum wells. *Phys. Rev. B*, 72:235313, Dec 2005.

[25] T. Jungwirth, P. Horodyská, N. Tesařová, P. Němec, J. Šubrt, P. Malý, P. Kužel, C. Kadlec, J. Masšek, I. Němec, M. Orlita, V. Novák, K. Olejník, Z. Šobáňň, P. Vašek, P. Svoboda, and Jairo Sinova. Systematic study of mn-doping trends in optical properties of (Ga,Mn)As. *Phys. Rev. Lett.*, 105:227201, Nov 2010.

[26] I. Kostakis and M. Missous. Optimization and temperature dependence characteristics of low temperature in0.3ga0.7as and in0.53ga0.47as-in0.52al0.48as semiconductor terahertz photoconductors. *AIP Advances*, 3(9):–, 2013.

[27] Y. Kostoulas, L. J. Waxer, I. A. Walmsley, G. W. Wicks, and P. M. Fauchet. Femtosecond carrier dynamics in lowtemperaturegrown indium phosphide. *Applied Physics Letters*, 66(14), 1995.

[28] Otfried Madelung. *Semiconductors - Basic Data*. 1996.

[29] Manuel Cardona Peter Y. Yu. *Fundamentals of Semiconductors Physics and Materials Properties*. 2005.

[30] Seldon D. Benjamin Hany S. Loka and Peter W. E. Smith. Optical characterization of low-temperature grown *gaa* for ultrafast all-optical switching devices. *IEEE Journal of Quantum Electronics*, 34(8):1426–1437, 1998.

[31] Sajeev John, Costas Soukoulis, Morrel H. Cohen, and E. N. Economou. Theory of electron band tails and the urbach optical-absorption edge. *Phys. Rev. Lett.*, 57:1777–1780, Oct 1986.

[32] Boris Petrovich Zakharchenya Felix Meier. *Optical Orientation*. Elsevier Science Ltd., November 1984.

[33] Tatsuo Yajima and Yoichi Taira. Spatial optical parametric coupling of picosecond light pulses and transverse relaxation effect in resonant media. *Journal of the Physical Society of Japan*, 47(5):1620–1626, 1979.

[34] Dai-Sik Kim, Jagdeep Shah, J. E. Cunningham, T. C. Damen, Wilfried Schäfer, Michael Hartmann, and Stefan Schmitt-Rink. Giant excitonic resonance in time-resolved four-wave mixing in quantum wells. *Phys. Rev. Lett.*, 68:1006–1009, Feb 1992.

[35] T. Rappen, U. Peter, M. Wegener, and W. Schäfer. Coherent dynamics of continuum and exciton states studied by spectrally resolved fs four-wave mixing. *Phys. Rev. B*, 48:4879–4882, Aug 1993.

[36] K. C. Hall, G. R. Allan, H. M. van Driel, T. Krivosheeva, and W. Pötz. Coherent response of spin-orbit split-off excitons in inp: Isolation of many-body effects through interference. *Phys. Rev. B*, 65:201201, Apr 2002.

[37] M. Wegener, D. S. Chemla, S. Schmitt-Rink, and W. Schäfer. Line shape of time-resolved four-wave mixing. *Phys. Rev. A*, 42:5675–5683, Nov 1990.

[38] K. Leo, M. Wegener, J. Shah, D. S. Chemla, E. O. Göbel, T. C. Damen, S. Schmitt-Rink, and W. Schäfer. Effects of coherent polarization interactions on time-resolved degenerate four-wave mixing. *Phys. Rev. Lett.*, 65:1340–1343, Sep 1990.

[39] Dai-Sik Kim, Jagdeep Shah, T. C. Damen, W. Schäfer, F. Jahnke, S. Schmitt-Rink, and K. Köhler. Unusually slow temporal evolution of femtosecond four-wave-mixing signals in intrinsic GaAs quantum wells: Direct evidence for the dominance of interaction effects. *Phys. Rev. Lett.*, 69:2725–2728, Nov 1992.

[40] Y. Z. Hu, R. Binder, S. W. Koch, S. T. Cundiff, H. Wang, and D. G. Steel. Excitation and polarization effects in semiconductor four-wave-mixing spectroscopy. *Phys. Rev. B*, 49:14382–14386, May 1994.

[41] Hailin Wang, Kyle Ferrio, Duncan G. Steel, Y. Z. Hu, R. Binder, and S. W. Koch. Transient nonlinear optical response from excitation induced dephasing in GaAs. *Phys. Rev. Lett.*, 71:1261–1264, Aug 1993.

[42] Stefan Schmitt-Rink, Dirk Bennhardt, Volker Heuckeroth, Peter Thomas, Peter Haring, Gerd Maidorn, Huib Bakker, Karl Leo, Dai-Sik Kim, Jagdeep Shah, and Klaus Köhler. Polarization dependence of heavy- and light-hole quantum beats. *Phys. Rev. B*, 46:10460–10463, Oct 1992.

[43] L. Schultheis, J. Kuhl, A. Honold, and C. W. Tu. Picosecond phase coherence and orientational relaxation of excitons in GaAs. *Phys. Rev. Lett.*, 57:1797–1800, Oct 1986.

[44] S. T. Cundiff, H. Wang, and D. G. Steel. Polarization-dependent picosecond excitonic nonlinearities and the complexities of disorder. *Phys. Rev. B*, 46:7248–7251, Sep 1992.

[45] H. Wang, K. B. Ferrio, D. G. Steel, P. R. Berman, Y. Z. Hu, R. Binder, and S. W. Koch. Transient four-wave-mixing line shapes: Effects of excitation-induced dephasing. *Phys. Rev. A*, 49:R1551–R1554, Mar 1994.

[46] L. Schultheis, J. Kuhl, A. Honold, and C. W. Tu. Ultrafast phase relaxation of excitons via exciton-exciton and exciton-electron collisions. *Phys. Rev. Lett.*, 57:1635–1638, Sep 1986.

[47] A. Honold, L. Schultheis, J. Kuhl, and C. W. Tu. Collision broadening of two-dimensional excitons in a GaAs single quantum well. *Phys. Rev. B*, 40:6442–6445, Sep 1989.

[48] D. S. Kim, J. Shah, T. C. Damen, Wilfred Schäfer, L. N. Pfeiffer, and K. Köhler. Instantaneous contribution in time-resolved four-wave mixing from GaAs quantum wells near zero time delay. *Phys. Rev. B*, 50:15086–15094, Nov 1994.

[49] L. Bányai, D. B. Tran Thoai, E. Reitsamer, H. Haug, D. Steinbach, M. U. Wehner, M. Wegener, T. Marschner, and W. Stolz. Exciton˘lo-phonon quantum kinetics: Evidence of memory effects in bulk GaAs. *Phys. Rev. Lett.*, 75:2188–2191, Sep 1995.

[50] T. Rappen, Mohs G. Schäfer W. Peter, U., and M. Wegener. Coherent dynamics of continuum and bound states in germanium. *Semicond. Sci. Technol.*, 9:422–424, May 1994.

[51] M. U. Wehner, D. Steinbach, and M. Wegener. Ultrafast coherent transients due to exciton-continuum scattering in bulk GaAs. *Phys. Rev. B*, 54:R5211–R5214, Aug 1996.

[52] S. T. Cundiff, M. Koch, W. H. Knox, J. Shah, and W. Stolz. Optical coherence in semiconductors: Strong emission mediated by nondegenerate interactions. *Phys. Rev. Lett.*, 77:1107–1110, Aug 1996.

[53] D. Birkedal, V. G. Lyssenko, J. M. Hvam, and K. El Sayed. Continuum contribution to excitonic four-wave mixing due to interaction-induced nonlinearities. *Phys. Rev. B*, 54:R14250–R14253, Nov 1996.

[54] K. El Sayed, D. Birkedal, V. G. Lyssenko, and J. M. Hvam. Continuum contribution to excitonic four-wave mixing due to interaction-induced nonlinearities: A numerical study. *Phys. Rev. B*, 55:2456–2465, Jan 1997.

[55] L. Bányai, Q. T. Vu, and H. Haug. Excitation induced dephasing in four-wave mixing and coulomb quantum kinetics. *Phys. Rev. B*, 58:R13341–R13342, Nov 1998.

[56] A. Lohner, K. Rick, P. Leisching, A. Leitenstorfer, T. Elsaesser, T. Kuhn, F. Rossi, and W. Stolz. Coherent optical polarization of bulk GaAs studied by femtosecond photon-echo spectroscopy. *Phys. Rev. Lett.*, 71:77–80, Jul 1993.

[57] G. R. Allan and H. M. van Driel. Coherence dynamics of excitons and continuum excitations in InP. *Phys. Rev. B*, 59:15740–15747, Jun 1999.

[58] Hartmut Haug and Stephan Koch. *Quantum Theory of the Optical and Electronic Properties of Semiconductors*. World Scientific Publishing Co. Pte. Ltd., 1990.

[59] R. J. Elliott. Intensity of optical absorption by excitons. *Phys. Rev.*, 108:1384–1389, Dec 1957.

[60] Jagdeep Shah. *Ultrafast Spectroscopy of Semiconductors and Semiconductor Nanostructures*. Springer, 1996.

[61] R. L. Fork, O. E. Martinez, and J. P. Gordon. Negative dispersion using pairs of prisms. *Opt. Lett.*, 9(5):150–152, May 1984.

[62] Kimberley C. Hall. *Coherent Response of Spin-Orbit Split-Off Excitons in InP*. PhD thesis, University of Toronto, 2002.

[63] Anthony E. Siegman. *Lasers*. University Science Books, 1986.

[64] L. Bányai, Q. T. Vu, B. Mieck, and H. Haug. Ultrafast quantum kinetics of time-dependent rpa-screened coulomb scattering. *Phys. Rev. Lett.*, 81:882–885, Jul 1998.

[65] M. Haiml, U. Siegner, F. Morier-Genoud, U. Keller, M. Luysberg, R. C. Lutz, P. Specht, and E. R. Weber. Optical nonlinearity in low-temperature-grown GaAs: Microscopic limitations and optimization strategies. *Applied Physics Letters*, 74(21), 1999.

[66] M. Haiml, U. Siegner, F. Morier-Genoud, U. Keller, M. Luysberg, P. Specht, and E. R. Weber. Femtosecond response times and high optical nonlinearity in beryllium-doped low-temperature grown GaAs. *Applied Physics Letters*, 74(9), 1999.

[67] S. D. Benjamin, H. S. Loka, A. Othonos, and P. W. E. Smith. Ultrafast dynamics of nonlinear absorption in low temperature grown GaAs. *Applied Physics Letters*, 68(18), 1996.

[68] M. Stellmacher, J. Nagle, J. F. Lampin, P. Santoro, J. Vaneecloo, and A. Alexandrou. Dependence of the carrier lifetime on acceptor concentration in GaAs grown at low-temperature under different growth and annealing conditions. *Journal of Applied Physics*, 88(10), 2000.

Appendix A

Copyright Permissions

Figure 1.5 (c),(d)

Daniel Webber

From:	Sarah Ryder [Sarah.Ryder@iop.org] on behalf of Permissions [permissions@iop.org]
Sent:	November 26, 2013 4:38 AM
To:	Daniel Webber
Subject:	Re: Permission Request - Daniel Webber
Attachments:	Permission Request - Daniel Webber.docx

Dear Daniel Webber,

Thank you for your request to reproduce IOP Publishing material.

We are happy to grant permission for the use you request on the terms set out below.

If you have any questions, please feel free to contact our Permissions team at permissions@iop.org.

I should be grateful if you would acknowledge receipt of this email.

Kind regards,

Sarah Ryder

Publishing Administrator
Email: permissions@iop.org

Conditions

Non-exclusive, non-transferrable, revocable, worldwide, permission to use the material in print and electronic form will be granted **subject to the following conditions:**

- Permission will be cancelled without notice if you fail to fulfil any of the conditions of this letter.

- You will make reasonable efforts to contact the author(s) to seek consent for your intended use. Contacting one author acting expressly as authorised agent for their co-authors is acceptable.

- You will reproduce the following prominently alongside the material:

o the source of the material, including author, article title, title of journal, volume number, issue number (if relevant), page range (or first page if this is the only information available) and date of first publication. This information can be contained in a footnote or reference note; or

o a link back to the article (via DOI); and

o if practical and IN ALL CASES for works published under any of the Creative Commons licences the words "© IOP Publishing. Reproduced by permission of IOP Publishing. All rights reserved"

- The material will not, without the express permission of the author(s), be used in any way which, in the opinion of IOP Publishing, could distort or alter the author(s)' original intention(s) and meaning, be prejudicial to the honour or reputation of the author(s) and/or imply endorsement by the author(s) and/or IOP Publishing.

- Payment of £0 is received in full by IOP Publishing prior to use.

Please note: IOP does not usually provide signed permission forms as a separate attachment. Please print this email and provide it to your publisher as proof of permission.

1

November 25, 2013

To whom it may concern

I am preparing a dissertation entitled

"OBSERVATION OF THE FUNDAMENTAL EXCITON IN

LOW-TEMPERATURE GROWN GaAs USING FOUR-WAVE MIXING SPECTROSCOPY"

as part of my Master's program, which shall be published in: Dalhousie University Thesis Collection

I would appreciate permission to reproduce the following item(s) in both print and electronic editions of the Journal and in all subsequent future editions of the Journal, any derivative products and in publisher authorized distribution by third party distributors, aggregators and other licensees such as abstracting and indexing services. I should be grateful for nonexclusive perpetual world rights in all languages and media. Unless you indicate otherwise, I will use the complete reference given below as the credit line.

In case you do not control these rights, I would appreciate it if you could let me know to whom I should apply for permissions.

1. Figure 1, "Coherent dynamics of continuum and bound states in germanium", T Rappen, U Peter, G Mohs, W Schafer, M Wegener, Semicond. Sci. Technol., 9, 422-424, 1994, IOP Publishing Ltd.

For material being published electronically a link to the version of record will be provided back to the original article via DOI.

For your information, Institute of Physics Publishing is a not-for-profit subsidiary of the UK Institute of Physics and is a signatory to the STM guidelines on use and republication of figures/tables in science publishing.

For your convenience a copy of this letter may serve as a release form: the duplicate copy may be retained for your files.

Thank you for your prompt attention to this request. Permission is being requested of the authors and the publisher separately.

Yours sincerely

Daniel Webber

M.Sc. Candidate
Department of Physics and Atmospheric Science
Dalhousie University
Halifax, Nova Scotia, Canada
B3H 4R2

Figure 2.3 (a)

**AIP PUBLISHING LLC LICENSE
TERMS AND CONDITIONS**

Nov 24, 2013

All payments must be made in full to CCC. For payment instructions, please see information listed at the bottom of this form.

License Number	3275501196383
Order Date	Nov 24, 2013
Publisher	AIP Publishing LLC
Publication	Journal of Vacuum Science & Technology B
Article Title	Optical characterization of low temperature grown GaAs by transmission measurements above the band gap
Author	D. Streb,M. Ruff,S. U. Dankowski, et al.
Online Publication Date	May 1, 1996
Volume number	14
Issue number	3
Type of Use	Thesis/Dissertation
Requestor type	Student
Format	Print and electronic
Portion	Figure/Table
Number of figures/tables	1
Title of your thesis / dissertation	OBSERVATION OF THE FUNDAMENTAL EXCITON IN LOW-TEMPERATURE GROWN GaAs USING FOUR-WAVE MIXING SPECTROSCOPY
Expected completion date	Dec 2013
Estimated size (number of pages)	110
Total	0.00 USD
Terms and Conditions	

American Vacuum Society -- Terms and Conditions: Permissions Uses

American Vacuum Society ("AVS") hereby grants to you the non-exclusive right and license to use and/or distribute the Material according to the use specified in your order, on a one-time basis, for the specified term, with a maximum distribution equal to the number that you have ordered. Any links or other content accompanying the Material are not the subject of this license.

1. You agree to include the following copyright and permission notice with the reproduction of the Material:"Reprinted with permission from [FULL CITATION]. Copyright [PUBLICATION YEAR], American Vacuum Society." For an article, the copyright and permission notice must be printed on the first page of the article or book chapter. For photographs, covers, or tables, the copyright and permission notice may appear with the Material, in a footnote, or in the reference list.
2. If you have licensed reuse of a figure, photograph, cover, or table, it is your responsibility to ensure that the material is original to AVS and does not contain the copyright of another entity, and that the copyright notice of the figure, photograph, cover, or table does not indicate that it was reprinted by AVS, with permission, from another source. Under no circumstances does AVS, purport or intend to grant permission to reuse material to which it does not hold copyright.
3. You may not alter or modify the Material in any manner. You may translate the Material into another language only if you have licensed translation rights. You may not use the Material for promotional purposes. AVS reserves all rights not specifically granted

herein.

4. The foregoing license shall not take effect unless and until AVS or its agent, Copyright Clearance Center, receives the Payment in accordance with Copyright Clearance Center Billing and Payment Terms and Conditions, which are incorporated herein by reference.
5. AVS or the Copyright Clearance Center may, within two business days of granting this license, revoke the license for any reason whatsoever, with a full refund payable to you. Should you violate the terms of this license at any time, AVS, American Vacuum Society, or Copyright Clearance Center may revoke the license with no refund to you. Notice of such revocation will be made using the contact information provided by you. Failure to receive such notice will not nullify the revocation.
6. AVS makes no representations or warranties with respect to the Material. You agree to indemnify and hold harmless AVS, American Vacuum Society, and their officers, directors, employees or agents from and against any and all claims arising out of your use of the Material other than as specifically authorized herein.
7. The permission granted herein is personal to you and is not transferable or assignable without the prior written permission of AVS. This license may not be amended except in a writing signed by the party to be charged.
8. If purchase orders, acknowledgments or check endorsements are issued on any forms containing terms and conditions which are inconsistent with these provisions, such inconsistent terms and conditions shall be of no force and effect. This document, including the CCC Billing and Payment Terms and Conditions, shall be the entire agreement between the parties relating to the subject matter hereof.

This Agreement shall be governed by and construed in accordance with the laws of the State of New York. Both parties hereby submit to the jurisdiction of the courts of New York County for purposes of resolving any disputes that may arise hereunder.

If you would like to pay for this license now, please remit this license along with your payment made payable to "COPYRIGHT CLEARANCE CENTER" otherwise you will be invoiced within 48 hours of the license date. Payment should be in the form of a check or money order referencing your account number and this invoice number RLNK501166601. Once you receive your invoice for this order, you may pay your invoice by credit card. Please follow instructions provided at that time.

Make Payment To:
Copyright Clearance Center
Dept 001
P.O. Box 843006
Boston, MA 02284-3006

For suggestions or comments regarding this order, contact RightsLink Customer Support: customercare@copyright.com or +1-877-622-5543 (toll free in the US) or +1-978-646-2777.

Gratis licenses (referencing $0 in the Total field) are free. Please retain this printable license for your reference. No payment is required.

Figure 1.1 (a),(b)

Daniel Webber

From: Essenpreis, Alice, Springer DE [Alice.Essenpreis@springer.com]
Sent: December 6, 2013 9:34 AM
To: Daniel Webber
Subject: WG: Permission to Reproduce

DATE: December 6, 2013

SPRINGER REFERENCE
Semiconductors — Basic Data. 1996
Editors: Prof. Dr. Otfried Madelung
ISBN: 978-3-642-97677-3
To be reused: Fig. 1 on page 102
Fig. 36 on page 256

YOUR PROJECT
Title: Observation of the fundamental exciton low-temperature grown GaAs using four-wave mixing spectroscopy"Dissertation/Thesis
University: Dalhousie University

Dear Mr. Webber,

Thank you for your e-mail.

With reference to your request to reuse material in which Springer Science+Business Media controls the copyright, our permission is granted free of charge under the following conditions:

Springer material
• represents original material which does not carry references to other sources (if material in question refers with a credit to another source, authorization from that source is required as well); • requires full credit (book title, year of publication, page, chapter title, name(s) of author(s), original copyright notice) is given to the publication in which the material was originally published by adding: "With kind permission of Springer Science+Business Media"; • may not be altered in any manner. Any other abbreviations, additions, deletions and/or any other alterations shall be made only with prior written authorization of the author and/or Springer Science+Business Media.

This permission
• is non-exclusive;
• is valid for one-time use only for the purpose of defending your thesis and with a maximum of 100 extra copies in paper.
• includes use in an electronic form, provided it is an author-created version of the thesis on his/her own website and his/her university's repository, including UMI (according to the definition on the Sherpa website: http://www.sherpa.ac.uk/romeo/);
• is subject to courtesy information to the corresponding author; • is personal to you and may not be sublicensed, assigned, or transferred by you to any other person without Springer's written permission; • is valid only when the conditions noted above are met.

Permission free of charge does not prejudice any rights we might have to charge for reproduction of our copyrighted material in the future.

Best regards,

Rights and Permissions
Springer-Verlag GmbH
Tiergartenstr. 17
69121 Heidelberg
Germany
E-mail: permissions.heidelberg@springer.com

-----Ursprüngliche Nachricht-----
Von: SpringerAlerts@springeronline.com [mailto:SpringerAlerts@springeronline.com]
Gesendet: Dienstag, 26. November 2013 22:34
An: Permissions Heidelberg, Springer DE
Betreff: Permission to Reproduce

Hello,

I am seeking permission to reproduce two figures from the book "Semiconductors - Basic Data". The relevant information pertaining to the two figures, as well as how they will be reproduced, are given below.

ISBN - 3-540-60883-4
Book Title - Semiconductors - Basic Data, 2nd Revised Edition Editor - Otfried Madelung Year of Book - 1996

I would like to reproduce two (2) figures:

1. Page 102, Figure 1. "GaAs. Band structure obtained by a non-local pseudopotential calculation."

2. Page 256, Figure 36. "Brillouin zone of the zincblende and NaCl lattices."

I wish to reproduce these two figures in my Master's thesis. The pertinent information is as follows:

Title - "Observation of the fundamental exciton low-temperature grown GaAs using four-wave mixing spectroscopy"
Author - Daniel Webber (Myself)
Department - Physics and Atmospheric Science Institution - Dalhousie University. Halifax, Nova Scotia, Canada. B3H 4R2
Number of copies - Depends. Theses are available to the public through the Dalhousie Thesis Collection Library both in print and electronically.
Fee - Printed copies of the thesis are available for a fee from the Dalhousie University Thesis Collection.

Thank you. I look forward to your response.

Daniel Webber

MSc. Candidate
Department of Physics and Atmospheric Science Dalhousie University Halifax, Nova Scotia, Canada B3H 4R2

[
Subject: Permission to Reproduce
Sender name: Daniel Webber
Sender email: daniel.webber@dal.ca
Page name: Rights and Permissions Department - Springer Verlag Heidelberg Page url:
http://www.springer.com/rights?SGWID=0-122-19-161426-0
]